IMAGING SUBSURFACE FRACTURE CHARACTERISTICS USING ELECTRICAL

RESISTIVITY TOMOGRAPHY: A CASE STUDY IN DOUGHERTY COUNTY,

SOUTHWEST GEORGIA

by

KWAKU ASIEDU

(Under the Direction of Charlotte Garing)

ABSTRACT

This study employed Electrical Resistivity Tomography (ERT) to investigate the

correlation between lineaments and subsurface bedrock fractures within the Ocala Limestone in

Dougherty County, southwest Georgia. Borehole geophysical logs were analyzed to guide survey

site selection and served as reference data for simulating ERT field responses. Synthetic data

generated from these forward models helped determine the dipole-dipole as the suitable array for

the ERT survey. Seven surveys were carried out using this array, of which six were across mapped

lineaments. Of these six surveys, only one showed evidence of a potential fracture within the Ocala

limestone. While remote sensing techniques such as aerial photographs are useful for identifying

potential fractures through lineament mapping, they provide limited field evidence regarding the

precise location of these fractures. Interpretations from the inverted sections also revealed

lentiform features within the upper unit of the Ocala limestone, suggesting the presence of water-

filled or clay-filled cavities.

INDEX WORDS:

Lineament, Fracture, Electrical Resistivity Tomography, Ocala Limestone

IMAGING SUBSURFACE FRACTURE CHARACTERISTICS USING ELECTRICAL RESISTIVITY TOMOGRAPHY: A CASE STUDY IN DOUGHERTY COUNTY, SOUTHWEST GEORGIA

by

KWAKU ASIEDU

BS, Kwame Nkrumah University of Science and Technology University, 2021

A Thesis Submitted to the Graduate Faculty of The University of Georgia in Partial Fulfillment of the Requirements for the Degree

MASTER OF SCIENCE

ATHENS, GEORGIA

2025

© 2025

Kwaku Asiedu

All Rights Reserved

IMAGING SUBSURFACE FRACTURE CHARACTERISTICS USING ELECTRICAL RESISTIVITY TOMOGRAPHY: A CASE STUDY IN DOUGHERTY COUNTY, SOUTHWEST GEORGIA

by

KWAKU ASIEDU

Major Professor: Charlotte Garing
Committee: Adam M. Milewski

Robert Hawman

Electronic Version Approved:

Ron Walcott Vice Provost for Graduate Education and Dean of the Graduate School The University of Georgia May 2025

DEDICATION

I dedicate this work to my family, whose encouragement, immense support, and prayers have been my greatest source of strength and inspiration. To my parents, Kwaku Sarpong and Adwoa Pomaa, for instilling in me the values of perseverance and for always believing in my dreams. They are my biggest motivation to succeed.

To all those who strive to make a difference in geoscience, may this work contribute to advancing our collective knowledge of the Earth's subsurface characteristics.

ACKNOWLEDGEMENTS

First, I would like to express my sincere appreciation to my advisor, Dr. Charlotte Garing, for her guidance and support throughout this journey. You are truly a great advisor, mentor, and friend. I also wish to thank my advisory committee, Dr. Milewski and Dr. Hawman, for their assistance, encouragement, guidance, and invaluable suggestions. Your expertise and support have greatly contributed to the success of this work.

I am also grateful to the porous media flow, and the water resources and remote sensing (WRRS) lab groups for the memories and collaborations. Special thanks go to the organization and funding bodies that supported this research: the Watts Wheeler Research Grant, the John Spencer Grant, the Geological Society of America Research Grant, and the Georgia Flow Incentive Trust Fund. To my dedicated field assistants, Michael Stefanou, Luqman Olawale, Fabian Zowam, Taran Bradley, and Yaw Barima Buabeng, I cannot thank you enough for your hard work and commitment. I also want to thank Ms. Wynn Page of Angus Graham Farm and Brent Howze of Albany Nursery Wildlife Management Area for granting me access to their sites for my fieldwork. Special thanks to Dr. Daniel Markewitz for providing the Supersting R8 resistivity meter and its accessories. This equipment was indispensable to the success of this work.

Most importantly, I want to thank God for His grace and blessings in making this dream a reality.

TABLE OF CONTENTS

ACKNOWLEDGEMENTS	v
LIST OF TABLES	ix
LIST OF FIGURES	X
CHAPTER 1	1
INTRODUCTION	1
1.1 Background and Significance	1
1.2 Objectives of the Study	4
1.3 Study Area	5
CHAPTER 2	12
LITERATURE REVIEW	12
2.1. Background on Lineaments	12
2.1.1. Formation of Lineaments	13
2.1.2. Early Studies on Lineaments	14
2.1.3. Importance of Fracture–Correlated Lineaments	16
2.1.4. Methods of Lineament Detection and Analysis	17
2.1.5. Challenges and Limitations of Lineament Detection and Analysis	19
2.1.6. Geophysical Surveys as A Tool to Validate Lineaments	19

2.2. Background on Geophysical Methods	20
2.2.1. Categories of Geophysical Methods	21
2.2.2. Electrical Resistivity Method	22
2.2.2.1. Basic Concepts About Resistivity	24
2.2.2.2. Theoretical Determination of Apparent Resistivity	27
2.2.2.3. Electrical Resistivity with Its Structural and Lithological Relationships	32
2.2.2.4. Electrical Resistivity Survey Methods	34
2.2.2.5. Electrical Resistivity Tomography in Karst Environments	35
2.2.2.6. Electrode Arrays Used in ERT Surveys	37
2.2.2.7. Electrical Resistivity Tomography Studies for Investigating Lineaments	44
2.2.2.8. Resolution Limitations of Electrical Resistivity Tomography Method	45
CHAPTER 3	47
METHODOLOGY	47
3.1. Borehole Geophysical Logging	47
3.2. Forward Modeling	49
3.3. Electrical Resistivity Tomography Survey	53
3.4.1. Survey Design	53
3.4.2. Data Acquisition	54
3.4.3. Inverse Modeling	56

CHAPTER 465
RESULTS AND DISCUSSION65
4.1. Well Logs Interpretation
4.2. Simulating Subsurface Responses from Forward Modeling
4.3. Resistivity Profiles and Subsurface Characterization
4.3.1. General Comments About the Model Sections
4.3.2 Interpretations of Model Sections
4.3.3. ERT Field Results
4.4. Discussion of Results
CHAPTER 5
CONCLUSIONS
5.1. Conclusions
5.2. Future Works
REFERENCES

LIST OF TABLES

Table 2.1: Geophysical methods and the characteristic physical properties they measure.20
Table 2.2: Mean depth of investigation (ze) for the different arrays used in electrical resistivity
surveys. L is the total length of the survey (Edwards, 1997)
Table 2.3: Various electrode arrays, their advantages, limitations, and suitable applications. W-S
is the Wenner-Schlumberger array (modified from (Bernard et al., 2006)) 44
Table 3.1: List of wells, GPS coordinates, total depths logged, and overburden thickness.47
Table 3.2: Parameters used in creating the various synthetic models
Table 3.3: Parameters used in creating AGI command file
Table 3.4: Parameters for ERT inversion process
Table 4.1: Anomaly effect calculations used in selecting the most suitable electrode array.68
Table 4.2: Bedrock depths and associated resistivity ranges interpreted from the seven model
sections

LIST OF FIGURES

Figure 1.1: Distribution of karst terrains in the United States (modified from Polk et al., 2007).
8
Figure 1.2: Possible fractures in the Ocala limestone mapped for sinkhole data, Dougherty
County, Georgia (modified from Brook & Allison, 1983)
Figure 1.3: Map of Dougherty County, southwest Georgia
Figure 1.4: Generalized lithostratigraphic and hydrostratigraphic units underlying Albany and
surrounding areas, southwestern Georgia. Middle Eocene and younger modified from
(Hicks et al., 1987), lower Eocene and older modified from (Clarke et al., 1984) 11
Figure 2.1: The flow of current from a point source and the resulting equipotential surfaces in a
level field with homogeneous subsurface structure (modified from Loke, 2001) 26
Figure 2.2: A schematic representation of Ohm's Law showing an electric circuit consisting of a
resistor and a battery with current flowing through a cylindrical material (modified from
Nadia, 2012)
Figure 2.3: Current lines radiating from the source electrode and converging on the sink
(modified after E. S. Robinson, 1988)
Figure 2.4: Generalized form of electrode configuration in resistivity survey used in generating
the apparent resistivity in equation 11, $C_1P_1=r_1$, $C_1P_2=r_2$, $C_2P_1=r_3$, $C_2P_2=r_4$. (modified
from Soge et al., 2019)
Figure 2.5: Resistivity of common rocks, soil materials, and chemicals (modified from Loke,
2011)

Figure 2.6: 2-D sensitivity section for different electrode arrays (modified after Loke, 2011).	
39	
Figure 2.7: Arrangement of electrodes in the a) Wenner electrode array, b) symmetrical	
Schlumberger electrode array and c) Dipole-Dipole electrode array (modified after Loke,	
2011)	
Figure 3.1: Composite log response from one of the USGS well logs (11L116). Deflections to	
the left on the gamma ray log in green show low readings, and to the right show high	
readings. Limestones show lower readings than sands because of the lower amount of	
radioactive elements	
Figure 3.2: Map showing the midpoints of the ERT survey lines	
Figure 3.3: AGI Supersting R8 resistivity meter deployed in the field	
Figure 3.4: Geometry of the dipole-dipole field measurement (modified from Wylie et al., 2014	.).
P1 and P2 are the potential electrodes, C1 and C2 are the current electrodes, and 'a' is the	
spacing between the electrode pairs	
Figure 4.1: Map showing the location of the twenty-nine wells used in refining the general	
knowledge of the study area (All but well CA11 are USGS wells)69	
Figure 4.2: Well-to-well correlation panel of the hydrostratigraphic units across the study area	
from SW to NE	
Figure 4.3a: Synthetic (top) and inverted (middle and bottom) sections of a three-layered	
subsurface model with a 4 m fracture located at the center of the survey line, extending	
vertically through the overburden and into the Ocala limestone. The middle-inverted section	or

represents resistivity distributions using the Wenner array while the bottom section
represents resistivity distributions using the Dipole-Dipole array71
Figure 4.3b: Synthetic (top) and inverted sections (middle and bottom) of a three-layered
subsurface model with a 4 m fracture located at the center of the survey line, confined
entirely within the Ocala limestone. The middle-inverted section represents resistivity
distributions using the Wenner array while the bottom section represents resistivity
distributions using the Dipole-Dipole array
Figure 4.4: Synthetic (left) and inverted ERT sections (right) illustrating fractures of varying
widths within the Ocala limestone using the dipole-dipole array: (a) 1m fracture, (b) 2m
fracture, (c) 3m fracture, and (d) 4m fracture73
Figure 4.7: Orientation of ERT survey lines at the Angus Graham Farm site
Figure 4.12: Orientation of ERT survey lines at the Wildlife Management Areas 84
Figure 4.5: Uninterpreted (top) and interpreted (bottom) resistivity model sections of the survey
conducted at Whitehall, University of Georgia, Athens campus. The black curvy dashed
lines indicate the inferred soil-bedrock contact and the blue solid line indicates a potential
fault90
Figure 4.6: Uninterpreted (top) and interpreted (bottom) resistivity model sections of profile line
E. The black curvy dashed lines indicate the inferred soil-bedrock contact and the black
solid line indicates a potential fracture. The black triangle indicates the location of a well.
91

Figure 4.8: Uninterpreted (top) and interpreted (bottom) resistivity model sections of profile line
A. The black horizontal dashed lines indicate the inferred soil-bedrock contact and the blue
sub-vertical line indicate a potential fault
Figure 4.9: Uninterpreted (top) and interpreted (bottom) resistivity model sections of profile line
B. The black horizontal dashed lines indicate the inferred soil-bedrock
Figure 4.10: Uninterpreted (top) and interpreted (bottom) resistivity model sections of profile
line F. The black curvy dashed lines indicate the inferred soil-bedrock contact and the black
full line indicates a potential fracture zone
Figure 4.11: Uninterpreted (top) and interpreted (bottom) resistivity model sections of profile
line G. The black horizontal dashed lines indicate the inferred soil-bedrock contact.95
Figure 4.13: Uninterpreted (top) and interpreted (bottom) resistivity model sections of profile
line C. The black horizontal dashed lines indicate the inferred soil-bedrock contact.96
Figure 4.14: Uninterpreted (top) and interpreted (bottom) resistivity model sections of profile
line D. The black horizontal dashed lines indicate the inferred soil-bedrock contact.97

CHAPTER 1

INTRODUCTION

1.1 Background and Significance

Water resource management plays an important role in ensuring the sustainable use and protection of one of the earth's most vital natural resources (Gleick, 1998). With increasing global population and climate change impacts, the effective management and development of water resources has become increasingly important, as there is the need to safeguard these resources for future generations (Cosgrove & Loucks, 2015). To do this, there is the need for an improved knowledge and understanding of groundwater systems, as they serve as significant sources of freshwater for industrial, domestic, and agricultural use (Foster et al., 2013). While groundwater is considered renewable, its availability remains finite. Therefore, locating, developing, and sustainably managing these resources is essential for meeting current and future demands while mitigating the risks associated with the poor siting of boreholes, over-extraction, and contamination (Mleta, 2010).

Southwest Georgia provides a compelling case study for developing strategies related to groundwater resource management due to its unique geological and agricultural setting. The region lies within a karst terrain dominated by the Ocala limestone formation (Hicks et al., 1981). Karst landscapes in green as shown in Figure 1.1, are commonly characterized by soluble bedrocks such as limestones and dolomites, and covers significant areas of the United States. These rocks are susceptible to dissolution and the formation of unique landscape features such as sinkholes, caves, and underground drainage systems and subsurface features such as solution-widened fractures

(White, 1990). These features, especially fractures, contribute significantly control the development, movement, and storage of groundwater (Cook, 2003).

As the agricultural industry in southwest Georgia continues to grow, increased water withdrawals from the Apalachicola, Chattahoochee, and Flint (ACF) River basins, as well as from the Upper Floridan aquifer, have become a pressing challenge (Karki et al., 2021; Rugel, 2020). There have been concerns regarding the sustainability of these water resources during periods of drought and the adverse effects it would have on the aquatic ecosystem. This, therefore calls for improved surface and groundwater management, making it crucial to understand the distribution and characteristics of features such as fractures for the effective management and development of groundwater resources in the region (Šumanovac & Weisser, 2001; White, 1988).

Previous work by Brook and Allison (1983) identified 1,298 possible fractures in Dougherty County, southwest Georgia, based on the linear alignment of geomorphological features such as topographic features, drainage patterns, and soil tonal changes (Figure 1.2). These linear features, commonly termed lineaments, were helpful in describing the regional patterns of sinkhole formation. The study showed that the mapped fractures with orientations of 325°, 5°, and 40° aligned with observed sinkhole development in the area and that they extended greater than 50 m within the subsurface, highlighting the importance of these linear features in karst terrains. To sustainably explore and exploit groundwater resources, lineament investigations are therefore required for the proper siting of boreholes (Maina & Tudunwada, 2017), as these features often reflect underlying structural discontinuities, including fractures. Lineaments can be defined as linear or curvilinear features observed on the Earth's surface that manifest as alignments of topographic features, changes in vegetation patterns, or subtle variations in landscape morphology (Lattman, 1958; O'Leary et al., 1976). Over the past decades, lineament mapping has been used

for water resource investigations, as they are believed to be surface expressions of joints, fractures, and zones of joint contributions within the subsurface (Boyer & McQueen, 1964; Brown, 1994; Dhakate et al., 2008; Lattman & Parizek, 1964). By studying the distribution and characteristics of lineaments, geologists and hydrogeologists can infer the existence and extent of fractures within the subsurface (Caran, 1982). However, several studies have also shown a notable divergence of lineaments from dominant joints and fractures (Acharya et al., 2012; Lattman & Matzke, 1961), demanding more investigations of surface-mapped lineaments. This research aimed to demonstrate the spatial correlation between the geomorphological features identified as fractures and subsurface fractures located in Dougherty County (Figure 1.3). For this research, the term fracture will refer to cracks in bedrock observed or measured in the field.

Conventional methods using spatial data have provided valuable insights into mapping lineaments, but they are often limited in their ability to delineate subsurface features accurately. It is sometimes difficult to insinuate whether the lineaments are surface manifestations of underground fractures or just linear features on the surface with no structural significance (G. K. Moore & Waltz, 1983; Sander, 2007). To address this limitation, geophysical prospecting can be used to augment these photogeological studies to validate the geomorphic features identified from the remote sensing techniques. These geophysical surveys can delineate subsurface features using techniques such as seismic refraction and refraction, ground penetrating radar, gravity, and electrical resistivity (Hagrey, 2012; Milsom & Eriksen, 2013). The electrical resistivity method was employed in this research as it is sensitive to variations in electrical conductivity within the subsurface due to the contrast between subsurface materials. This makes the electrical resistivity method effective for delineating near-surface geological features such as faults and fractures, which often exhibit resistivity anomalies compared to surrounding rock formations due to the

presence of fluids or mineralization (Gelis et al., 2016; Obiadi et al., 2012; Szalai et al., 2018). Electrical resistivity surveys are therefore valuable adjuncts to the remote sensing studies to verify the connection between mapped lineaments or fracture traces and underlying vertical bedrock fractures (Setzer, 1966).

This work is inscribed within a larger effort by the Georgia Flow Incentive Trust (GA-FIT), supported by the American Rescue Plan Act, aimed at improving water supply security in southwest Georgia by providing farmers with the necessary tools to satisfy agricultural needs regarding water use. The outcome of this research will be a valuable reference for future groundwater exploration and management efforts in selecting well sites for developing new groundwater supplies in similar hydrogeologic settings. By demonstrating the importance of thorough field analysis before drilling operations and integrating existing spatial data with geophysical site surveys, this study will form the foundation of a new exploration strategy to improve borehole success rates in similar geological settings. Results from this study will also help in selecting potential sites for sewage disposal in Dougherty County and validate the use of the Claiborne aquifer as an alternate source of water for the farmers in southwest Georgia.

1.2 Objectives of the Study

This present work outlines the use of the Electrical Resistivity Tomography (ERT) technique to investigate the relationship between lineaments and subsurface fractures and their potential influence on groundwater movement and hydraulic connectivity in the karst environment of Dougherty County, southwest Georgia. Data from individual boreholes may not be enough for a comprehensive site assessment due to the spatial heterogeneity of karst features. ERT was used to attempt to confirm the presence and extent of the mapped fractures within the subsurface. The objectives of this research were to:

- 1. Integrate well logs and drill cuttings data to improve the general geology of the subsurface in the study area.
- 2. Identify and characterize the spatial heterogeneity of the Ocala limestone.
- 3. Assess the effectiveness and limitations of the ERT as a tool for identifying fractures within the subsurface.
- 4. Validate whether lineaments are surface manifestations of underground geological features such as fractures and or joints.

1.3 Study Area

Dougherty County, located in southwestern Georgia spans between longitude 84°00' and 83°30' W and latitude 31°25' and 31°40' N. It is bordered by Worth County to the east, Lee and Terrell Counties to the north, Calhoun County to the west, and to the south by Baker and Mitchell Counties (Wait, 1963). It is a karstic physiographic district dominated by sinkholes and uvalas and covers about 852 km² of land. Albany, the county seat and largest city in southwest Georgia, serves as the regional trade hub. The land cover primarily consists of row-crop agriculture, natural and planted pine forests, with widespread center-pivot agricultural irrigation (Martin, 2010). Land use in the study area is dominated by residential and agricultural activities, supplemented by light to heavy industries generally near the Albany city limit (Stewart et al., 1999).

The agriculture economy of Georgia, valued at over \$12.2 billion, relies heavily on southwest Georgia, where cotton, peanuts, and lumber, three of the state's top commodities are produced. These industries are major consumers of water from the Flint River Basin, with irrigation expanding significantly since the 1950s to sustain crops during droughts (Jennifer Hafer, 2022). Groundwater therefore is a vital resource in the Coastal Plain of Georgia, and essential for

public and domestic water supplies in Dougherty County. The aquifer system and surface water sources in the county support residential, agricultural, and industrial needs (Stewart et al., 1999). As Dougherty County continues to grow, water demand is projected to rise, necessitating the drilling of new wells to meet increased groundwater needs, particularly for agricultural irrigation (Gordon, 2020).

1.3.1 Lithostratigraphic and Hydrostratigraphic Descriptions

Dougherty County is underlain by rocks ranging in age from Paleozoic to recent, made up of sand, clay, and limestone (Figure 1.4). These formations have significant groundwater resources within limestone and sand beds, ranging in age from late Cretaceous to late Eocene (Wait, 1963). The sediments and sedimentary rocks within the study area dip gently to the southeast and generally thicken in that direction. This study focuses on geologic units bounding the Ocala limestone, including in stratigraphic order, the middle Eocene Lisbon Formation, upper Eocene Ocala Limestone, and undifferentiated overburden of Quaternary age (Hicks et al., 1981).

The undifferentiated overburden (surface residuum) is predominantly red to reddish brown in color and is made up of sand, clay, and boulders, some of which are several meters in diameter (Hayes et al., 1983; Wait, 1963). Its thickness averages approximately 13 m in the northwest and increases to about 19 m in the southeast, overlying the Ocala limestone almost everywhere. The overburden consisting mainly of sand is probably alluvium deposited by local streams whereas the overburden consisting of mainly clay is considered residuum from the weathering of the Ocala Limestone. Generally, the thickness of the overburden highly varies and may increase by more than 30 m over a 3 km distance (Brook & Allison, 1983).

The Ocala limestone is a highly pure limestone formation, composed of up to 98% calcium carbonate. The upper surface of the Ocala limestone in the area has a highly irregular topography

because of differential weathering. In the west, where it infrequently outcrops, the limestone may be as thin as 15 m, whereas in the east, it is more than 75 m thick (Hicks et al., 1981). The region has a minimal relief, gentle formation dip, and a generally thick residual material overlying the Ocala limestone resulting in fewer outcrops within the county. However, the Ocala limestone extensively outcrops in a wide area in western Georgia, including most of the Dougherty Plain and its outcrop zone extends eastward to the Okmulgee River. It is present in southern and southeastern Georgia in the subsurface with the best exposures along the Flint River where channels as deep as 18 m have been eroded (Brantly, 1916). In the study area, the Ocala Limestone is divided into upper and lower units, with thicknesses reaching approximately 82 meters. The lower unit consists of interbedded glauconitic and dolomitic limestone, while the upper unit is composed of fossiliferous, very fine-grained, chalky limestone interbedded with thin layers of calcareous sand (Hicks et al., 1987).

Beneath the Ocala Limestone lies the Lisbon Formation, a dense, brownish-gray, clayey, glauconitic limestone. The thickness of the Lisbon Formation ranges from 0.3 m in central Lee County to 30 m at Albany (Hicks et al., 1981). Due to its significantly lower water-yielding capacity compared to the Ocala limestone, the Lisbon Formation forms the lower confining unit of the Upper Floridan Aquifer in Dougherty County (Hayes et al., 1983).

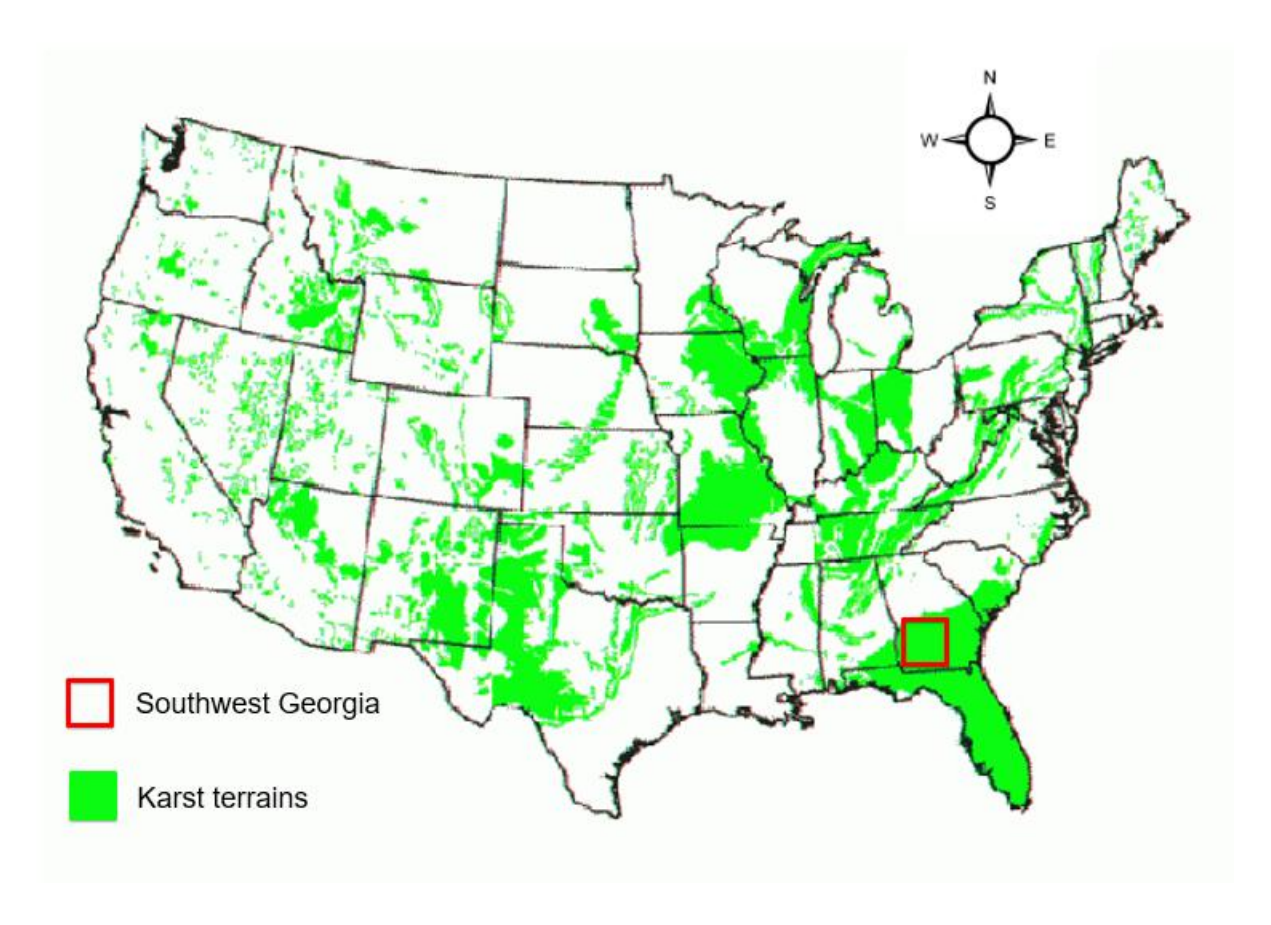


Figure 1.1: Distribution of karst terrains in the United States (modified from Polk et al., 2007).

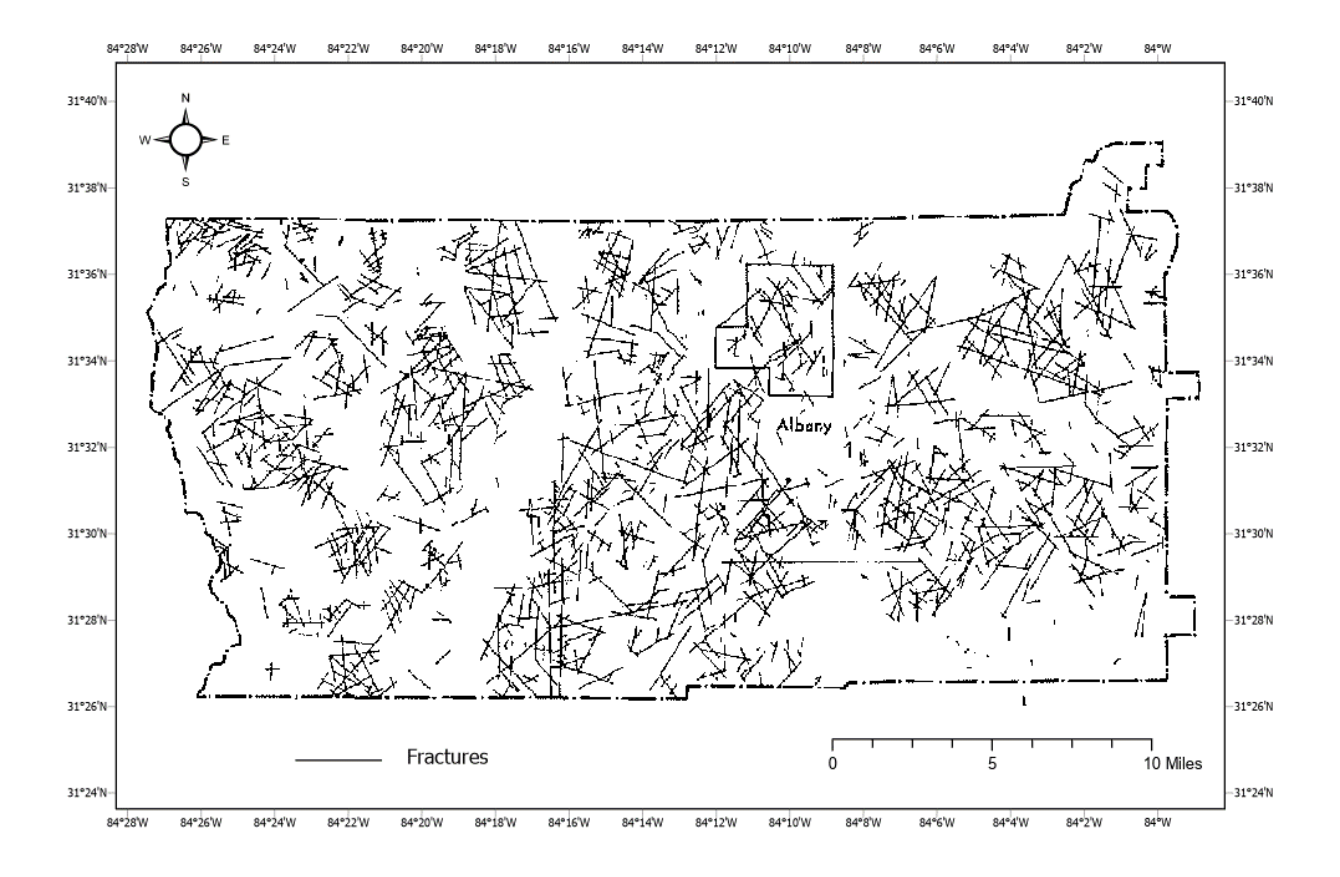


Figure 1.2: Possible fractures in the Ocala limestone mapped for sinkhole data, Dougherty County, Georgia (modified from Brook & Allison, 1983).

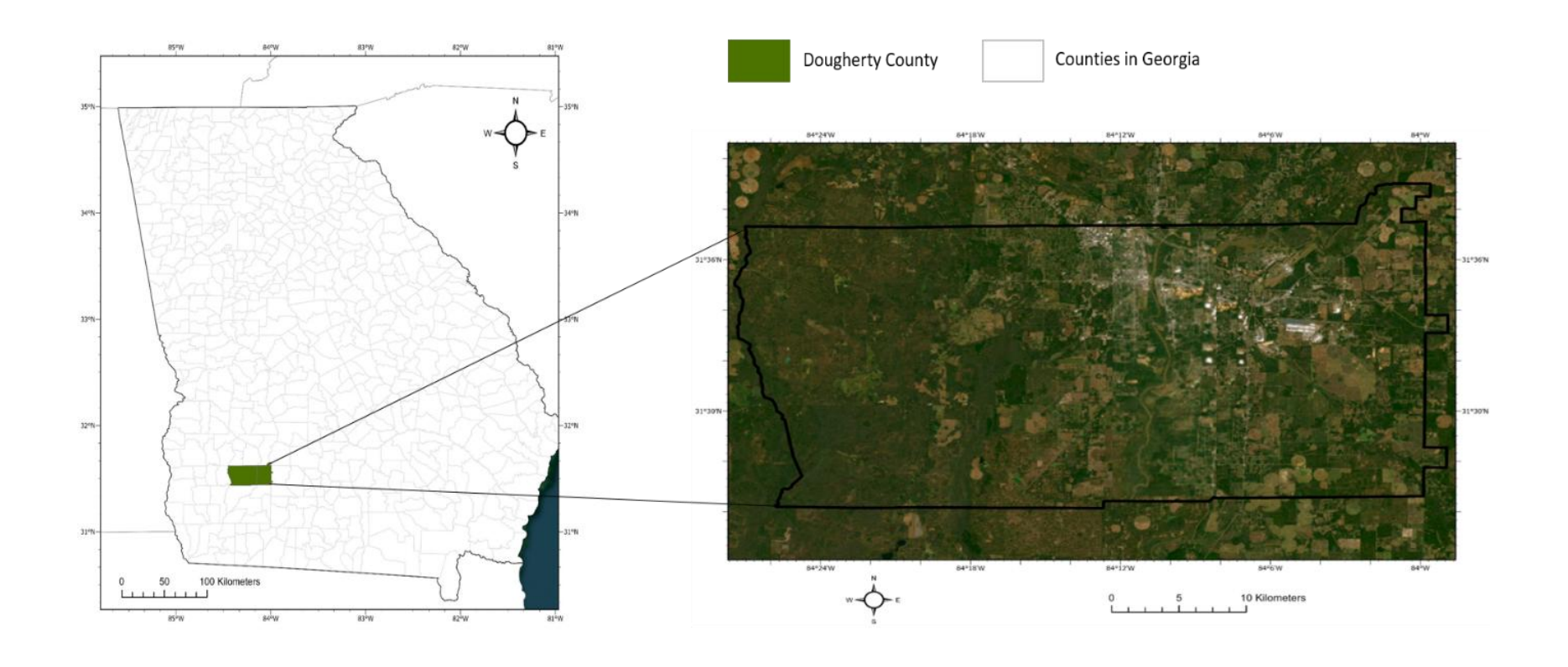


Figure 1.3: Map of Dougherty County, southwest Georgia

Series		G	iroup, formation, and member	Aquifer or confining unit, this rep		
<u> </u>	ocene		Undifferentiated overburden			
Pliocene				Surficial aquifer system/ upper semiconfining unit		
Miocene						
Olig	ocene			dan	Upper water-bearing zone	
	UpperEocene	,	Ocala Limestone	Upper Floridan	Middle unit	
		2	Clinchfield Sand	Upper	Lower water-bearing zone	
Eocene	LowerEocene MiddleEocene	Group	Lisbon Formation		Lisbon confining zone	
		Middle	ClaiborneG roup	Tallahatta Formation		
			Tallahatta Formation (?)		Claiborne aquifer	
	Lov	WilcoxGroup	Bashi Hatchetigbee Fm Hatchetigbee Formation Tuscahoma Formation			
		Manage Parker Par		Wilcox confining unit		
	Paleocene	d.	Porters Creek Formation			
	Pal	MidwayGroup	Clayton Formation		Clayton aquifer	
2		~	Providence	Cla	atyon-Providence confining zone	
Upper			Sand upper unnamed sand member)	Providence aquifer		

Figure 1.4: Generalized lithostratigraphic and hydrostratigraphic units underlying Albany and surrounding areas, southwestern Georgia. Middle Eocene and younger modified from (Hicks et al., 1987), lower Eocene and older modified from (Clarke et al., 1984).

CHAPTER 2

LITERATURE REVIEW

2.1. Background on Lineaments

Lineaments have been of interest to hydrogeologists, geologists, and remote sensing experts for decades now since they may be important geological features (Ahmadi & Pekkan, 2021; Hoffmann & Sander, 2007). The term "lineaments" has been used to describe the mappable linear or curvilinear features on the Earth's surface, which may be identified by several observation methods including field observations, satellite imagery, and aerial photography. This definition given by O'leary et al. (1976) got a lot of citations and laid the groundwork for numerous later studies. Lineaments as detected on remotely sensed imagery and aerial photographs may represent linear drainage pattern anomalies, alignments of topographic features, like ridgelines or straight valley segments, changes in vegetation patterns, or subtle variations in landscape morphology. In many cases, such linear or curvilinear features on the Earth's surface represent the underlying geological structures and hence can be very informative about the subsurface conditions. As stated by Lattman and Parizek (1964), they can manifest at many scales, from a few meters to hundreds of kilometers in length.

However, other studies and works show that lineaments significantly deviate from dominant joints and fractures (Chandra et al., 2006; Acharya & Mallik, 2012; Lattman & Matzke, 1961). This chapter provides a general discussion on the formation and history of lineaments and an overview of various ways lineaments are detected and their hydrogeological significance.

2.1.1. Formation of Lineaments

Geologically related lineaments are formed through various geological processes and can represent different types of structures (Solomon & Ghebreab, 2006).

In the saturated zone, sedimentary rocks such as carbonates and sandstone contain water within their pore spaces. However, the water within their pores is trapped unless there is sufficient connection between the pore spaces. Vertical fracturing in these rocks introduces secondary porosity within them serving as significant preferential pathways for fluid flow (Mazzullo, 2004; Molina et al., 2011). Water from the surface can therefore infiltrate faster through the formation. When the surface water encounters carbon dioxide and organic compounds, weak acids are formed. Limestone and dolomite being carbonate rocks are slightly soluble in these acids (Petersen & Chesters, 1966). Continuous chemical dissolution of the rocks by the weak acids enlarges the water-filled pores and fractures, enhancing the circulation paths. Many of these vertical fractures propagate upward through the rocks and manifest at the surface as shallow depressions, sinks, and leads to changes in soil tonal patterns (Casper et al., 1981; Mollard, 1988). These shallow depressions, sinks, and soil tonal contrasts can be seen on satellite or aerial imagery as linear or curvilinear features commonly interpreted as lineaments (Gay Jr, 2012). Other primary mechanisms for lineament formation include:

1. Tectonic activity: Tectonic activities can induce linear deformations in the landscape making topographic lineaments reliable indicators of faults. Faults can create lineaments in various ways, for example, significant offsets can juxtapose contrasting rocks across a fault, vertical displacements can form linear fault scarps, or highly fractured rocks can lead to increased erosion rates along the fracture trend (Florinsky, 1996; Jacobi, 2002; Terech, 2006).

2. Structural controls: Bedding planes, foliation and other planar structures on rocks can create linear patterns when exposed. These structural discontinuities in rocks result in linear geomorphological features along the intersection of a fracture plane and the land surface. This causes a change in elevation and manifests as linear valleys and linear slope breaks (Jordan et al., 2005).

While many lineaments represent subsurface geological features like fractures and faults, others can be purely surficial features with no direct connection to subsurface geologic structures. Such a distinction is therefore crucial in the interpretation and application of lineament studies (Magowe & Carr, 1999). Non-fracture correlated lineament features can be caused by various surface processes or even human activities. Wind-formed features in arid areas, glacial features like drumlins or eskers (Hess, 2009), man-made linear features like field boundaries or roads, and erosional patterns that do not reflect deeper structures are a few examples of these non-fracture-related lineaments.

2.1.2. Early Studies on Lineaments

The word lineament has become increasingly popular in water resource investigations and structural mapping since the advent of high-altitude aerial images. There are several definitions of the term lineament in literature. These definitions describe the presumed origin of the linear feature or occasionally the source of data from which it was derived (Prabu & Rajagopalan, 2013; Sander, 2007). Hobbs (1904) first used the term lineament to describe the spatial relationships between various landscape features, such as ridge crests or elevated area boundaries, drainage lines, coastlines, boundary lines of formations, petrographic rock types, or outcrop lines. He added valleys or ravines, as well as visible fracture lines or zones of fault breccia, to these features in a

subsequent article in 1912. According to Hobbs, a lineament can be created by joining any number of these features end to end.

Lattman (1958) defined lineaments as natural and curvilinear features consisting of changes in topographic expressions, vegetation patterns, drainage alignments, and soil tonal changes visible on aerial photographs and mosaics. In areas characterized by exposed bedrock where the canopy cover is under 10 percent, Lattman (1958) included bedrock joints in the definition of the terminology. It should be noted that the terms lineaments and fracture traces are used interchangeably since their difference is based on their lengths. Parizek (1976) considered a fracture trace as a linear feature that is less than 1.5 km long and a lineament as a linear feature that is more than 1.5 km long.

Gabrielsen and Braathen (2014) refined the concept of lineaments by introducing the term "fracture lineament" to describe lineaments that can be confirmed as zones with enhanced fracture frequency, likely indicating stress-induced weaknesses in the bedrock, such as fracture corridors (Ogata et al., 2014; Souque et al., 2019) and faults. They emphasized that once the specific nature of a lineament is determined, the terminology should reflect the degree of knowledge available. For example, it should be identified as a "fracture lineament," 'fracture corridor," 'fault," or "dyke" instead of the more generic term "lineament" (Nur, 1982). For over a hundred years, earth scientists have been interested in linear features on the earth's surface since the introduction of aerial photographs and satellite imageries in geological studies and as such analyzing lineaments and fracture traces has been an important area of study (Sander, 2007). Hine (1970) and Parizek (1976) determined that lineaments are the mapped surface expressions of vertical bedrock fractures.

Since the publication of Lattman and Parizek's paper six decades ago, several projects have used lineament mapping as the foundation of groundwater exploration work, especially in complex

geologic environments (Mabee et al., 1994; Minor, 1995; Solomon & Quiel, 2006). Lattman and Parizek (1964) working with thick dolomite and limestone formations, reported that wells drilled on a fracture trace (or lineament) intersect a greater number of cavernous openings than wells drilled in inter-fracture trace areas. These investigations showed that fracture traces or lineaments are good prospecting tools for identifying the high permeability zones within a limestone or dolomite aquifer because they overlie vertical zones with increased solvent activity.

2.1.3. Importance of Fracture–Correlated Lineaments

Fracture-correlated lineaments play a crucial role in water resource investigations for several reasons. In many geological settings, particularly in fractured rock aquifers, lineaments can indicate preferential groundwater flow paths within these aquifers as faults and fracture zones represented by these lineaments often have higher permeability than the surrounding rock mass (Henriksen & Braathen, 2006). They can sometimes represent zones of enhanced recharge, where surface water can more easily penetrate the subsurface (Sander, 2007). According to earlier research by Lattman and Parizek (1964), the intersection of multiple lineaments is often associated with higher groundwater yield potential, making lineament analysis a valuable tool in well-siting studies.

Lineaments can also provide insights into the potential connectivity between different parts of an aquifer system or between surface water and groundwater (Mabee et al., 2002). Understanding lineament patterns can therefore help predict potential contaminant transport pathways in fractured rock environments (Singhal & Gupta, 2010). In carbonate terrains, lineaments often correlate with zones of enhanced dissolution and karst development, which are critical for understanding groundwater flow in these complex systems (Alonso-Contes, 2011).

Lineaments can also be indicators of deep-seated structures that may be associated with geothermal resources (Woodruff Jr & Caran, 1984). In hard-rock areas and karst terrains, the degree and extent of weathering can vary significantly, often influenced by the presence of fractures at depth and surface geomorphological features. Hence in groundwater studies, identifying lineaments and delineating underground fractures are crucial for understanding groundwater flow and development (Mondal et al., 2008).

2.1.4. Methods of Lineament Detection and Analysis

Various methods have been employed in the literature to detect and characterize lineaments. Over the past decade, several papers and reports have presented a wide range of techniques for mapping and analyzing lineaments and their hydrologic properties. These techniques include tectonic models, remote sensing, detailed structural mapping, gravity surveys, and borehole records.

Remote sensing

Remote sensing provides a means for the regional understanding of groundwater systems (Gunawan, 1997). In hard rock terrains, the interpretation of remotely sensed data for lineament mapping is an integral part of groundwater exploration programs (Haryono & Day, 2004). With the benefits of having data spanning broad and inaccessible areas in a short amount of time, remote sensing has emerged as a particularly useful technique for lineament mapping (Mashala et al., 2023). Remote sensing data was used to identify lineaments and pinpoint areas of intense fracturing and fault zones in central and western New York State (McGuire, 2007). Identifying spectral anomalies in vegetation served as a valuable tool for detecting unexposed fracture and

fault systems, as well as fracture-related hydrocarbon reservoirs in the region (Fountain et al., 1999).

Brook and Allison (1983) identified sinkholes based on the presence of surface water features, vegetation, soil moisture patterns, and topographic expression in Dougherty County, southwest Georgia using topographic maps and 1: 24,000 scale, color infrared images. Fractures and joints were delineated using color infrared images and the distribution of the mapped sinkholes.

Digital Elevation Models

Bruning et al. (2011), used remote sensing techniques and derived products such as Digital Elevation Model (DEM) and Landsat TM & ETM+ for geological lineament mapping. Cahalan and Milewski (2018) conducted similar work in Dougherty County by comparing the results of sinkhole inventories formed between 1999 and 2011 from Digital Elevation Models (DEM). A Light Detection and Radar (LiDAR) DEM with a 1 m resolution was used to gather a spatially detailed sinkhole inventory of 3412 sinkholes, which were converted into sinkhole density maps for subsequent analyses. By analyzing topographic data using DEMs, lineaments were revealed through shaded relief maps and drainage pattern analysis (Smith & Wise, 2007). Xu et al., (2016) also used different band combinations and image enhancement techniques to analyze linear features and noted that sinkholes followed a linear pattern. This suggests that joints and fractures also influence sinkhole distribution. Various algorithms and software tools have also been developed for automated lineament extraction, including edge detection methods and the Hough transform (Ahmadi & Pekkan, 2021b; Masoud & Koike, 2006). Despite advances in automated techniques, manual interpretations by experienced geologists remain valuable, especially for complex geological techniques (Wise et al., 1985).

2.1.5. Challenges and Limitations of Lineament Detection and Analysis

While lineaments are valuable features in geological and hydrogeological investigations, there are several challenges and limitations to consider. Manual interpretation of lineaments can be subjective, leading to variations between different interpreters and the detection and significance of lineaments can also vary depending on the scale of observation (Middleton et al., 2015; Scheiber et al., 2015; Tiren, 2010). Moreover, not all linear features represent geological structures, as human-made features or artifacts in imagery can be mistaken for lineaments (Sander, 2007). In heavily vegetated or soil-covered areas, lineaments may be obscured and may not be consistently detectable (Hashim et al., 2013). Distinguishing between lineaments that represent subsurface features and those that are purely surficial can therefore be challenging. It often requires additional data and investigation beyond remote sensing or surface observation. Geophysical surveys and borehole data may be necessary to confirm the nature of lineaments.

2.1.6. Geophysical Surveys as A Tool to Validate Lineaments

The likelihood of lineaments representing subsurface structural features can vary by region and geological setting. Lineaments are more likely to reflect underlying structures in areas of exposed bedrock or thin soil cover (Carruthers et al, 1991). In areas with thick sedimentary cover or complex surface processes, underlying transmissive features can consequently go undetected to the large extent of lineament investigations using surface geophysical techniques (Sander, 2007).

In water resource investigations the combination of remote sensing and geophysical techniques (surface and borehole), therefore, constitutes a valuable approach to exploring the subsurface continuity of geological features observed on remote sensing images such as lineaments

(Eze, 2024). There is a growing body of literature that recognizes the wide number of advantages that geophysical techniques have in imaging subsurface geological characteristics.

2.2. Background on Geophysical Methods

Traditional approaches to subsurface field investigations include borehole drilling and soil sampling, monitoring wells, exploratory trenches, piezometric measurements, and water sample analysis (Lutenegger, 2021). These approaches involve taking a significant number of samples to ensure a reasonable level of accuracy and certainty. Furthermore, these techniques are invasive, modify water circulation, are expensive to carry out, and cannot be achieved in relatively high resolution (Butler, 2005). To optimize these traditional approaches of subsurface characterization, there is a need for a cost-effective reconnaissance technique that provides rapid, continuous spatial coverage and reduces the risk of contamination associated with conventional subsurface assessment techniques. These cost-effective reconnaissance techniques are known as geophysical methods (Benson et al., 1982; Frost & Burns, 2003). They have the potential to enhance hydrogeological characterization when there is an effective correlation between geophysical and hydrogeological properties (Linde et al., 2006). Geophysical techniques, however, cannot replace sampling completely, because background information is needed on each new hydrogeologic environment to aid data analysis and interpretation.

Geophysics deals with the physical processes and properties of the Earth, the atmosphere, and its surrounding space environment. Geophysical measurement systems have a wide range of techniques, applied to fields such as space exploration, geothermal exploration, water resource investigations, archaeological investigations, earthquake monitoring, and mineral exploration

(Gaffney, 2008; Goldman & Neubauer, 1994; Hoover et al., 1995; Kana et al., 2015). There are different types of geophysical measurement systems, and they can be categorized into surface and subsurface geophysical techniques. Surface geophysics provides area-wide coverage for subsurface characterization employing techniques such as electrical resistivity method, ground penetrating radar, seismic refraction and reflection, gravity method, and electromagnetic methods (Alhassan et al., 2018; Barrett et al., 2002; Buselli & Lu, 2001; Endres et al., 2000). Subsurface geophysics, on the other hand, involves the measurement of petrophysical properties of borehole traversed or penetrated formations as sensing devices are lowered down the well bore. The measured parameters may be interpreted in terms of the characteristics of the rocks, and the fluids that are contained within them (Keys & MacCary, 1971). These surface geophysical methods can also be subdivided into active and passive systems. In active geophysical surveys, a signal is injected into the earth, and the earth's response to this signal is monitored. Passive geophysical surveys, on the other hand, measure naturally occurring fields or properties of the earth (Piroddi et al., 2021).

2.2.1. Categories of Geophysical Methods

Geophysical methods can be broadly categorized based on the physical properties they measure and the techniques they employ to investigate the subsurface. Table 2.1 shows the various geophysical methods and the physical properties they measure (Bechtel et al., 2014; Erkan, 2008; Foulger & Pierce, 2007). This study focused on using the Electrical Resistivity method for subsurface characterization.

2.2.2. Electrical Resistivity Method

The advent of electrical resistivity measurements for subsurface exploration can be traced back to 1912 when Conrad Schlumberger conducted pioneering experiments in Normandy, France. Initially adopted by the petroleum industry for reservoir characterization and geological formation analysis, electrical resistivity methods have since evolved into a fundamental geophysical technique (Sharma, 1997). The electrical resistivity method has since then been employed to investigate vertical and horizontal discontinuities in the electrical properties of subsurface materials (Zarroca et al., 2011). The principle involves injecting direct current into the ground via surface electrodes and measuring the resulting potential difference (Binley & Slater, 2020). The resistivity of a material, defined as its opposition to current flow, serves as a diagnostic tool for distinguishing subsurface layering and structures (Knödel et al., 2007).

The sensitivity of the resistivity method to variations in electrical conductivity arises from the inherent contrast between different subsurface materials (Mickus, 2021). Geological formations, including sedimentary (e.g., clay, sand, gravel), metamorphic, and igneous rocks, exhibit a wide range of resistivity values. In unconsolidated sediments, resistivity is primarily influenced by granulometric composition and the presence of water or clay. Conversely, in consolidated rocks, resistivity is modulated by factors such as water- or clay-filled interstices, degree of fracturing or karstification, and lithological composition. Additionally, pore fluid salinity can significantly affect the bulk resistivity of rock formations (Barrett et al., 2002; Telford et al., 1990a) The ability of electrical resistivity methods in delineating near-surface geological features, such as faults and fractures, stems from the resistivity anomalies these structures often present relative to the surrounding rock matrix. These anomalies are frequently associated with the

presence of fluids or mineralization within the discontinuities (Gelis et al., 2016; Obiadi et al., 2012; Szalai et al., 2018).

Recent advancements in data acquisition systems, inversion algorithms, and 3D visualization techniques have further enhanced the resolution and interpretability of electrical resistivity surveys. These developments have expanded the application of resistivity methods beyond traditional geological mapping to include environmental monitoring, hydrogeological characterization, and geotechnical investigations (Chambers et al., 2015; Loke et al., 2013). Moreover, the integration of electrical resistivity tomography (ERT) with other geophysical methods, such as seismic refraction or ground-penetrating radar, has led to more robust and comprehensive subsurface characterization. This multi-method approach allows for the mitigation of inherent limitations associated with individual techniques and provides a more holistic understanding of complex geological environments (Gallardo & Meju, 2011; Garambois et al., 2002). Electrical resistivity methods have also evolved from their early applications in petroleum exploration to become an indispensable tool in various earth science disciplines. Their noninvasive nature, coupled with continuous advancements in technology and data interpretation, ensures their continued relevance in addressing complex subsurface characterization challenges across diverse geological settings (Pradipta et al., 2025; D. A. Robinson et al., 2008).

Table 2.1: Geophysical methods and the characteristic physical properties they measure.

Geophysical Method	Physical Property		
Seismic	Travel time of sound waves		
Gravity	Earth's gravitational field		
Electromagnetic	Electrical conductivity		
Radiometric	Natural or artificial radiation emitted		
Magnetic	Earth's magnetic field		
Thermal	Subsurface temperature or heat flow		
Electrical Resistivity	Electrical properties of the subsurface		

2.2.2.1. Basic Concepts About Resistivity

In geophysics, electrical resistivity studies can be understood as the investigation of current flow (Figure 2.1) through subsurface materials composed of multiple layers, each characterized by distinct resistivities (Herman, 2001). In 1827, Georg Simon Ohm derived an empirical relationship between resistance R of a resistor in ohms, current (I) in amperes, and the corresponding change in potential (V) in volts, expressed as:

$$V = IR \tag{1}$$

This relationship, widely recognized as Ohm's law, defines resistance as the property of the resistor that describes how much it resists the passage of current for a given applied potential difference. Generally, a high resistance will only give a small current (I) for a given potential difference V, and vice versa. Resistance is dependent on the physical dimensions of the material or sample. To remove the effect of the dimensions of the material or sample, resistance is expressed

per unit length and cross-sectional area, yielding a value called resistivity. Resistivity therefore depends solely on the property of the material and is independent of its dimensions (Christensen, 2000).

In physics, resistivity is frequently introduced when discussing the resistance of current flow through an ideal cylinder of cross-sectional area A and length L of uniform composition (Figure 2.2). The resistivity ρ , an intrinsic property of the material is related to the total resistance of the cylinder in the expression (Herman, 2001),

$$R = \rho \frac{L}{A} \tag{2}$$

where R is resistance in ohms, ρ is resistivity in ohm.m, L is length in meters and A is area in squared meters.

This equation can be rearranged and expressed as:

$$\rho = \frac{R.A}{L} \tag{3}$$

The current (*I*) flowing through a circuit is influenced by the resistance of the conductor. For a cylindrical bar, the resistance R is directly proportional to its length L, and inversely proportional to its cross-sectional area A. This relationship can be expressed as:

$$\rho = \frac{V \times A}{I \times L} \tag{4}$$

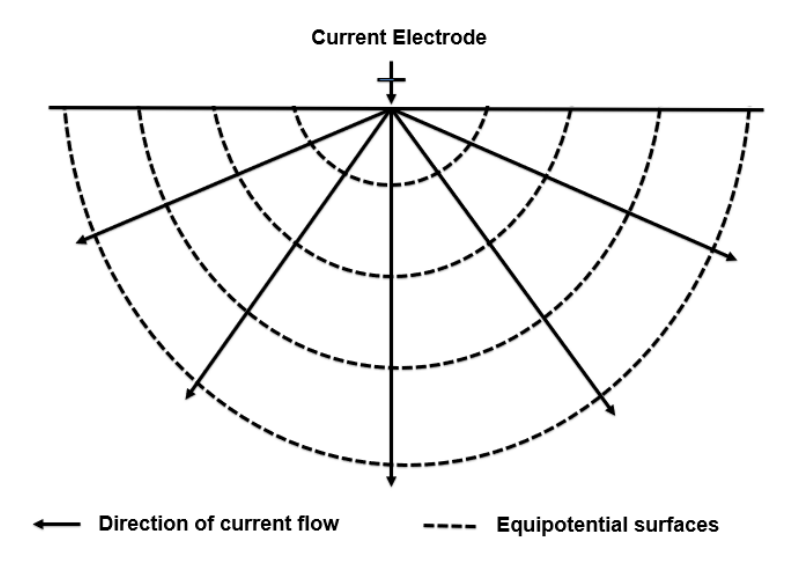


Figure 2.1: The flow of current from a point source and the resulting equipotential surfaces in a level field with homogeneous subsurface structure (modified from Loke, 2001).

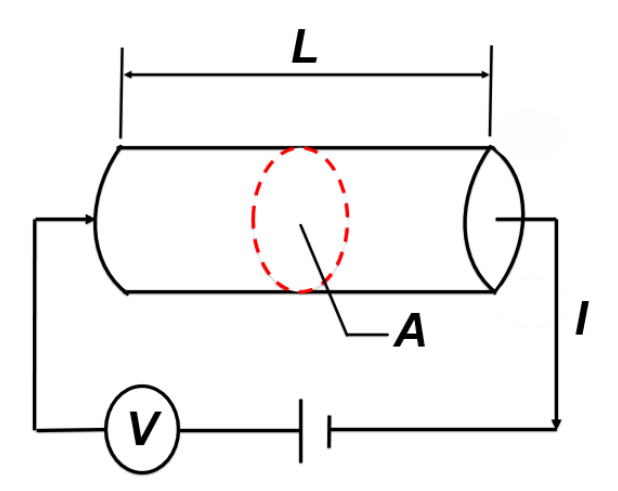


Figure 2.2: A schematic representation of Ohm's Law showing an electric circuit consisting of a resistor and a battery with current flowing through a cylindrical material (modified from Nadia, 2012).

2.2.2.2. Theoretical Determination of Apparent Resistivity

In the theoretical determination of apparent resistivity, several assumptions are made to simplify the Earth model. The Earth is assumed to be uniform and homogeneous, with constant resistivity throughout its extent. Also, the earth is assumed as a hemispherical resistor in a basic electrical circuit comprising two electrodes designated as sink and source electrodes that are inserted into the ground and a battery as shown in Figure 2.3 (Aizebeokhai, 2010). These assumptions, while useful for theoretical calculations, may not fully account for the complexity of natural subsurface conditions.

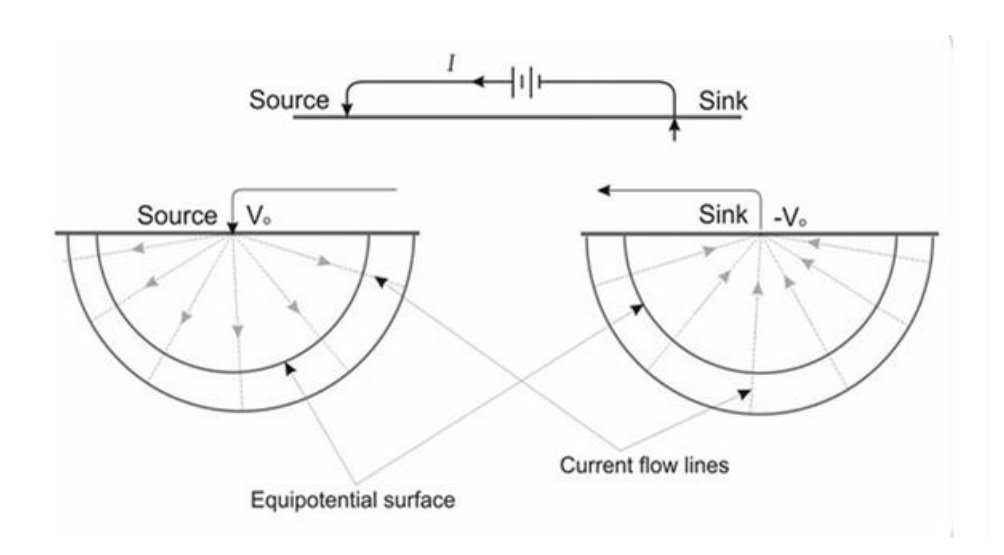


Figure 2.3: Current lines radiating from the source electrode and converging on the sink (modified after E. S. Robinson, 1988).

When electrical current is introduced into the ground, it disperses radially outward from the source electrode. Assuming the Earth is a homogeneous model, the current propagates uniformly in all directions, forming a hemispherical distribution around the electrode. At any given point, the current front advances through the hemispherical zone. The area of such a zone can be expressed with the relationship;

$$A = 2\pi r^2 \tag{5}$$

where r is the radius of the hemisphere (half the distance from the source electrode to the point on the hemisphere surface in Figure 2.3).

Substituting equation 5 into equation 4, the potential (V) at a point due to a current source (I) at a distance, r, away from the point in a medium of resistivity, p, is expressed as:

$$V = \frac{I\rho}{2\pi r} \tag{6}$$

For current to flow, there must be a source (+I) and sink (-I) creating a circuit. The total potential (V_{P1}) at a given point (P_1) resulting from the current flow is obtained by summing the potentials caused by both the source and sink (Figure 2.4).

The potential at P_1 due to the source (+I) at distance r_1 is:

$$V_{P1} = \frac{I\rho}{2\pi r_1} \tag{7}$$

The potential at P_1 due to the source (-I) at distance r_2 is:

$$V_{P1} = -\frac{I\rho}{2\pi r_2} \tag{8}$$

Thus, the total potential at P_1 is given as:

$$V_{P1} = \frac{I\rho}{2\pi} \left(\frac{1}{r_1} - \frac{1}{r_2} \right) \tag{9}$$

where r_1 and r_2 are the respective distances of the source and sink currents from the potential point, P_1 .

Similarly, the total potential (V_{P2}) at a point (P_2) resulting from the same current flow, where the source and sink are at distances r_3 and r_4 from the point, respectively can be expressed as:

The potential at P_2 due to the source (+I) at distance r_3 is:

$$V_{P2} = \frac{I\rho}{2\pi r_3} \tag{10}$$

The potential at P_2 due to the source (-I) at distance r_4 is:

$$V_{P2} = -\frac{I\rho}{2\pi r_4} \tag{11}$$

Thus, the total potential at P_2 is given as:

$$V_{P2} = \frac{I\rho}{2\pi} \left(\frac{1}{r_3} - \frac{1}{r_4} \right) \tag{12}$$

The potential difference across the points P_1 and P_2 resulting from the current flow can be expressed as:

$$\Delta V = V_{P1} - V_{P2} = \frac{I\rho}{2\pi} \left(\frac{1}{r_1} - \frac{1}{r_2} - \frac{1}{r_3} + \frac{1}{r_4} \right)$$
 (13)

$$\Delta V = \frac{I\rho}{2\pi} \left(\frac{1}{r_1} - \frac{1}{r_2} - \frac{1}{r_3} + \frac{1}{r_4} \right) \tag{14}$$

Making resistivity p, the subject,

$$p = 2\pi \frac{\Delta V}{I} \left(\frac{1}{r_1} - \frac{1}{r_2} - \frac{1}{r_3} + \frac{1}{r_4} \right)^{-1}$$
 (15)

and if $G = \left(\frac{1}{r_1} - \frac{1}{r_2} - \frac{1}{r_3} + \frac{1}{r_4}\right)$ is the geometric factor

Then,
$$\rho = 2pG^{-1}\frac{\Delta V}{I}$$
 (16)

where the coefficient of geometry, $K = 2\pi G^{-1}$.

The coefficient of geometry therefore varies by array and depends on the electrode spacing and arrangement of the potential and current electrodes. The Earth's crust is neither homogeneous nor isotropic, it exhibits varying physical properties, hence assuming uniform resistivity is unrealistic (Binley & Slater, 2020; Naif et al., 2021). The resistivity measured in the field represents an average resistivity derived from the resistivity distribution between two equipotential surfaces. This average resistivity is referred to as the apparent resistivity, p_a . Equation 11 is now written as:

$$\rho_a = K \frac{\Delta V}{I} \tag{17}$$

The apparent resistivity is influenced by several variables including the lithological characteristics of the subsurface materials, moisture content, and the configuration of the electrode array (Bakar et al., 2024). The true resistivity distribution within the subsurface can be estimated from the apparent resistivity by an inversion procedure based on the minimization of a suitable function to derive a model that best fits the measured data (Olayinka & Yaramanci, 2000).

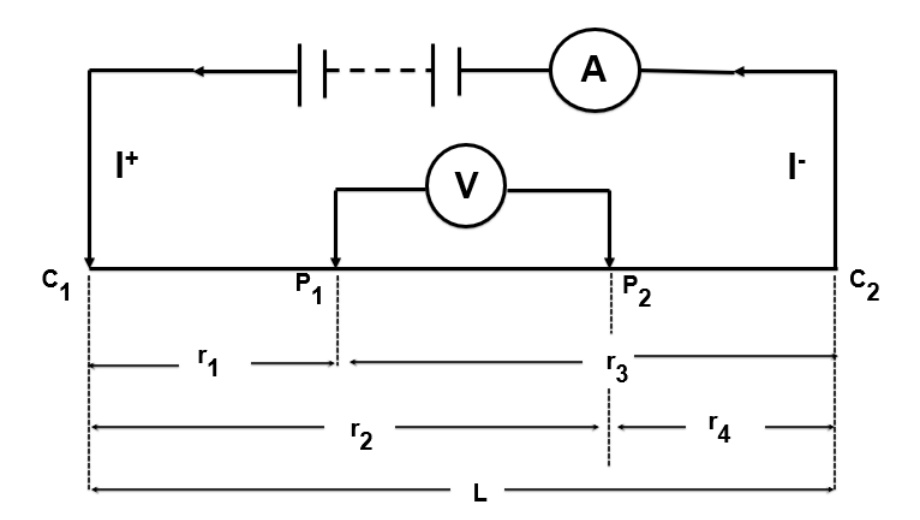


Figure 2.4: Generalized form of electrode configuration in resistivity survey used in generating the apparent resistivity in equation 11, $C_1P_1 = r_1$, $C_1P_2 = r_2$, $C_2P_1 = r_3$, $C_2P_2 = r_4$. (modified from Soge et al., 2019).

2.2.2.3. Electrical Resistivity with Its Structural and Lithological Relationships

Electric current propagation through subsurface materials occurs via two primary mechanisms: electrical conduction and electrolytic conduction (Robinson, 1988). Electrical conduction involves the movement of free electrons, typically observed in metallic substances, while electrolytic conduction is characterized by ionic movement within groundwater (Binley & Slater, 2020). In the field of engineering geophysics, electrolytic conduction is the predominant mechanism. However, electrical conduction becomes significant in the presence of conductive minerals such as metal sulfides and graphite.

The electrical resistivity of igneous and metamorphic rocks is highly dependent on the degree of fracturing and the proportion of fractures filled with groundwater (Godfray & Tembo, 2024). Depending on the amount of water within a rock, a given rock type can have a large range of resistivity values. These resistivity properties are valuable in the delineation of fractures and other weathering features within the subsurface (Loke, 2004). Geological structures such as joints and fractures commonly manifest on resistivity model sections as vertical electrical resistivity contrasts. These zones of increased permeability and porosity promote increased weathering and water infiltration. This results in altered electrical properties in comparison with the surrounding intact rock units (Fazzito et al., 2009). Faults are characterized in resistivity sections either by sharp contrasts due to the juxtaposition of materials with distinct electrical properties or by flexed patterns in resistivity resulting from offsets within a unit along a fault plane (Galli et al., 2014).

Analysis of resistivity across the three major rock types reveals that sedimentary rocks generally exhibit lower resistivity values than igneous and metamorphic rocks. This is attributed to the typically higher porosity and water content of sedimentary rocks (Tiab & Donaldson, 2024). Resistivity values are therefore largely dependent on rock porosity and the salinity of interstitial

fluids. Unconsolidated sediments, such as clay and sand, generally display lower resistivity compared to consolidated sedimentary rocks. Moreover, clay soils typically exhibit lower resistivity values than sandy soils due to their higher water retention capacity and ionic content (Chik & Islam, 2012).

The resistivity of common rocks, soil materials, and chemicals is shown in Figure 2.5. This table, along with data from borehole geophysical logs and results from previous resistivity works serves as a guide to interpreting possible lithologies within the subsurface.

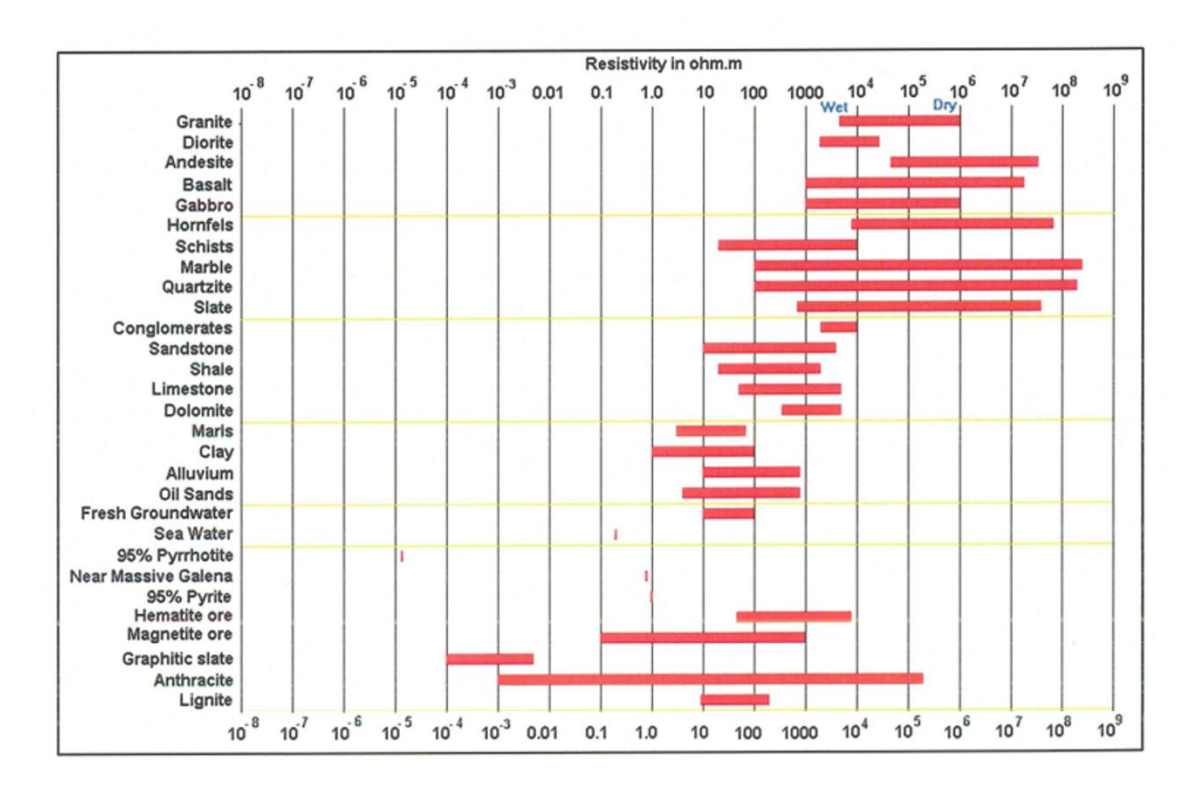


Figure 2.5: Resistivity of common rocks, soil materials, and chemicals (modified from Loke, 2011).

2.2.2.4. Electrical Resistivity Survey Methods

Electrical resistivity data acquisition employs a diverse array of survey methodologies, each tailored to specific investigative requirements. The selection of an appropriate survey method depends on several factors, including the type of information desired, the dimensional complexity of the interpretative model (1D, 2D, or 3D), and the cost-effectiveness of the proposed approach. The main surface-based electrical resistivity survey methods include Horizontal Electrical Profiling (HEP), Vertical Electrical Sounding (VES), and Electrical Resistivity Tomography (ERT) (Botha, 1975; Hasan et al., 2020; Markos et al., 2021).

Vertical Electrical Sounding (VES) provides one-dimensional (1D) resolution of resistivity data at varying depths beneath a single surface location. In VES, the electrode configuration is systematically adjusted symmetrically around a central measurement point, allowing for the vertical delineation of subsurface electrical properties (Coker, 2012). This method is suitable in horizontally stratified environments where lateral variations are minimal as it does not take into account horizontal changes in subsurface resistivity. Horizontal Electrical Profiling (HEP) on the other hand, provides information about the lateral variations in subsurface electrical resistivity (Storz et al., 2001). By maintaining a fixed electrode spacing and moving the entire array along a profile, HEP helps in the detection of horizontal discontinuities and anomalies within a consistent depth range. This approach is valuable for mapping lateral changes in lithology or identifying subsurface features such as buried channels or fault zones.

Electrical Resistivity Tomography (ERT) is an advanced geophysical method that synthesizes aspects of both VES and HEP, providing comprehensive information about vertical and lateral resistivity variations within the subsurface (Zarroca et al., 2011). The geophysical

technique employed in this study is Electrical Resistivity Tomography, which will be discussed in detail.

2.2.2.5. Electrical Resistivity Tomography in Karst Environments

Electrical resistivity tomography, ground penetrating radar, and seismic methods are the most used active source geophysical methods for subsurface characterization in karst terrains (Montane, 2001; Schmelzbach et al., 2015; Verdet et al., 2020). Ground penetrating radar (GPR) which uses radar pulses to image the subsurface is less preferred among the three. The depth of investigation of GPR is extremely limited as the signals can be highly attenuated in soils with high electrical conductivity, which is often due to elevated clay and moisture content (Chalikakis et al., 2011). Such soils are prevalent in Dougherty County, southwest Georgia. Investigated soils, bedrock, and air or water-filled voids should have sufficient contrast in the dielectric properties to be precisely identified by the GPR method (Rodriguez et al., 2014). GPR signals also generally penetrate between 5 – 10 m deep, usually not deep enough to image bedrock in karst environments (Dobecki & Upchurch, 2006). Electrical resistivity tomography, however, provides greater depth of investigation.

Advancements in resistivity techniques using multi-electrode arrays have significantly enhanced electrical imaging for subsurface investigations. Over the past decade, Electrical Resistivity Tomography (ERT) has emerged as a reliable and widely used technique for hydrogeological, geotechnical, and environmental engineering studies (Griffiths & Barker, 1993). ERT is extensively employed across various applications, including determining the depth of bedrock, locating contaminated plumes, delineating the elevation of the groundwater table, monitoring and modeling soil-plant interactions, detecting buried objects in archaeological sites,

rock mass quality evaluation, and monitoring environmental remediation processes. These surveys are usually carried out using multiple electrodes connected through a multi-core cable (Barker, 1981). This generates 2D and 3D images of electrical resistivity variations of the subsurface (Zhou et al., 2000). Electrodes (current pairs) are planted into the ground to create an electrical field and other pairs of electrodes (potential) measure the potential difference away from the source. In a multi-electrode array, apparent resistivity measurements are sequentially recorded by switching between multiple electrode combinations. This process measures the resistivity distribution variations at shallow depths within pseudosections, producing high-density data acquisition in a short timeframe. This allows the detailed interpretation of 2D resistivity distribution within the subsurface (Loke & Barker, 1996). By conducting these measurements in different electrode geometries, it is possible to evaluate or delineate the resistivity of the subsurface (Cheng et al., 2019). The Electrical Resistivity Tomography technique enables the detection zones of anomalous subsurface resistivity or conductivity. An unfilled fracture or cave is likely to be a zone of nearinfinite resistivity (Telford et al., 1990). In some cases, if a fracture in a limestone is filled with water or clay, it may be a better electrical conductor than the surrounding rock. For these reasons, fractures and caves can be expected to have anomalous electrical resistivities compared to the rest of the formation (Van Schoor, 2002).

In karst environments, the ERT technique is often used to determine the depth-to-bedrock, locate fracture zones, and locate air-filled cavities, which are often depicted by high contrast in resistivity (Nyquist et al., 2007). ERT has been used extensively in karstic environments and it is the preferred method for subsurface characterization in karst terrains (Fields Jr et al., 2022), especially when the overburden is a clay-rich soil. The high contrast in resistivity between carbonate rock and clayey soil makes the resistivity technique effective for identifying the soil-

bedrock interface. Zhu et al., 2011, employed various ERT methods, including time-lapse approaches, to detect karst conduits, and Carrière et al., 2013 and Martínez-Moreno et al., 2014 integrated ERT with Ground Penetrating Radar (GPR) to identify fractures and conduits in karst regions. (Zhou et al., 2002), studied the reliability of ERT for mapping the bedrock in covered karst terrain and noted general limitations of ERT, such as averaging of resistivity data values representing a bulk geological material and uncertainty in contouring of small-scale inconsistencies in the geologic interfaces. The authors concluded that various geological environments could produce similar distributions of calculated apparent resistivity.

2.2.2.6. Electrode Arrays Used in ERT Surveys

The 2D ERT is affected by the electrode configuration and the spacing between the electrodes. Commonly used electrode arrays for resistivity surveys include the dipole-dipole, Wenner, Schlumberger, pole-pole, and Wenner-Schlumberger arrays. Table 2.3 compares the various electrode arrays, their advantages, limitations, and suitable applications. When selecting an array for a proposed study, it is important to consider factors such as the depth of investigation, the sensitivity of the array to lateral and vertical changes in subsurface resistivity distribution, horizontal data coverage, and the signal-to-noise ratio of the array (Mirzaei et al., 2021; Neyamadpour et al., 2010).

In every electrical resistivity survey, the depth of investigation (DOI) is an important parameter and it is influenced by factors such as the array type, electrode spacing and separation, contrasts between subsurface materials, data coverage, and the signal-noise ratio (Robinson, 1988). The depth of investigation is the depth below which features seen on the resistivity profile are not controlled by the resistivity data. Generally, the depth of investigation increases as the distance

between the first and last electrodes in a survey setup is increased. The farther, the first and last electrodes are apart, the greater the distance in which the bulk of the current flows within the subsurface. Table 2.2, lists the mean depth of investigation for the different arrays used in electrical resistivity surveys.

Given a set of 56 electrodes spaced at 3 m intervals, the total length of the survey line would be 165 m. The depth of investigation for the dipole-dipole and Wenner arrays in a first-order approximation would be 20% of the total length of the survey line. The total depth of penetration for a 165 m long survey would be 33 m. However, when there is higher heterogeneity in resistivity near-surface, the actual depth of investigation may be different as these depth models are good enough for planning field surveys because it is strictly valid for a homogeneous earth model. The depth of investigations from (Edwards & Hillel, 1977) is provided as factors relative to the characteristic length of the array. While these depths may be helpful as guidelines in the design of the survey, they do not quantify the depth to which the features in the inverted section can be interpreted (Oldenburg & Li, 1999).

In 2D electrical resistivity surveys, the sensitivity of different electrode arrays also varies based on their geometry and configuration. This has an effect on the resolution, depth of investigation, and the ability of these electrode arrays to detect subsurface features. The sensitivity function gives information about the extent to which variations in subsurface resistivity affect the potential measured by the electrode array. Sensitivity patterns for these different arrays are shown in Figure 2.6. Subsurface regions with higher sensitivity values have a greater influence on the recorded measurements. Generally, for all electrode arrays, sensitivity values are observed to be highest in areas closer to the electrodes (Loke, 2004). The three most common electrode arrays Wenner, Schlumberger, and Dipole-Dipole, will be discussed further in this study.

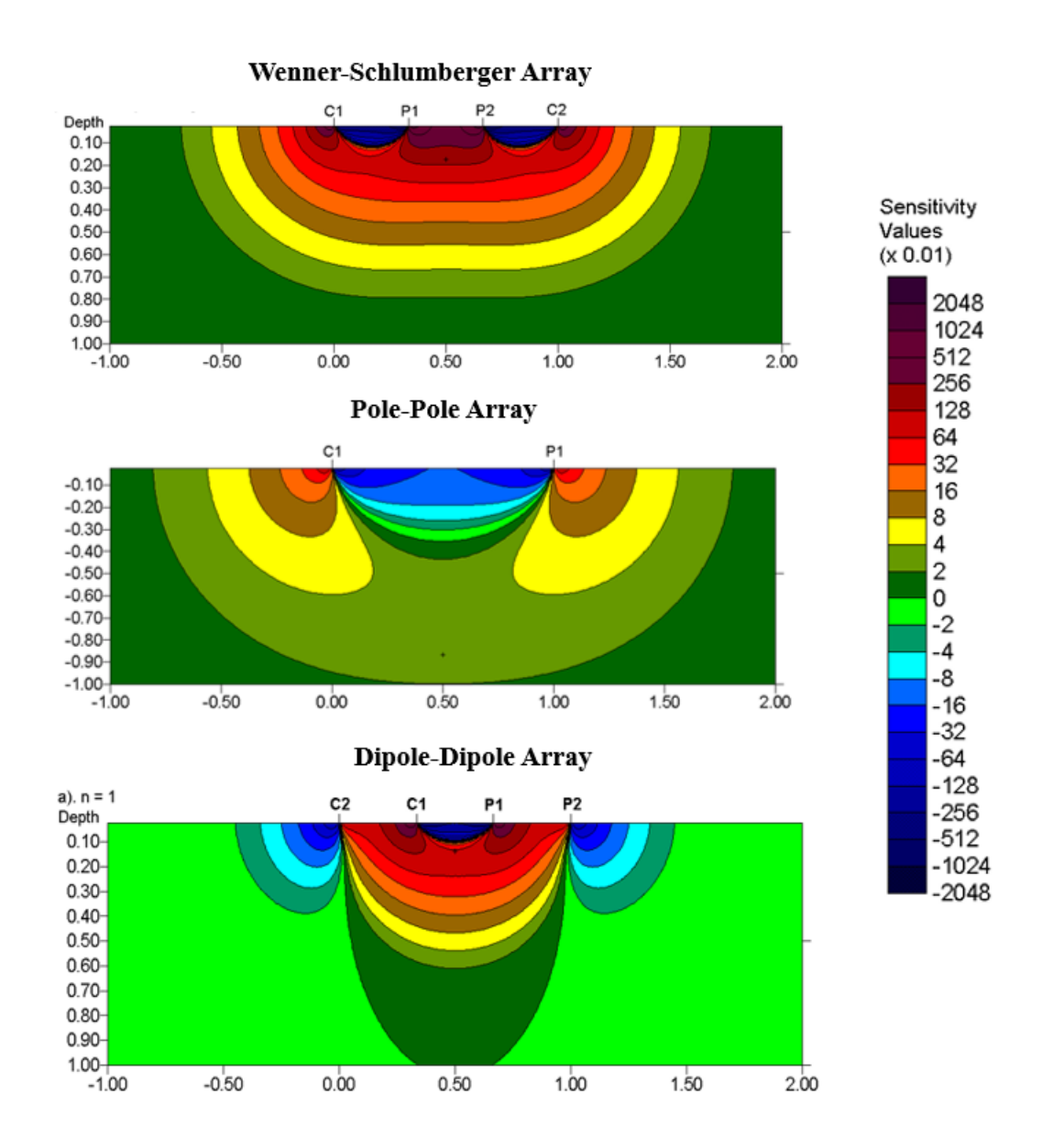


Figure 2.6: 2-D sensitivity section for different electrode arrays (modified after Loke, 2011).

Table 2.2: Mean depth of investigation (z_e) for the different arrays used in electrical resistivity surveys. L is the total length of the survey (Edwards, 1997).

Array type	z _e /a	z _e /L
Wenner alpha	0.519	0.173
Dipole-Dipole		
n = 1	0.416	0.139
n = 2	0.897	0.174
n = 3	0.962	0.192
n = 4	1.220	0.203
n = 5	1.476	0.211
n = 6	1.730	0.216
Equatorial dipole-dipole		
n = 1	0.451	0.319
n=2	0.809	0.362
n = 3	1.180	0.373
n = 4	1.556	0.377
Wenner - Schlumberger		
n=1	0.52	0.173
n = 2	0.93	0.186
n = 3	1.32	0.189
n = 4	1.71	0.190
n = 5	2.09	0.190
n = 6	2.48	0.190
Pole-dipole		
n = 1	0.52	
n = 2	0.93	
n = 3	1.32	
n = 4	1.71	
n = 5	2.09	
n = 6	2.48	
Pole-Pole	0.867	

Wenner Array

The Wenner electrode array (Figure 2.7a) consists of four electrodes arranged in a straight line with equal spacing between them. In this array, two potential electrodes (P1 and P2) are positioned between two current electrodes (C1 and C2), with a uniform distance 'a' between

adjacent electrodes. While there are three types of Wenner arrays; the alpha, beta, and gamma, the Wenner alpha configuration is the most used in practice. To explore greater or deeper depths within the subsurface, the spacing 'a' between the electrodes is progressively increased while maintaining a fixed center point. However, for increasing lateral explorations, the electrode array spacing remains constant as the entire array is shifted along the survey line (Loke, 2004).

This array is relatively sensitive to vertical changes in subsurface resistivity, particularly beneath the center of the array. This makes it effective at detecting horizontal structures. The Wenner array also has strong signal strength compared to other electrode arrays. However, it has limited sensitivity to horizontal resistivity changes and is less effective at identifying narrow vertical structures (Milson & Eriksen, 2013). The geometric factor of the Wenner array is given by the expression:

$$\rho_{a} = (2\pi a) \frac{V}{I} \tag{18}$$

Schlumberger Array

In the Schlumberger array (Figure 2.7b), the potential electrodes are sandwiched between the outer current electrodes, however, unlike in the Wenner array, the electrode pairs are not equally spaced. The outer current electrodes are commonly set apart at a distance at least five times greater than the spacing between the potential electrodes. The two interior potential electrodes are spaced symmetrically between the two current electrodes, in such a way that, they are more closely together in the center of the array (Aspinall & Gaffney, 2001). The Schlumberger array is commonly used for VES surveys as it provides better horizontal resolution and is less time-consuming compared to the other arrays. During the VES surveys, the current electrodes are progressively moved outward to greater separations while the potential electrodes remain fixed at

the center. This configuration continues until the measured voltage becomes too small for accurate readings (Ohaegbuchu et al., 2019). The apparent resistivity can be calculated for this array from this equation:

$$\rho_{a} = \left[\frac{\pi(L^{2} - l^{2})}{2l}\right] \frac{V}{I} \tag{19}$$

Dipole-Dipole Array

The dipole-dipole (D-D) electrode array (Figure 2.7c) uses two electrode pairs: one for current injection and the other for potential measurement. Each pair has equal internal spacing but unlike the Wenner and Schlumberger arrays, these pairs can be arranged in various ways. The most common dipole-dipole configuration is the collinear arrangement (CCPP or ABMN), where two current electrodes are followed by two potential electrodes along as single line (Al Hagrey, 2012). In this system of arrangement, the spacing between the current electrode pair (C2-C1) and the potential electrode pair (P1-P2) is denoted as 'a'. A key parameter in this array is the 'n' factor, which represents the ratio of the distance between C1 and P1 to the dipole length 'a' (Griffiths & King, 2013). For surveys using this array, the dipole length 'a' is typically maintained at the smallest unit electrode spacing, while the 'n factor is increased sequentially from 1 until up to 6 to achieve greater depths of investigation. The dipole-dipole array is relatively suitable for detecting vertical structures due to its sensitivity to horizontal changes in subsurface resistivity between the electrodes in each dipole pair. However, it has low signal-noise ratio and is less sensitive to vertical changes in subsurface resistivity (Loke, 2004). The apparent resistivity can be calculated for this array from this equation:

$$\rho_{a} = \pi n(\pi + 1)(\pi + 2)a\frac{V}{I}$$
 (20)

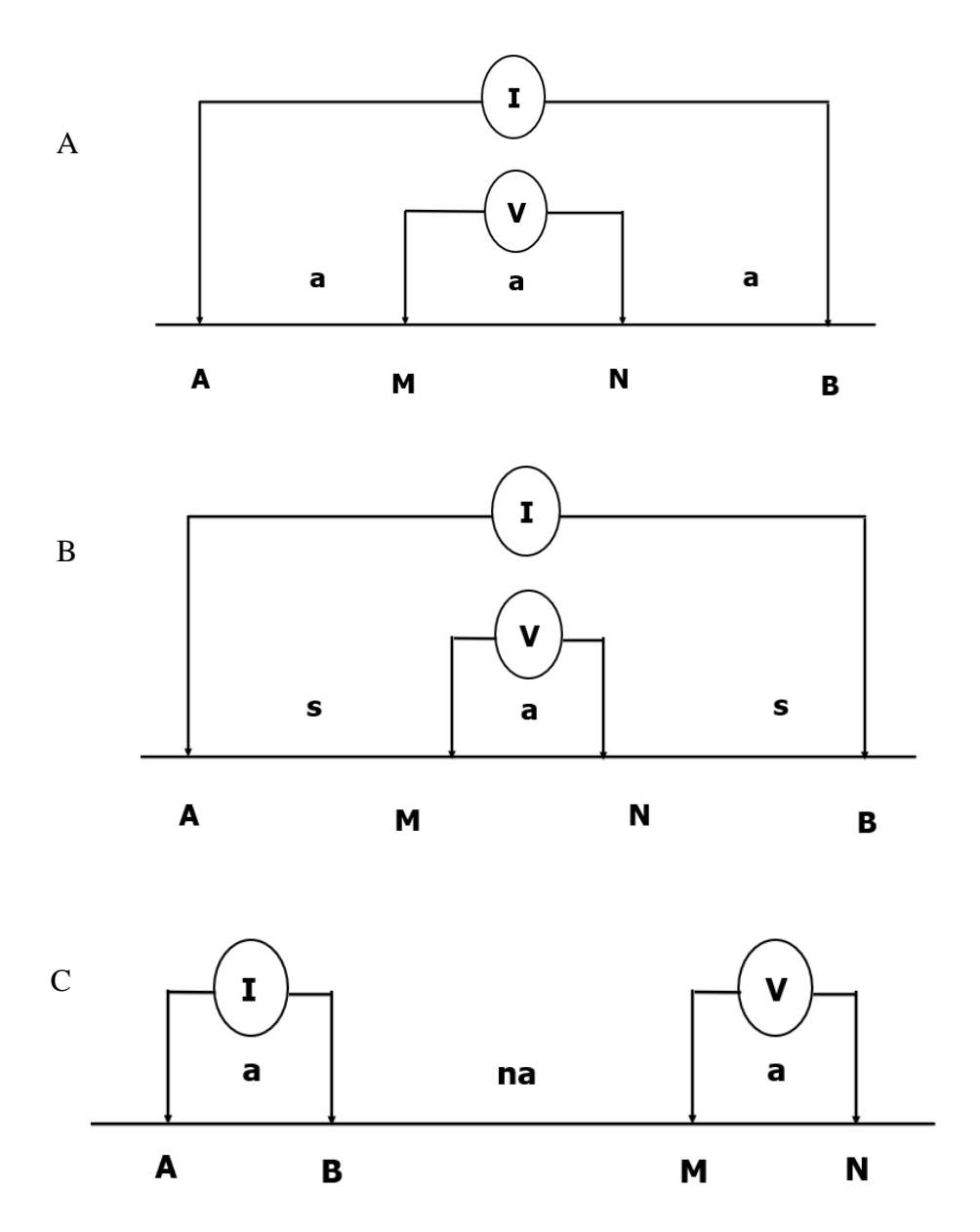


Figure 2.7: Arrangement of electrodes in the a) Wenner electrode array, b) symmetrical Schlumberger electrode array and c) Dipole-Dipole electrode array (modified after Loke, 2011).

Table 2.3: Various electrode arrays, their advantages, limitations, and suitable applications. W-S is the Wenner-Schlumberger array (modified from (Bernard et al., 2006)).

Criteria	Dipole-Dipole (D-D)	W-S	Pole - Pole
Resolution	best	regular	weak
Depth	weak	regular	best
Field set-up	regular	regular	weak
Amplitude	weak	regular	best
Natural noise	regular	regular	weak
Coupling noise	best	regular	weak
Estimated DOI	0.2 x L	0.2 x L	0.9 x L

2.2.2.7. Electrical Resistivity Tomography Studies for Investigating Lineaments

Mondal et al. (2008), delineated concealed lineaments using electrical resistivity imaging in a granitic terrain. To examine potential borehole sites and concealed lineaments, ERT using the Wenner–Schlumberger and Dipole-Dipole configurations was carried out with a maximum of 48 electrodes and 10 m electrode spacing. The results from the electrical resistivity survey showed changes in bedrock topography, the precise location of concealed fractures, and the thickness and nature of the overburden. The imaged concealed fractures allow large-scale migration of groundwater in hard rock areas and can be used as potential sites for drilling new boreholes for water supply. The usefulness of the ERT technique to study lineaments in metamorphic terrains and investigate the geophysical signatures of fracture traces in karst terrains was also reported by (Acharya et al. 2012, (Carruthers et al., 1991), (Chandra et al., 2006), and (Moore & Stewart,

1983), among others. These previous works showed that electrical resistivity data improved the characterization of subsurface features in karst terrains. Fracture traces or lineaments were detected on aerial photographs but were traced more precisely by resistivity surveys where they showed up as elongated zones of low resistivity.

2.2.2.8. Resolution Limitations of Electrical Resistivity Tomography Method

The Electrical Resistivity Tomography technique has some limiting factors that affect the resolution of detail and accuracy with which it can interpret subsurface characteristics. The resolution of a resistivity profile is dependent upon the electrode spacing and resistivity contrast between geologic materials. While the purpose of a survey may be to target deeper structures, exploring deeper layers requires increasing the current and potential electrode spacing. As the distance between the current and potential electrodes increase, the sensitivity of the ERT method decreases. This reduction in sensitivity makes it difficult to accurately interpret small-scale features at depth (Kearey et al., 2002).

Another parameter that affects the resolution of the ERT method is the contrast in resistivity between subsurface geologic materials (Muchaidze, 2008). Geologically different features such as intact bedrock and air-filled voids may have similar high resistivity values. As a result of this, provided an air-filled void is embedded in an intact bedrock, it will be difficult to detect the difference between these two features on a resistivity profile because of the low resistivity contrast. Synthetic resistivity models are used for the visual estimation of the size of detectable objects at different depths as a way to address such challenges and enhance the reliability of ERT interpretations. Such ambiguous subsurface conditions should be further investigated using complementary geophysical methods. ERT profiles should always be

interpreted with caution, keeping in mind the limitations of the method (Balasco et al., 2022; Cardarelli & De Donno, 2019; Daily et al., 2004).

CHAPTER 3

METHODOLOGY

In karst terrains, integrated studies are necessary to map subsurface fracture characteristics. In this project, borehole geophysical logging and surface geophysics (ERT) data were combined to investigate the lineaments mapped on the surface, their potential extent within the subsurface, and whether they are surface manifestations of underground fractures. This section details the methods employed in the research.

3.1. Borehole Geophysical Logging

Borehole geophysical logging, or well logging, was used as a preliminary site assessment and characterization technique in this study. Twenty-eight well logs from the United States Geological Survey (USGS) and one newly acquired well log from the Georgia Flow Incentive Trust (GA-FIT) project were analyzed to select suitable sites for the ERT survey and aid in the interpretation of the ERT field results. The USGS well logs used in this study were downloaded from the USGS GeoLog Locator database (www.usgs.gov/tools/geolog-locator, accessed: July 1, 2024). These logs were acquired in the early 1990s and consisted of the following logs, the gamma ray, short-normal and long-normal resistivity, fluid temperature, acoustic velocity, and caliper logs. All the 29 well logs analyzed in this study consisted of gamma ray logs. The gamma ray logging tool measures the intensity of natural radiations emanating from the penetrated formations within the borehole. These radiations result from common naturally occurring radioactive elements such as potassium, thorium, and uranium (Keys, 2017). This log was used to delineate lithology in the study area, with sands and limestones showing low gamma ray readings and clays showing

high gamma ray readings as shown in figure 3.1. The downloaded files from the USGS GeoLog Locator were converted to the LAS format and digitized using the WellCAD software (Advanced Logic Technology). WellCAD is a computer-based composite log package, that combines integrated data processing tools and graphic editing mechanisms for well log management, analysis, and presentation. The converted files were read into the WellCAD software and depth intervals were examined to determine if they were correctly imported. These files were saved as WCL files for log analysis and interpretation.

When the gamma ray log was difficult to interpret, the volume of shale (V_{sh}) module in WellCAD using the gamma ray index function was used to enhance boundary contrast and coherency for improved picks of lithology and formation tops. The gamma ray index function is a linear function that estimates the volume of shale based on the data measured by the gamma ray probe (sensor). The gamma ray index (I_{GR}) is calculated using this equation;

$$I_{GR} = V_{sh} = \frac{GR - GR_{\min}}{GR_{\max} - GR_{\min}}$$
 (21)

where GR denotes the gamma ray reading at a given depth point, GR_{min} and GR_{max} are the gamma ray values of the clean sand formation and clay respectively (Asquith et al., 2004).

Hydrostratigraphic units were inferred from these lithology interpretations and a template was created to be applied to the other well logs. The top and bottom of the Upper Floridan Aquifer (UFA) were picked based on the start and end of the Ocala limestone formation as generally, the UFA was made up of relatively blocky lower gamma signatures. Lithology, surfaces, and volumes of the various hydrostratigraphic units were created in Excel and imported as lithology and marker logs respectively in WellCAD.

All the interpreted well logs were grouped into three tracks, the gamma ray, lithology, and hydrostratigraphic unit tracks, and cross-sections were created using the multi-well module in WellCAD. The multi-well module is a simple and easy-to-use tool for displaying and correlating multiple wells. It has a zoomable map that acts as the graphical management interface handling imported well locations, well status, and profile orientations. This module allowed the individual well logs to be selected in the map window and viewed as a cross-sectional window.

Global Positioning System (GPS) coordinates of the interpreted logs were imported into the multi-well module interface and transect lines were selected for the well-to-well correlation of the hydrostratigraphic units. The lithological and hydrostratigraphic units were assigned different colors to aid in visualizations of the correlations. Table 3.1 provides a list of the wells, their GPS coordinates, total depths logged, and thickness of the overburden. One northwest-southeast cross-section was created across the well points to characterize the hydrostratigraphic units in the study area and select sites with thinner overburden for the ERT survey.

The ERT equipment available could only probe to a depth of approximately 40 m when the maximum 3 m spacing between the electrode takeouts is used. With less materials in the overburden for current propagation, the ERT technique can better resolve geological features, such as fractures at greater depths within the Ocala limestone. Lithology delineated by interpreting the gamma-ray responses was also used to simulate the synthetic ERT responses.

3.2. Forward Modeling

This study employed forward modeling as a predictive tool to simulate ERT geophysical responses and characterize the subsurface properties in Dougherty County, southwest Georgia.

Though the main interest in ERT data analysis is in the inversion of resistivity field data, the forward modeling was useful, particularly in the planning stage of the ERT survey. Also, the forward modeling subroutine is included in the inversion program because it is essential to compute the theoretical apparent resistivity values for the model generated by the inversion routine to determine whether they match the observed or measured values (Cardarelli & Fischanger, 2006; Mishra & Naskar, 2024). Before the ERT field survey was conducted, there was a need to simulate the resistivity distribution in the study area. Forward modeling and inversion were used extensively to quantitatively integrate geological and geophysical data. This provided a direct means for testing and validating geological hypotheses. Before carrying out the field survey, some information about topography and the shape and size of expected targets was known from the desk study conducted. Expected ERT responses were then simulated with different scenarios of electrode arrays using the Res2Dmod software (Geotomo Software Malaysia). A 2D forward modeling code for the ERT response simulation was written in Microsoft Excel based on the survey parameters in Table 3.2, and the results of the code were computed into the Res2Dmod software.

Two types of forward model computational methods are used to calculate the apparent resistivity values of the synthetic models: the finite element method and the finite difference method. In this study, various synthetic simulations were created with varying fracture widths and depths of burial using the finite difference computational method. The finite difference method differs from the finite element method in such a way that it determines the potentials at the nodes using simple regular shapes and boundaries such as a rectangular mesh, in the calculation of the potential distribution (Dey & Morrison, 1979). These models were generated for both the dipole-dipole and Wenner electrode configurations to determine their imaging capabilities using 56 electrodes with a unit electrode spacing of 3 m. The layers in the model were defined as a 2D

subsurface profile, with average thicknesses from the well log analysis and boundary conditions set to simulate lateral homogeneity and variable resistive layers.

A preliminary analysis of well logs in Dougherty County revealed that the study area is primarily composed of clays and sands in the overburden. Beneath that, the Ocala limestone formed the main lithological component of the Upper Floridan aquifer. Underlying the Upper Floridan aquifer is the Lisbon confining unit, which consists of alternating layers of sands, clays, silts, and limestone. Forward models were built comprising these three distinct layers, and typical resistivity values were assigned to these geologic materials for the forward modeling process. The overburden, Ocala limestone, and the Lisbon confining unit were assigned resistivity values of 50, 200, and 100 Ω -m, respectively. The overburden was assigned a value of 50 Ω -m because it was predominantly made up of clays and sands, which have low resistivity values when saturated. The Ocala limestone was assigned a value of 200 Ω -m because a previous study in the study area showed that this limestone had resistivity readings between 150 and 250 Ω -m. An average value was then assigned to generate the synthetic models. Fracture widths of 1 m, 2 m, 3 m, and 4 m were then constructed within the synthetic model to simulate ERT field responses. These fracture widths were selected because the Res2DMod software allows a minimum spacing of 1 m between the rectangular meshes. In this synthetic model, it was then assumed that the wider the fracture, the more solution-widened it is.

To simulate field conditions, the calculated apparent resistivity results from the forward modeling routine were contaminated with 5% Gaussian noise (Press et al., 1986; Dahlin & Zhou, 2004) before they were saved in Res2DInv format. The apparent resistivity data were then inverted using both the robust and smoothness-constrained least squares inversion computational methods in the Res2Dinv software to get ERT-simulated field responses.

A comprehensive comparison of the responses from the different simulations for the 2D resistivity imaging was made and the most suitable array was selected for the ERT fieldwork. The Anomaly Effect (AE), introduced by (Militzer et al., 1979), was applied to assess the effectiveness of the resistivity measurements for the electrode arrays used. For an effective survey, a high AE is essential as it must exceed the background noise. As a result, in this study, the anomaly effects of the different electrode arrays were evaluated based on models of similar parameters to identify the array with superior resolution and sensitivity. The 2D apparent resistivity values were analyzed to calculate the anomaly effects for the synthetic models. The mean absolute anomaly effect for a specific array or configuration was determined using the equation below.

$$AE = \frac{\rho_{\text{max}} - \rho_{\text{min}}}{\rho_{\text{av}}} \tag{22}$$

where ρ_{max} , ρ_{min} , and ρ_{av} are maximum, minimum, and average apparent resistivities respectively, observed for each electrode array.

According to Dahlin and Zhou (2004), arrays with high anomaly effects produce inversion images with enhanced resolution and greater sensitivity to the model though the resistivity contrast and the overall level of background noise influence these effects. These simulations helped in avoiding the use of an array that was unsuitable for the detection of the structures of interest. This forward modeling step also enabled the selection of optimal conditions, such as spacing between adjacent electrodes or maximum electrode separation needed. One caveat about the forward modeling routine was that it assumed isotropic conditions that may not fully reflect the heterogeneities within the subsurface. Also, there were uncertainties in the input parameters as vertical offsets caused by topographic variations may impact the reliability of the simulated results.

3.3. Electrical Resistivity Tomography Survey

The Electrical Resistivity Tomography (ERT) technique was selected as the primary surface geophysical method in this investigation because of its portable, economical, and practical applications in karst terrains. Before the main field investigation in Dougherty County, southwest Georgia, a preliminary survey was conducted at Whitehall, Athens in July 2024 to calibrate the equipment for the main field site investigation and to be familiar with the data processing technique. The main fieldwork was conducted between September and October 2024 to image subsurface fracture characteristics within the study region.

3.4. ERT Survey Design and Data Acquisition

3.4.1. Survey Design

Electrical Resistivity Tomography (ERT) data were collected along seven traverse lines in Dougherty County, southwest Georgia. The first two surveys, Profile Lines A and B, were conducted in September 2024 at the Angus Graham Farm along west-east oriented traverse lines. Subsequently, two additional surveys, Profile Lines C and D, were carried out at the Albany Nursery and the Chickasawhatchee Wildlife Management Areas, respectively, following north-south oriented traverse lines.

In October 2024, following Hurricane Helen, three more surveys were conducted: Profile Lines F and G at the Angus Graham Farm, and Profile Line E near the Georgia Flow Incentive Trust (GAFIT) well, CA 11. The survey at the known well location was conducted to aid in interpreting the ERT responses from the other survey sites. The advantage of making measurements close to existing boreholes is that their lithology logs can be used as a reference for validating and calibrating the resistivity field data. This helps accurately correlate resistivity anomalies with

specific geological formations. The locations of the ERT survey/profile lines were selected based on the georeferenced bedrock fracture map by Brook and Allison (1986). On this map, fractures were mapped based on the linear alignment of topographic features, vegetation patterns, and soil tonal changes. The profile lines were systematically named based on the order in which the surveys were conducted, and the midpoints of each survey line are shown in Figure 3.2.

3.4.2. Data Acquisition

ERT data were collected using the Advanced Geophysical Incorporation (AGI) Supersting R8 resistivity meter and its accessories (Figure 3.3). The accessories include a hammer, stainless steel electrodes, passive land cables, battery, jumper cable, switch box, and measuring tapes. A total of six passive land cables were used for this survey. Two of them accommodated 14 electrodes each and the other four accommodated 7 electrodes each. The Supersting resistivity meter used for the surveys was an 8-channel instrument that took eight readings for each current injection. The system had eight receivers, as a result for each current injection, the potential difference between nine electrodes was measured simultaneously, thus speeding up the measurement process. Approximately 56 minutes was used to take electrical resistivity readings at each survey site excluding the survey setup.

The ERT data was collected using the dipole-dipole array (Figure 3.4) with the 56 electrodes spaced 3 m apart and the total length of each of the survey lines was 165 m. The dipole-dipole array was used for this investigation because it is very sensitive to horizontal changes in resistivity making it easier to pick out vertical anomalies or contrasts within the subsurface (Okpoli, 2013; Rucker & Glaser, 2015; Swarzenski et al., 2016). This makes it suitable for mapping vertical or sub-vertical structures such as fractures.

A 2D command file was created using the AGI Supersting Administrator software and uploaded into the AGI Supersting resistivity meter before the survey to configure the survey parameters. The file defined the dipole-dipole configuration used for the survey, the electrode spacing, the maximum expansion factor 'n', the number of electrodes, and time estimates. The setup ensured that the resistivity measurements adhered to the designed survey plan. The parameters used in creating the command file are presented in Table 3.3.

Before each survey, several things were noted such as the time, location, and the GPS coordinates of the survey start and endpoints. Environmental factors such as weather conditions and potential sources of electrical noise (nearby power lines) were also noted as they could influence the data quality. Four people were present at each survey site to make the data collection effective and efficient. After taking the field notes, tape measures were laid on the ground in a straight line to measure the desired length of the survey line, and electrodes were placed at every 3 m interval. After positioning the electrodes at every 3 m interval, they were hammered into the ground to ensure good electrical contact between them and the subsurface materials to enhance current injection. If the ground was dry or resistive, additional measures such as applying water or adding an extra electrode were used to further enhance the contact. The electrodes were then attached to the passive land cables at each takeout point with the help of the stainless-steel springs. The survey was set up in such a way that the Supersting resistivity meter remained at the center of the survey to ensure a balanced distribution of current injection and potential measurements across the entire survey line.

Once the setup was complete, the resistivity meter powered by a battery was programmed with the survey parameters, including the array type, electrode spacing, start and end positions of the electrodes, amount of current to inject, and the duration of the current injection cycle. A pre-

survey test called the electrode contact test was run to check for any errors in the setup, such as poor electrode contact or broken cables. When there was any error in the setup, the resistivity meter indicated an HVOVL error code, and any detected issues were resolved to ensure accurate data collection. After the electrode contact test, the survey started with the resistivity meter automatically injecting currents into the ground through specific electrode pairs while measuring the resulting potential difference generated at the other electrode pairs. These measurements were recorded for all combinations of electrodes in the dipole-dipole configuration. During the survey, elevation data was taken at every electrode position using a hand level and a staff. The elevation data were used to correct the inverted field data for variations in surface elevation along the survey line.

At the end of the survey, each survey was saved as a .stg file and the data were downloaded onto a field laptop for initial quality control checks. This involved reviewing the apparent resistivity pseudosections to identify any inconsistencies or anomalies in the data that might indicate setup issues or noise interference. All equipment were then carefully disassembled, and the site was inspected to ensure it was left as it was found. The survey process was repeated for each of the seven survey lines, ensuring consistent methodologies to allow accurate comparisons during data analysis.

3.4.3. Inverse Modeling

The computer program, Res2DInv software (Geotomo Software, Malaysia, copyright 1995-2006) was used to invert the apparent resistivity field data. Res2DInv is a robust 2D inversion software that offers an intuitive workflow from data import to inversion and visualization, with extensive options for advanced users to customize inversion parameters. Given the wide range of data sets collected over various geological settings, no single inversion method will give the

optimum results in all cases. The Res2DInv program therefore has several settings that the user can change to obtain results that are closer to the known geology (Loke, 2011).

The data derived from the ERT field survey is resistance. To convert resistance to resistivity, a geometric factor depending on the electrode configuration used and treating the earth as a homogenous hemisphere is applied to the field resistance data. As a result, the resistivity data obtained from this conversion is the apparent resistivity. To get the true resistivity distribution of the subsurface, the apparent resistivity data is then inverted using an inversion software.

The main aim of the inversion process is to find a model that shows responses similar to those observed with the actual measure values (Loke, 2001). The Res2DInv software generates the true resistivity model by dividing the subsurface into rectangular pixels (Figure 3.5), with each pixel assigned a resistivity value representative of its constrained materials and the pixel dimensions influenced by the electrode spacing (Anderson et al., 2006). Horizontally, the pixel dimensions correspond to the distance between adjacent electrodes while the vertical dimension of the pixels is about 20% of the electrode spacing near surface and gradually increases to 100% at greater depths. The resolution of the resistivity models is therefore determined by the pixel size, so the resolution decreases as the depth of investigation increases (Muchaidze, 2008).

To invert the apparent field resistivity data in the Res2DInv software, the resistivity data sets were inspected for bad data points such as negative readings and unreasonably high or low resistivity values. These bad data points can result from several reasons, such as poor electrode ground contact, cable breaks, forgetting to attach the stainless-steel spring to the electrode, and connecting the passive land cables in the wrong direction. In this thesis, these bad data points were removed using the filter option in Microsoft Excel. After the bad data points were exterminated, inversion parameters in Table 3.4 were applied to the data to convert the measured resistivity data

sets into inverted resistivity models (ERT resistivity profiles) which reflect the lateral and vertical resistivity distribution within the subsurface. The inversion routine was modified with techniques such as smoothing the resistivity model or applying robust inversion. In the smoothing approach, constraints are applied directly to the resistivity values, resulting in models with gradual variations in resistivity while the robust inversion minimizes the sum of absolute discrepancies, producing models with uniform resistivity and sharp boundaries. For this study, the mathematical expression used in estimating the resistivity of each of the cells was the robust constraint method (Loke et al., 2003). This inversion method seeks to develop an idealized model of the subsurface resistivity distribution that closely matches the measured pseudosection. The difference between the calculated and observed resistivity data can be quantified using either the absolute or root mean square (RMS) error. Both errors are calculated using the Gauss-Newton method. The RMS error is calculated using the L2 norm while the absolute error is calculated using the L1 norm and is used when high resistivity contrasts are expected. For this study, the blocky model constraint (L1) was used as fractures are expected to yield sharp contrast in resistivity with their surrounding media (Van Riet et al., 2022).

The acquired ERT profiles were modeled using these methods and the resulting inverted sections were selected based on how well they represented observed features in the inverse models. Topography data was incorporated into the inversion process for all the ERT profiles. Each inverted resistivity section has a scale from low resistivity (blue) to high resistivity (violet) measured in ohm-m. The final inverted resistivity sections were exported as bitmap image files which were then edited for presentation clarity by removing unwanted sections and adding additional information to the outputs.

 Table 3.1: List of wells, GPS coordinates, total depths logged, and overburden thickness.

Well ID	Latitude	Longitude	Total logged depth (ft)	Overburden Thickness (ft)
11L116	31.57795075	-84.3037995	145	30
12K123	31.49458	-84.22172	240	45
12K136	31.446	-84.2104444	205	70
12K144	31.49628605	-84.221575	200	50
12K148	31.4947222	-84.2197222	200	35
12K154	31.49406386	-84.2243528	200	50
12L281	31.5865629	-84.1476853	130	20
12L295	31.5371186	-84.222131	50	35
12L324	31.54277778	-84.23	140	40
12L325	31.5451739	-84.23435349	380	40
12L326	31.53692778	-84.23256389	110	25
13L180	31.5465649	-84.0137936	320	50
13L181	31.56100833	-84.0935174	230	100
13L183	31.5573978	-84.0396274	220	65
13L184	31.5551757	-84.0310161	190	50
13L185	31.55489787	-84.03823849	170	40
13L186	31.55489793	-84.0318495	190	50
13L188	31.55795334	-84.0412941	190	70
13L189	31.55211984	-84.0687947	125	110
13L191	31.54684213	-84.0704614	130	110
13L192	31.55100879	-84.0646279	130	100
13L209	31.55073099	-84.0668502	110	50
13L212	31.55850875	-84.0557388	270	200
13L213	31.54406418	-84.0929618	250	125
13L215	31.55461966	-84.082406	250	140
13L219	31.55128666	-84.0540721	300	190
13L221	31.5437869	-84.0429608	320	237
13L225	31.5476758	-84.032405	320	225
CA11	31.5272503	-84.3688293	550	30

Table 3.2: Parameters used in creating the various synthetic models.

ID	Parameter	Unit	
1	Number of electrodes	7	
2	Array types	W, D-D	
3	Number of 'a' spacing	18	
4	Number of 'n' values	8	
5	Electrode spacing	1 - 4 m	
6	Resistivity of overburden	50 Ω-m	
7	Resistivity of Ocala Limestone	200 Ω-m	
8	Resistivity of Lisbon Formation	100 Ω-m	
9	Resistivity of fracture	10 and $100~\Omega\text{-m}$	
10	Computational method	Finite-difference	

Table 3.3: Parameters used in creating AGI command file.

ID	Parameter	Unit
1	Type of array	D-D
2	Number of electrodes	56
3	Maximum expansion factor 'n'	8
4	Maximum dipole	6
5	Number of cycles	2
6	Measure time	1.2 s

Table 3.4: Parameters for ERT inversion process.

ID	Inversion Parameter	Unit
1	Number of iterations	7
2	Error change convergence limit	5 %
3	Data inversion constraint	Robust
4	Inversion equation	Least-squares
5	Use extended model	No

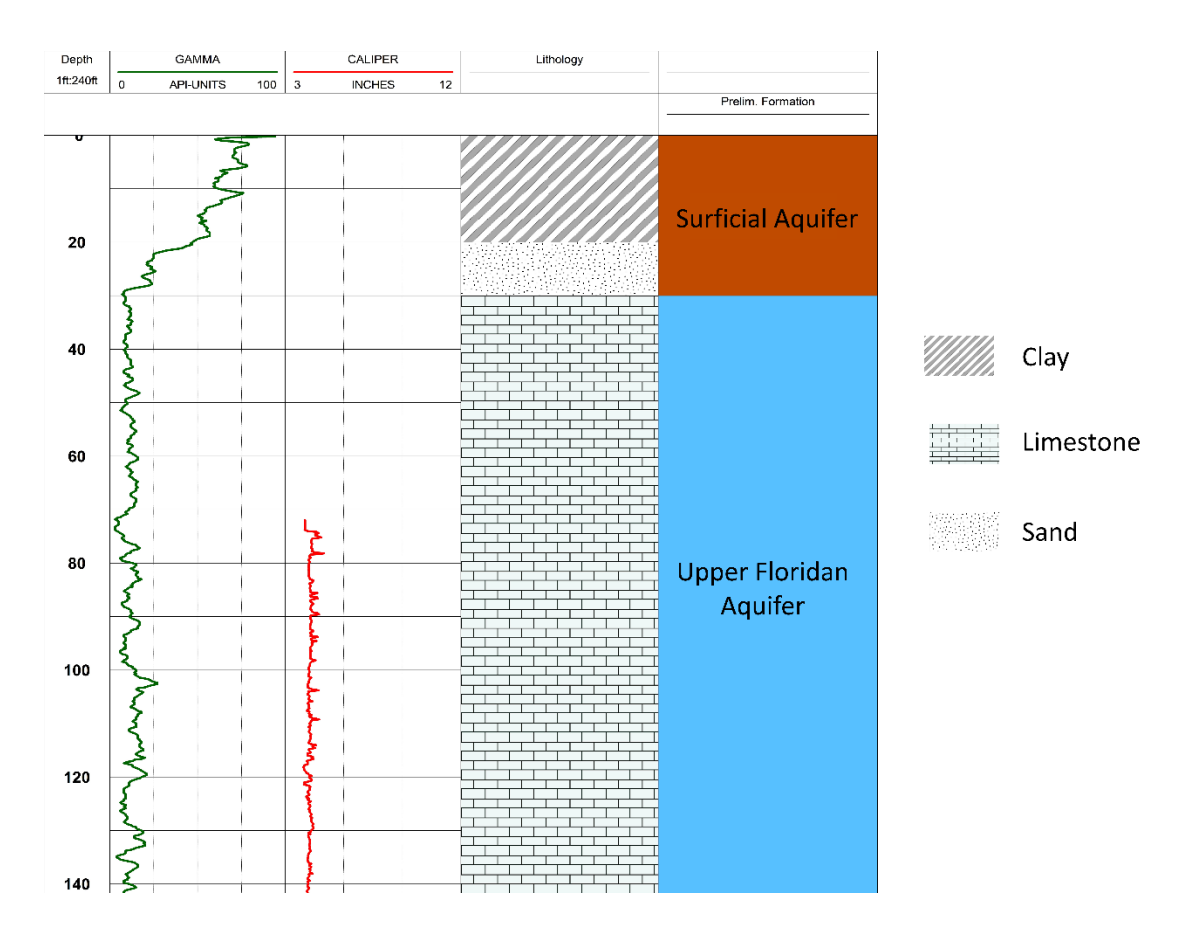


Figure 3.1: Composite log response from one of the USGS well logs (11L116). Deflections to the left on the gamma ray log in green show low readings, and to the right show high readings. Limestones show lower readings than sands because of the lower amount of radioactive elements.

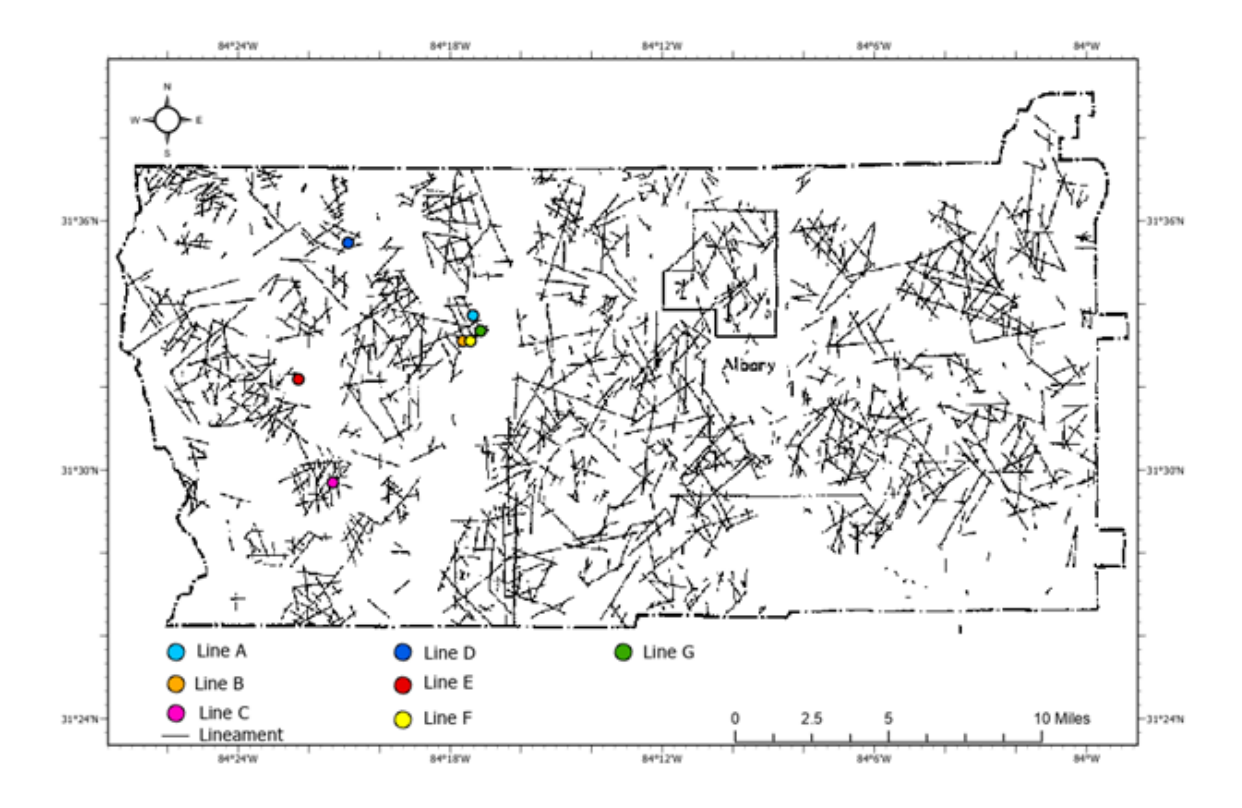


Figure 3.2: Map showing the midpoints of the ERT survey lines.

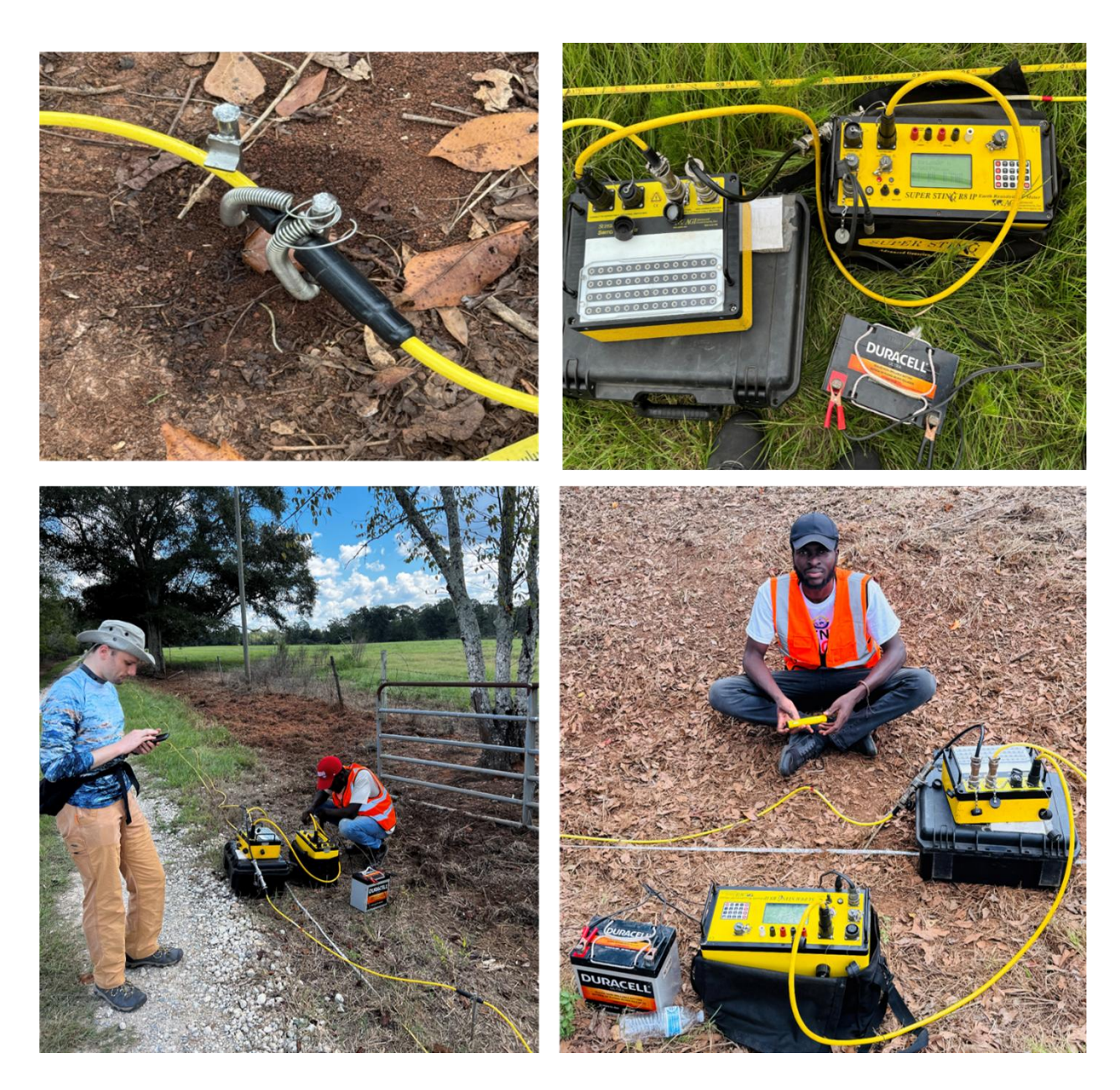


Figure 3.3: AGI Supersting R8 resistivity meter deployed in the field.

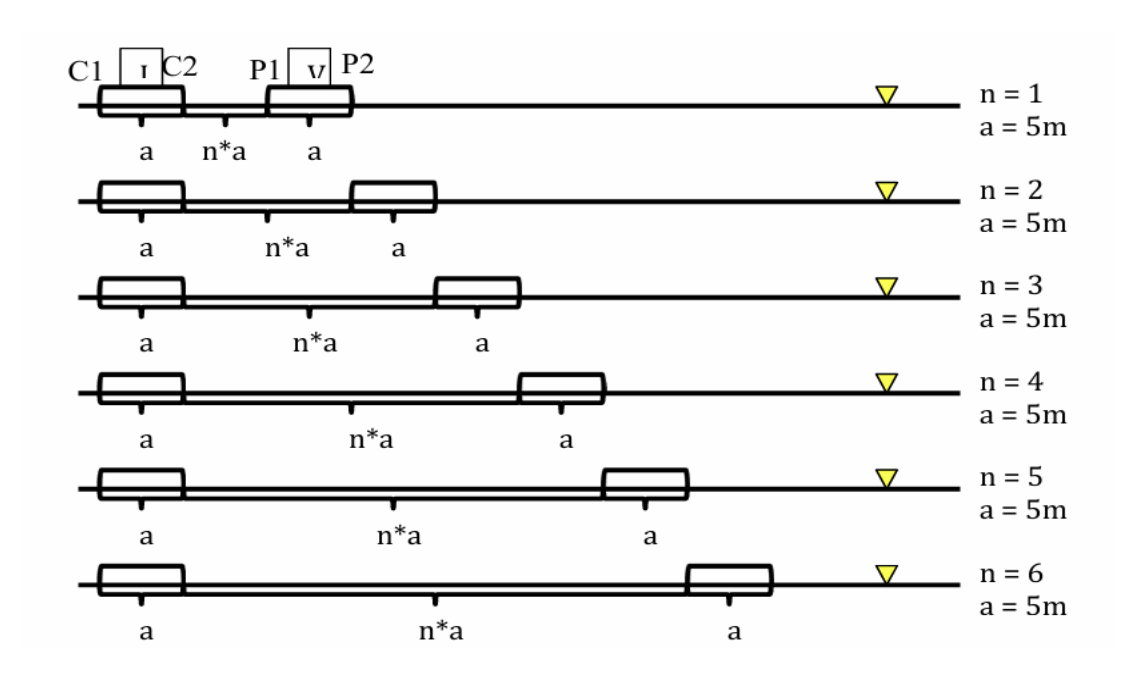


Figure 3.4: Geometry of the dipole-dipole field measurement (modified from Wylie et al., 2014). P1 and P2 are the potential electrodes, C1 and C2 are the current electrodes, and 'a' is the spacing between the electrode pairs.

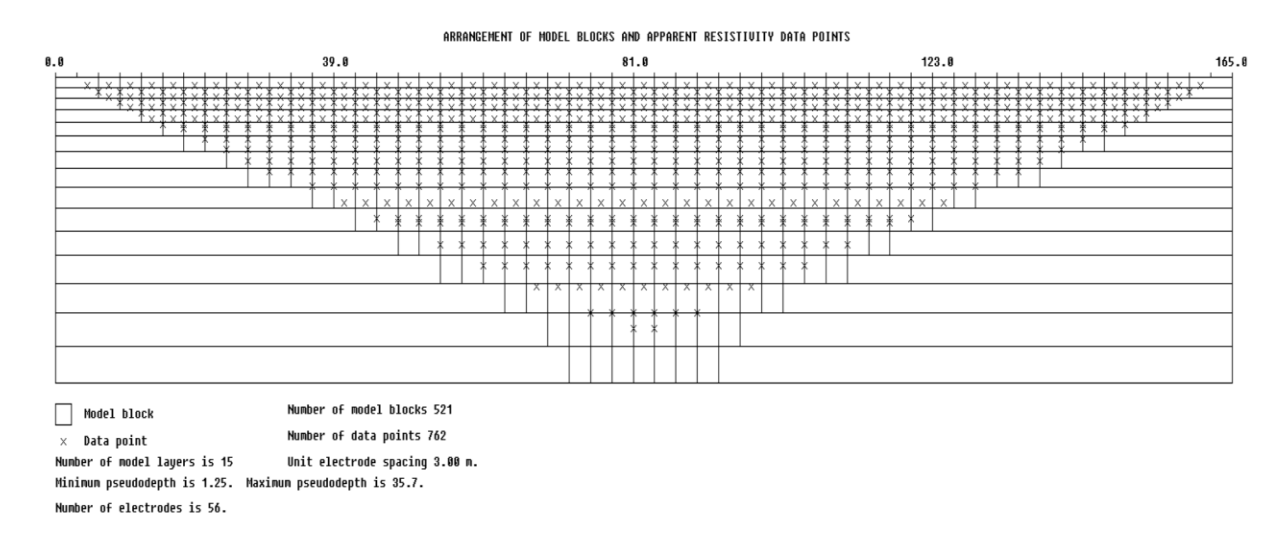


Figure 3.5: Arrangement of the rectangular blocks used in a 2-D model and the data points in the pseudosection.

CHAPTER 4

RESULTS AND DISCUSSION

This chapter presents the results and interpretations of the geophysical analyses conducted during the study. The section discusses the results from analyzing the borehole geophysical logs which provide information about lithological variations within the subsurface. It is followed by deductions from the forward modeling process for designing the ERT survey and evaluating the accuracy and reliability of the data inversion approach. This chapter also includes the results and interpretations of the ERT resistivity models. The integration of these findings provided a comprehensive understanding of subsurface fracture characteristics in Dougherty County, southwest Georgia.

4.1. Well Logs Interpretation

Twenty-nine well logs were analyzed in the study area (Figure 4.1) to refine the geology of the region and select areas with a thin overburden for the ERT field survey. Logging depths varied significantly among the 29 well logs analyzed. The deepest borehole (CA 11) was logged to 550 feet below the surface. The rest of the wells were logged to depths between 50 and 320 feet. Three main hydrostratigraphic units were interpreted from the well logs based on the gamma logs but were supplemented with drill cuttings when available. These units include the surficial aquifer made up of overburden materials, the Upper Floridan Aquifer consisting mainly of the Ocala limestone, and the Lisbon confining unit made up of sands, clays, and silts. All the wells logged penetrated the overburden as well as the Ocala limestone which was interpreted based on the low gamma ray readings of approximately less than 20 API. The top of the Upper Floridan Aquifer

was picked at the base of the overburden materials showing a significant decrease in gamma ray signature. The low gamma ray signature of the Ocala limestone made it easy to delineate the unit across the study area. 11 out of the 29 well logs analyzed penetrated the Lisbon Formation. A cross-section (Figure 4.2) generated across the study area shows that the overburden thickness varied across the wells, getting progressively thinner towards the western part of the study area. The well logs confirmed the presence of the Ocala limestone at shallow depths in the study area and sites in the western part of Dougherty County were prioritized for the ERT survey for improved resolution of subsurface features. This observation is consistent with findings from Parker and Hawman, (2012) and Brook and Allison, (1986), which confirmed that the unconsolidated overburden is thinner west of the Flint River and gets thicker towards the southeastern part of Dougherty County.

4.2. Simulating Subsurface Responses from Forward Modeling

Synthetic models were created to simulate ERT responses for different fracture orientations, spacing, and depths using both the Wenner and Dipole-Dipole electrode arrays. In this results section, two specific cases are considered for comparison:

Case 1: A three-layer subsurface model with a 4 m fracture located at the center of the survey line, extending vertically through the overburden and into the Ocala limestone.

Case 2: A three-layer subsurface model with a 4 m fracture located at the center of the survey line, confined entirely within the Ocala limestone.

These scenarios were chosen to evaluate how each electrode array (dipole-dipole and Wenner) responds to fractures at different depths within the subsurface and to assess their sensitivity and

resolution in imaging subsurface features. Included in this result section are also the synthetic models of fractures of different widths confined within the Ocala limestone. Resistivity sections for all the other synthetic models are included in the Appendix for reference.

Comparative analyses of the simulated ERT responses for dipole-dipole and Wenner arrays are presented in Figures 4.3a and 4.3b. The results revealed that the dipole-dipole array showed high sensitivity to lateral changes in resistivity, making it well-suited for detecting narrow fracture zones and other subsurface heterogeneities. The dipole-dipole array showed a greater depth of investigation in both models as compared to that of the Wenner array. Also, the Wenner array demonstrated higher sensitivity to layered subsurface features but lower resolution for vertical structures, limiting its applicability to the objectives of the study. The anomaly effect (AE) calculations quantitatively validated these observations, with the dipole-dipole array showing consistently higher AE values across all models, indicating better resolution and sensitivity in detecting the fractures. The AE values for the two case scenarios are presented in Table 4.1. The inversion of the apparent resistivity data using the robust method produced high-quality simulated field responses, with clear delineation of the interfaces between the overburden and the Ocala limestone in the dipole-dipole array. Generally, the array type affected the appearance of the inverted resistivity models.

The synthetic models in Figure 4.4 further illustrate fractures of varying widths confined within the Ocala limestone and demonstrate that the fractures can be detected by ERT within the Ocala limestone regardless of their width. These models show how well-resolved even the smaller fractures are within the Ocala limestone and suggest that ERT is a reliable method for detecting subsurface fractures within the limestone formation.

 Table 4.1: Anomaly effect calculations used in selecting the most suitable electrode array.

Case	Electrode array	Minimum apparent resistivity	Maximum apparent resistivity	Average apparent resistivity	Anomaly Effect (AE) value
1	Wenner	14.03	89.21	60.36	1.25
	Dipole-Dipole	10.34	109.88	58.02	1.72
2	Wenner	49.42	91.67	63.96	0.66
	Dipole-Dipole	5.80	108.33	49.81	2.06

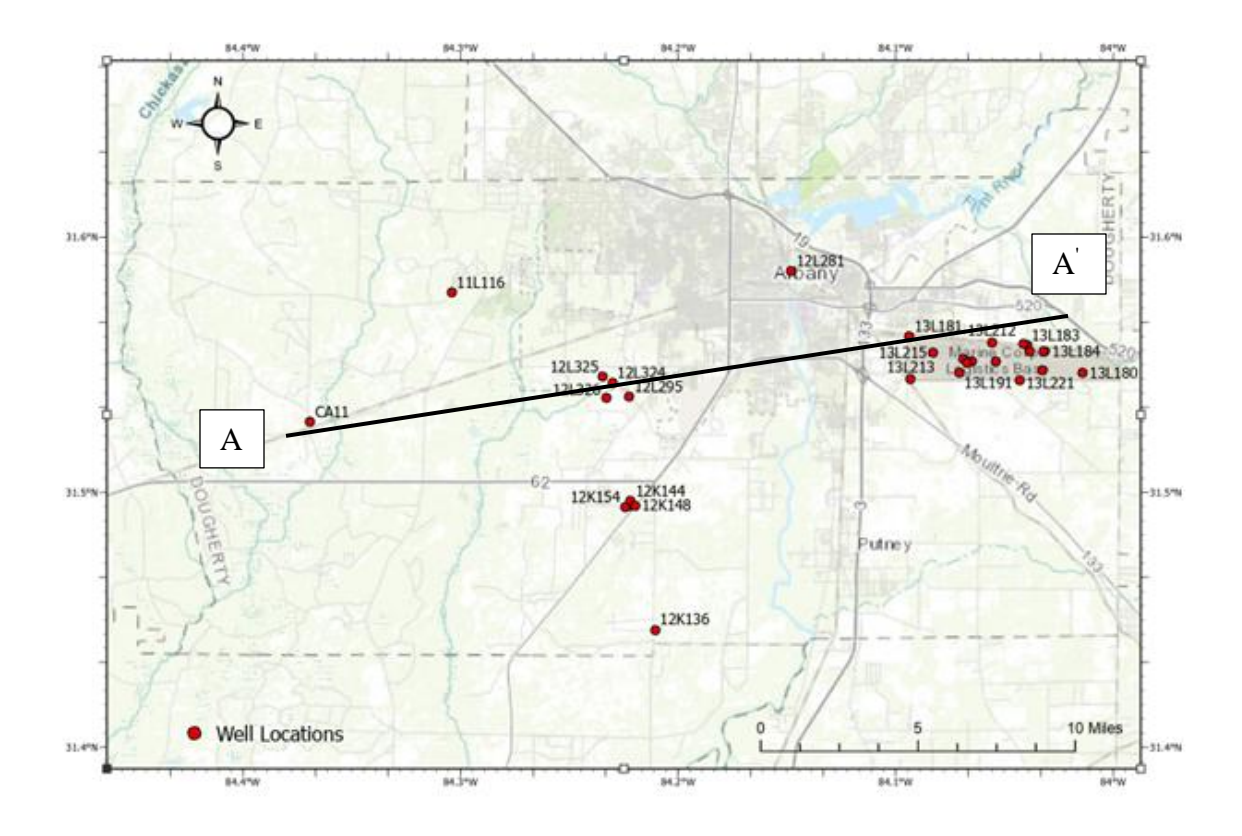


Figure 4.1: Map showing the location of the twenty-nine wells used in refining the general knowledge of the study area (All but well CA11 are USGS wells).

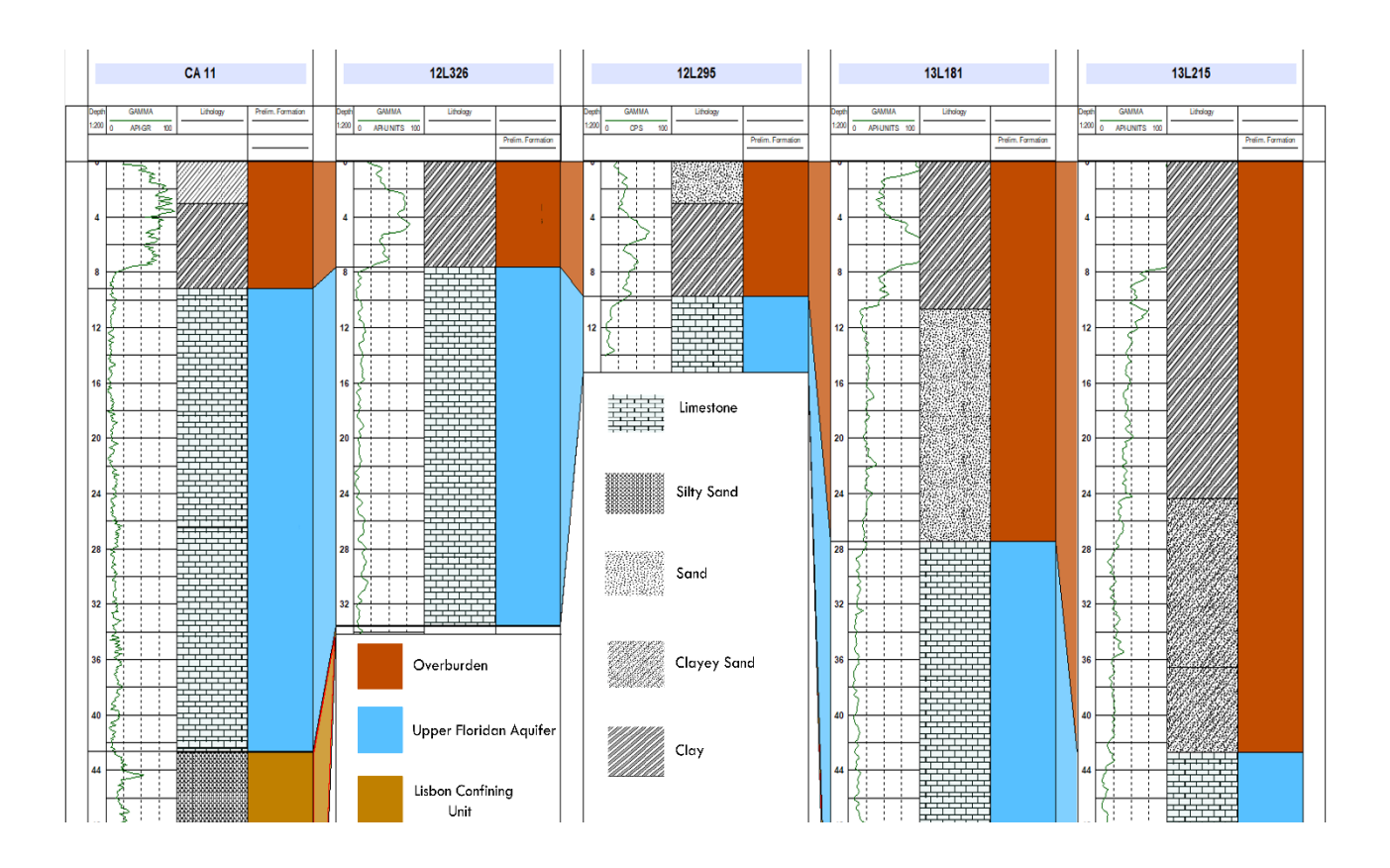


Figure 4.2: Well-to-well correlation panel of the hydrostratigraphic units across the study area from SW to NE.

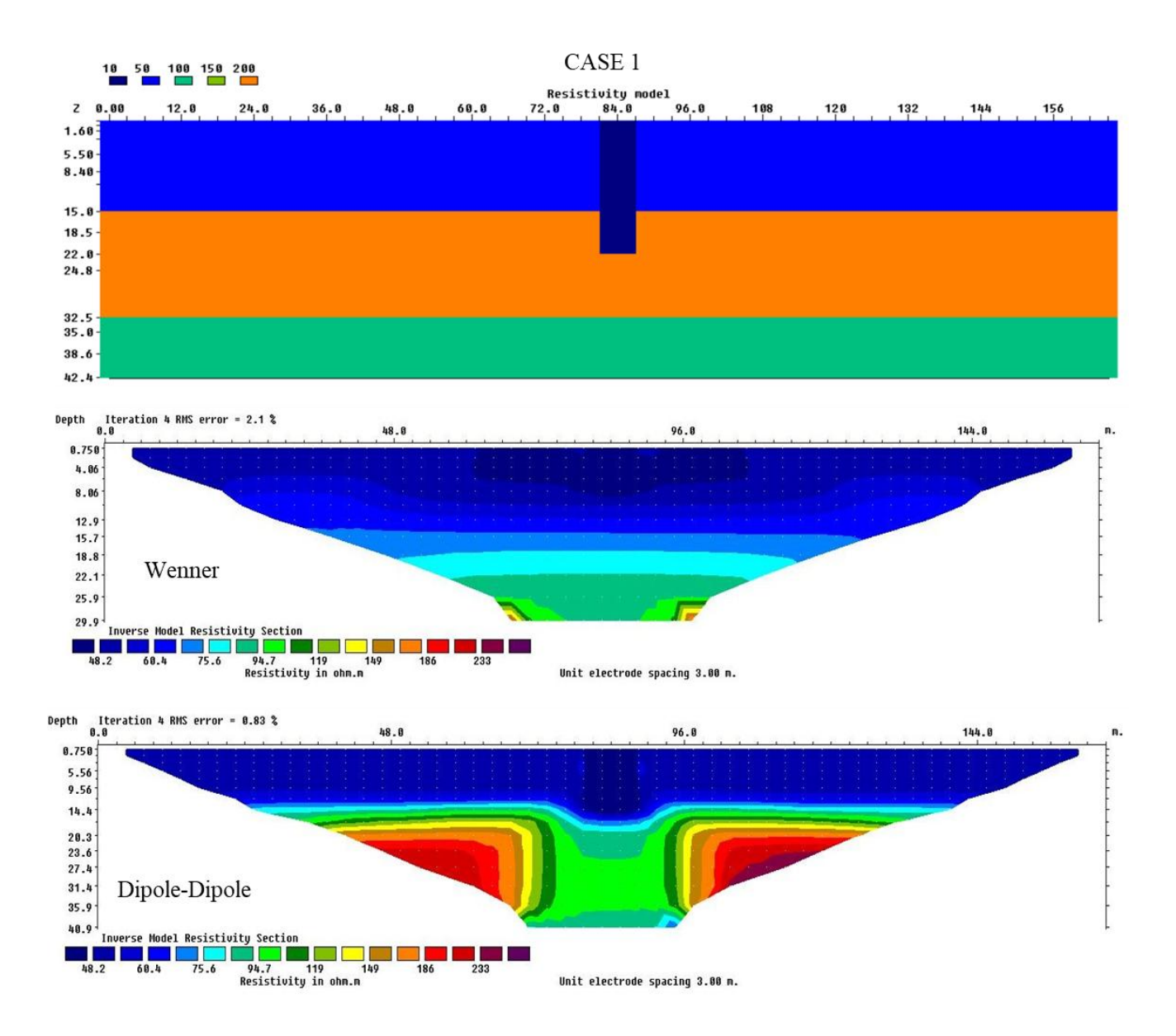


Figure 4.3a: Synthetic (top) and inverted (middle and bottom) sections of a three-layered subsurface model with a 4 m fracture located at the center of the survey line, extending vertically through the overburden and into the Ocala limestone. The middle-inverted section represents resistivity distributions using the Wenner array while the bottom section represents resistivity distributions using the Dipole-Dipole array.

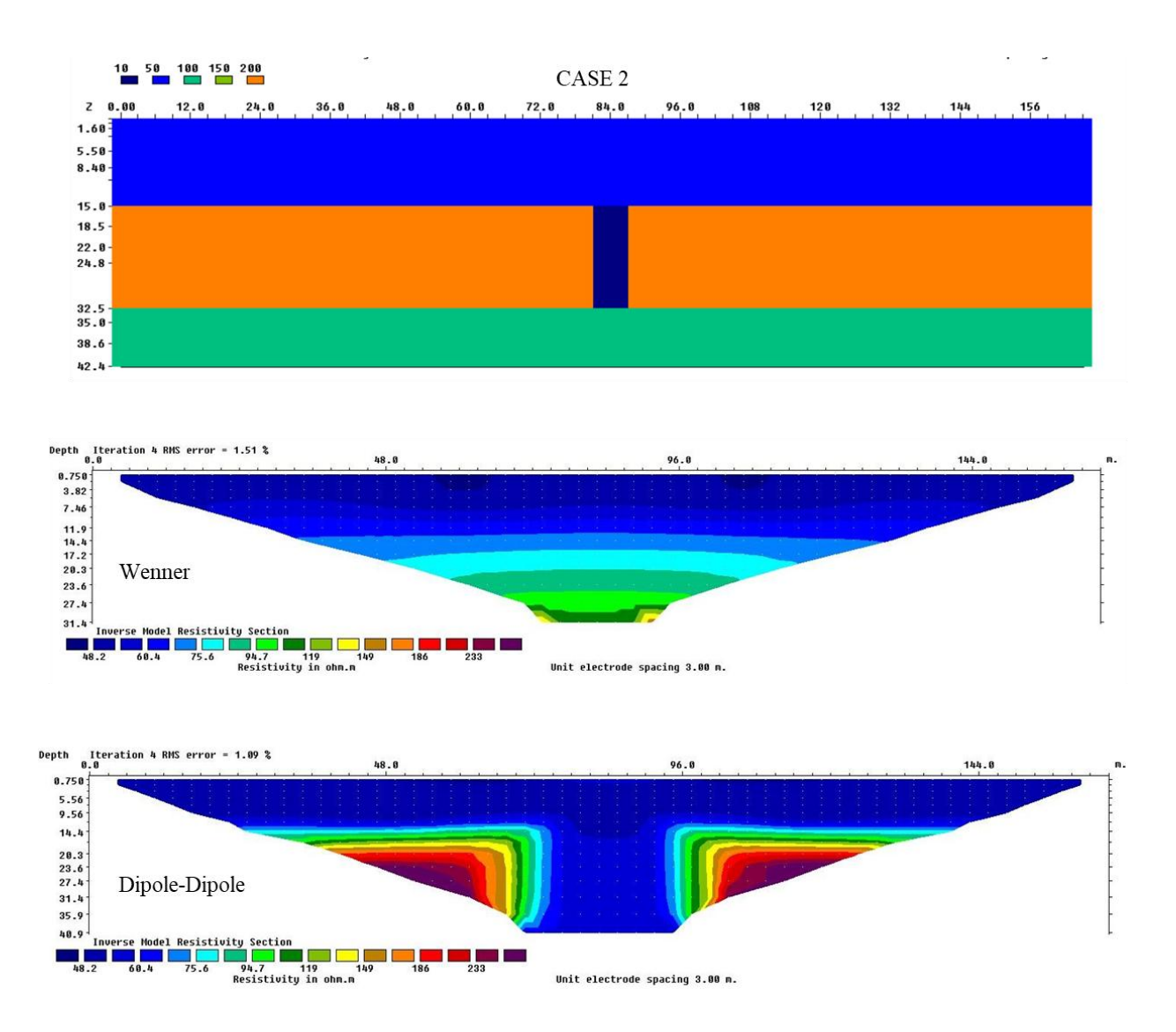


Figure 4.3b: Synthetic (top) and inverted sections (middle and bottom) of a three-layered subsurface model with a 4 m fracture located at the center of the survey line, confined entirely within the Ocala limestone. The middle-inverted section represents resistivity distributions using the Wenner array while the bottom section represents resistivity distributions using the Dipole-Dipole array.

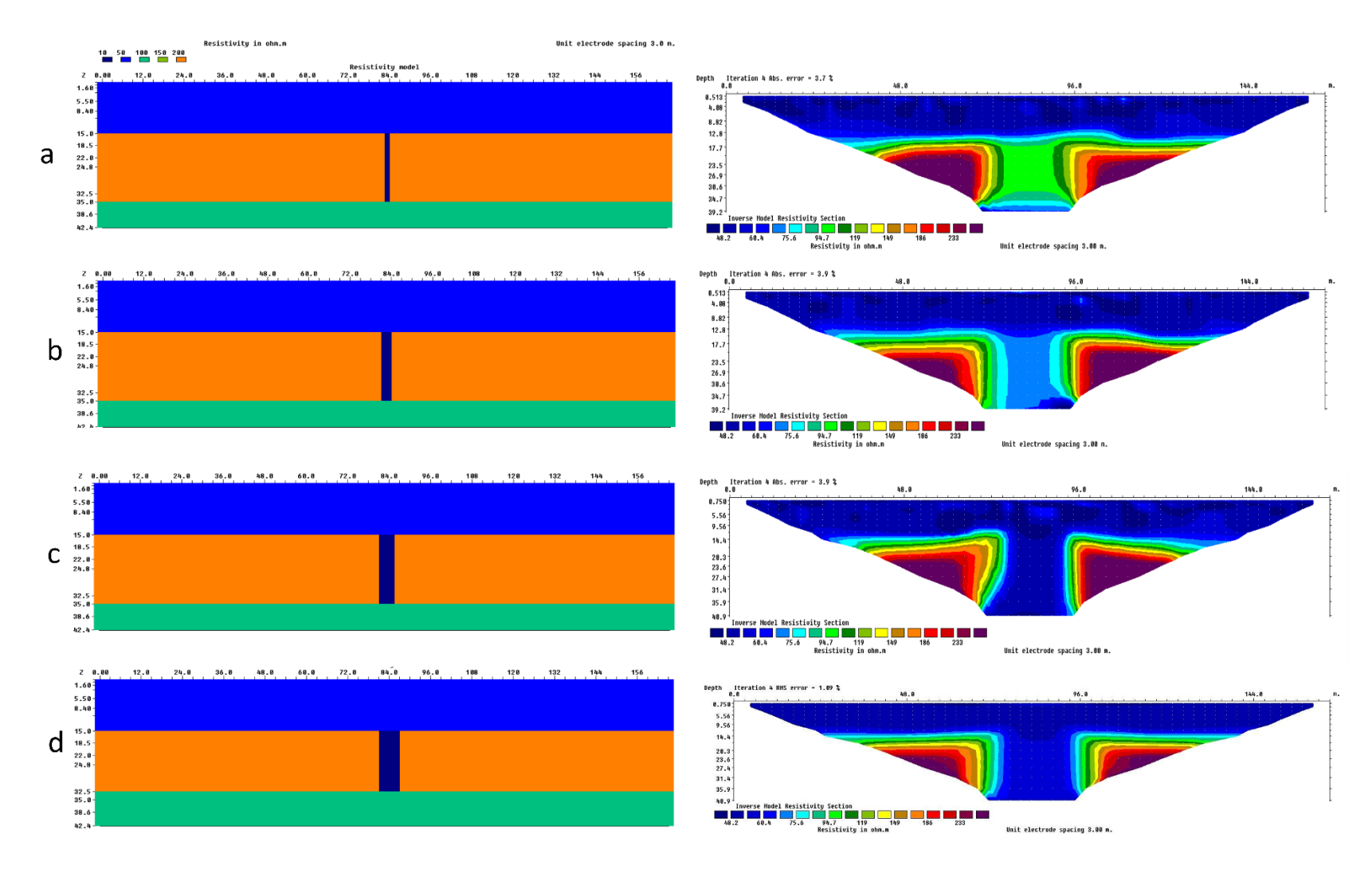


Figure 4.4: Synthetic (left) and inverted ERT sections (right) illustrating fractures of varying widths within the Ocala limestone using the dipole-dipole array: (a) 1m fracture, (b) 2m fracture, (c) 3m fracture, and (d) 4m fracture.

4.3. Resistivity Profiles and Subsurface Characterization

4.3.1. General Comments About the Model Sections

ERT surveys were carried out along eight traverse lines using the AGI Supersting R8 resistivity meter and its accessories. Apparent resistivity data results gathered from the surveys were processed to generate 2D model sections of subsurface resistivity using the RES2DINV software. To ensure consistency in the analysis of resistivity pseudo-sections across the various profile lines, each profile data was processed individually. However, the same inversion procedures were applied to all the model sections. The model sections of the surveys conducted in Dougherty County were placed on the same resistivity color scale to help with comparisons and to reduce differences and ambiguity to the barest minimum. The overburden-Ocala limestone contact is marked by black dashed lines; potential faults are delineated by full blue lines; and full black lines are used to highlight potential fracture zones within the subsurface.

During the data acquisition for ERT Line G, there was an issue with the passive land cable and steel electrode connection. Electrode positions 41, 42, and 43 failed the electrode contact test, and as a result, they were excluded from the data set. The inversion routine smeared out the effect of these electrode positions and likely used data from the next depth, which has lower resistivity, leading to a lower inversion estimate at the surface between lateral distances 126 and 129 m. The resolution, however, might not be good, as it is interpolated data.

4.3.2 Interpretations of Model Sections

One important aspect of any subsurface characterization survey is a good appreciation of geology. The geology of the area determines the characteristics of groundwater occurrence and potential geologic features within the subsurface (John E. Moore, 2005). The study area is generally underlain by a predominantly sand and clay overburden, the Ocala limestone, and the

Lisbon Formation (Fig 4.2). The interpretation of the resistivity profiles were therefore based on the knowledge of the geology of the survey area and the general resistivity of the subsurface materials. The results are discussed presently below.

4.3.3. ERT Field Results

Initial Survey: Whitehall

The inverted model section (Figure 4.5) shows the resistivity of subsurface materials ranging from 103 to more than 7900 Ωm in different color bands over a distance of 110 m and up to a depth of 27.2 m below the ground surface. The electrode configuration used in this survey was the dipole-dipole array with 56 electrodes spaced at 2 m. It is evident from the model section that, the subsurface is not horizontally layered and does not extend from one end to the other. There are lenses of low resistivity layers within the first 5 m below the ground surface which can be interpreted as water-bearing zones. There was a 1 m diameter culvert between electrode positions 32 and 34. This can be seen in the model section as the 100 Ω m low resistivity zone between 32 and 34 m because it was water-filled. Closer to the surface at the western end of the section, there is a resistive layer with resistivity values ranging between 2000 to about 8000 Ω m. This layer is interpreted as the gneiss bedrock unit. However, the layer at the eastern end is less resistive, with resistivity values from 1400 Ωm and below. This implies that the bedrock is more weathered between 55 to 110 m lateral distance. The gradual decrement of resistivity toward the eastern end indicates a higher degree of near-surface weathering of the bedrock. This is depicted by the lower resistivity readings of the zones on the eastern end of the section. Considering the layering in the section, a fault can be interpreted from the resistivity model. The resistivity model, however, does not show any vertical anomalies as evidence of a fracture across the profile line.

Line E: ERT Survey Along a Known Well Location

Profile E (Figure 4.6), spans a total length of 165 m, and the drilled well (CA 11), was in the middle of the survey line. This survey line did not intersect with any mapped lineament. The uppermost layer within this ERT section shows varying thickness and comprises materials with varying resistivity values. At the western end of the top layer, highly resistive materials (250 – $1000~\Omega m$) extend from the start of the profile to approximately 30 m lateral distance. Between 30 and 48 m lateral distance lies a zone of very low resistive values ranging from 9 to 40 Ωm . Materials with resistivity values between 74 Ωm and 550 Ωm cover the rest of the profile line. Beneath the uppermost layer, the inverted section shows both vertical and horizontal resistivity anomalies, particularly in the central segment of the profile. Intermediate to high resistive materials (74–1200 Ωm) at both ends of the section are separated by a vertical zone of significantly low resistivity values (9-40 Ωm), which extends to the bottom of the cross-section. The depth from the surface to the intermediate to high resistive material varies along the profile as it is approximately 9 m at the western end and 12 m at the eastern end of the profile line.

Lithology and Structural Interpretation

The uppermost layer, characterized by varying resistivity values, represents the overburden composed of sands and clays. Within the uppermost layer, the high resistivity zone (420-1000 Ω m) indicates dry sands or gravels, and the very low resistivity zone (9-40 Ω m) between 30 and 48 m lateral distance suggests saturated clays and/or water. The materials with resistivity values between 74 Ω m and 550 Ω m beyond 48 m lateral distance indicate a mixture of dry sands and clays. The vertical low resistivity zone (9-40 Ω m) in the central part of the section likely represents a fracture zone within the Ocala limestone potentially induced by the drilled well (CA 11). This vertical feature separates the more competent limestone units at both ends of the section.

Angus Graham Farm

Four resistivity surveys were carried out within the Angus Graham Farm. Profile lines A, B, and F were located across N-S lineaments, whereas Line G was across an E-W trending lineament. Figure 4.7 shows the orientation of the survey lines within the Angus Graham Farm site.



Figure 4.7: Orientation of ERT survey lines at the Angus Graham Farm site.

Line A

Line A (Figure 4.8), located in the northern section of the farm, covers a total length of 165 m. The uppermost layer of the profile, approximately 7 m thick, exhibits distinct resistivity

variations and extends horizontally across the entire length of the profile. Highly resistive materials are found between 72 and 165 m along the profile line with less resistive materials at the western end of the uppermost section. At the western end of the profile at approximately 48 m, a zone of low resistivity ($<145~\Omega m$) is embedded within horizontally layered high-resistive materials ($>250~\Omega m$). Beneath the uppermost layer lies a relatively low resistive layer with values ranging from 9 to 74 Ωm at a depth between 7 and 17 m. This layer is about 10 m thick and has a series of unconnected zones of low resistivity embedded within it. Below this 10 m thick layer at a depth of 17 m, a sequence of horizontally layered materials with resistivity values ranging from 74 to 280 Ωm are observed. Towards the eastern end of the profile, this sequence of horizontally layered materials becomes near vertical, suggesting structural deformation or geological process altering the layering pattern in this section.

Lithology and Structural Interpretation

The uppermost layer of resistivity ranging from $145-250~\Omega m$ corresponds to the overburden. The variation in resistivity values reflects different materials within the overburden. The high-resistive materials (>250 Ωm) in the central and eastern parts of the profile within the uppermost layer indicate well-drained sands and gravels, while the low-resistivity zone (<145 Ωm) at the western end could represent a sand-clay mixture. The middle layer of resistivity values ranging between 9 and 74 Ωm can be interpreted as the upper portion of the Ocala limestone. The low resistivity values in this layer can be attributed to a high degree of weathering as a result of fracturing or saturation from groundwater. The presence of the isolated low-resistivity zones also suggests karst features such as solution or clay-filled cavities distributed throughout the layer. The deeper layer indicates the less weathered and more competent portions of the Ocala limestone. The horizontally layered features of varying resistivities suggest differences in porosity and moisture

content. The transition from horizontally layered materials to a near-vertical orientation at the eastern end of the profile suggests possible faulting.

Line B

Profile B, located in the southern section of the farm, covers a maximum length of 165 m and was acquired before Hurricane Helen. The inverted section (Figure 4.9) shows a top layer characterized by materials of high resistivity values ranging from 220 and 1000 \Omegam. This uppermost layer, approximately 6 m thick, extends horizontally along the entire profile length with no significant changes in layer thickness. The continuity of the layer is only interrupted between 99 m and 102 m lateral distance, where there is a relatively low resistivity anomaly (75 Ω m) between two highly resistive zones. Beneath the uppermost layer lies a relatively low to intermediate resistivity layer with resistivity values ranging between 9 to 110 Ω m at a depth between 6 and 18 m. This 12 m thick layer exhibits a remarkably sharp and horizontally layered upper boundary, whereas the lower boundary follows an undulating irregular pattern in layering. Within this layer, there are a series of isolated lentiform features with distinct resistivity contrasts. Underlying the 16 m thick layer is a deeper layer with resistivity values ranging from 110 to 420 Ω m, which extends to the bottom of the inverted section. In the central part of this layer, a circular, high-resistive feature has been modeled. This feature displays sharp resistivity contrasts with the surrounding less resistive medium, suggesting a distinct structural or compositional difference.

<u>Lithology and Structural Interpretation</u>

The high resistivity uppermost layer (220 -1000 Ω m) represents the overburden, composed primarily of sands, clays, and gravels. The high resistivity values indicate relatively dry, coarsegrained sands and gravels. The low-resistivity anomaly (75 Ω m) between 99 and 102 m likely represents a pocket of increased moisture content suggesting a potential preferential infiltration

pathway or recharge zone into the underlying Ocala limestone. The middle layer (low to intermediate resistivity) corresponds to the upper portion of the Ocala limestone. The low resistivity values $(9-110~\Omega m)$ show evidence of increased porosity and potential saturation from groundwater because of weathering or fracturing. The lenticular features within this layer are indicative of clay-filled cavities. The deeper layer with resistivity values ranging from 110 to 420 Ωm represents the more competent or less weathered portions of the Ocala limestone. The circular high-resistivity feature observed in the middle of this layer may be an artifact or a massive limestone block resistant to dissolution or a cavity filled with resistive material.

Line F

Line F, located in the southern section of the farm, covers a maximum length of 165 m. The starting point of this profile line is 60 m farther along the starting point of Line B. It should be noted that the survey for profile line F was acquired after Hurricane Helen. The inverted resistivity section (Figure 4.10) reveals a top layer with resistivity values ranging from 74 and 1000 Ω m. This uppermost layer, approximately 9 m thick, is not laterally continuous along the entire profile length, and it is made up of materials of varying resistivity values. High resistive materials (280 - 1000 Ω m) are observed at both ends of the profile, while a region of intermediate resistivity values ranging from 74 and 280 Ω m is observed between 48 and 120 m along the profile. Beneath the uppermost layer, between depths 9 and 22 m, lies a relatively low to intermediate resistivity layer with values ranging from 9 – 110 Ω m. This layer is 13 m thick with an irregular upper boundary and a sharp, horizontally consistent lower boundary in the central portion of the profile. Within this layer, a series of unconnected lentiform features with low resistivity (9 – 40 Ω m) are concentrated near the ends of the profile. Below the 13 m thick layer is a deeper layer that

extends to the bottom of the cross-section. This layer shows relatively high resistive materials (220 – 550 Ω m) at its western and eastern ends, displaying sharp contrasts with the surrounding less resistivity materials. At a depth of about 25 m, a vertical low-resistivity anomaly is observed in the central part of the deeper layer sandwiched between the two resistive units in the section.

Lithology and Structural Interpretation

The uppermost layer (74 -1000 Ω m) represents the overburden, composed primarily of sands, clays, and gravels. The variability in resistivity values shows a mixture of materials with different moisture content and compaction. The high resistivity values at the ends of the profile indicate relatively dry sands or gravels, while the intermediate resistivity values in the central portion suggest sandy-clay mixtures. The middle layer, likely representing the upper portion of the Ocala limestone, is highly weathered or saturated. The low resistivity values within the lenticular features indicate zones of high moisture content, possibly water-filled cavities or clay infills. The deeper layer in the resistivity section represents more competent and less weathered portions of the Ocala limestone. The high-resistivity zones at the western and eastern ends of the profile indicate massive limestone, while the central vertical low-resistivity anomaly within the layer may be a potential fracture. The low contrast in resistivity between this potential fracture zone and the surrounding resistive bedrock could be due to low water saturation or the infill materials being less conductive.

Line G

Profile G, located at the eastern end of the Angus Graham farm spans a total length of 165 m. The inverted resistivity section (Figure 4.11) shows a top layer characterized by materials of varying resistivity values ranging from 19 to 550 Ω m. Within this layer, there is a localized patch

of highly resistive materials of resistivity greater than $1000~\Omega m$ at a lateral distance of 123~m. This uppermost layer, about 5 m thick, extends horizontally along the entire profile length with no significant changes in layer thickness, only interrupted by a low resistive material (<19 Ωm) at 126 m lateral distance. Beneath the uppermost layer lies a 12 m thick low resistivity layer. This layer within the 6 and 18 m depth range is made up of materials of resistivity values ranging from about 19 to 96 Ωm and characterized by a series of isolated lentiform features. Below this 12 m thick layer is a sequence of horizontally layered materials that extend to the base of the ERT section with resistivity values ranging from 110 to 215 Ωm . At the western end of this deeper layer is a highly resistive material with resistivity values ranging from 250 – 550 Ωm .

Lithology and Structural Interpretation

The uppermost layer represents the overburden with resistivity variations reflecting differences in material composition. The resistivity range of the materials suggests sand and gravel materials in the overburden. The highly resistive patch (>1000 Ω m) at 123 m lateral distance likely indicates a localized zone of very dry, compacted sands. The low resistivity anomaly within the uppermost layer at 128 lateral distance suggests a localized preferential pathway for surface water infiltration. The 12 m thick low-resistivity layer suggests that the upper portion of the Ocala limestone is highly saturated. The moderate resistivity values of the deeper layer indicate that the Ocala limestone is weathered and saturated with groundwater. The highly resistive material (250-550 Ω m) at the western end indicates a zone of competent, less weathered limestone or could be an artifact.

Wildlife Management Areas

Two north-south trending surveys were carried out in the Albany Nursery and Chickasawhatchee Wildlife Management Areas. Figure 4.12 shows the orientation of the survey lines within the wildlife management areas.



Figure 4.12: Orientation of ERT survey line at the Chickasawhatchee Wildlife Management Areas.



Figure 4.13: Orientation of ERT survey line at the Chickasawhatchee Wildlife Management Areas.

Line C: Chickasawhatchee Wildlife Management Area

Profile C (Figure 4.14), located in the southwest of Dougherty County spans a total length of 165 m. The uppermost part of this section is about 5 m thick and is characterized by materials of very low resistivity values ranging from 9 to 75 Ω m. Within this layer, patches of high resistivity materials (110 – 420 Ω m) are observed between lateral distances of 30 - 48 m and 144 -156 m. The top layer is underlain by a layer of resistivity value (74 – 110 Ω m) that thickens progressively towards the eastern end of the section. This layer is observed at 5 m deep at the western end of the profile and between 5 and 15 m at the eastern end of the profile. Underlying this is another layer that extends to the bottom of the resistivity section. This layer is approximately 32 m thick and made up of materials with resistivity values ranging from 110-220 Ω m. There are localized patches

of high resistivity materials (\sim 250 Ω m) within this deeper layer. Generally, this layer is horizontally layered but thickens towards the western end of the profile.

Lithology and Structural Interpretation

The low-resistivity materials in the uppermost layer covering the entire extent of the profile line indicate a clay-rich zone with localized zones of dry sands or gravel between lateral distances of 30 - 48m and 144 - 156 m. The intermediate layer with resistivity values (74 - 110 Ω m) indicates a transition between the overburden and the underlying Ocala limestone. The resistivity values associated with this layer suggest a mix of weathered limestone and sandy clay materials. The observed thickening towards the eastern end indicates that the surface of the underlying layer has differential weathering. The resistivity range associated with the deeper layer (110 -220 Ω m) and thickness indicate that this layer corresponds to the Ocala limestone. The Ocala limestone in this profile shows low variability in resistivity readings across the profile indicating it is less heterogeneous.

Line D: Albany Nursery Wildlife Management Area

Profile D, located in the northwest of Dougherty County, spans a total length of 165 m. The inverted section (Figure 4.15) shows an uppermost layer characterized by very highly resistive materials of resistivity values ranging from 420 to 1200 Ω m. This layer, about 5 m thick, extends horizontally across the entire profile length with no significant variation in layer thickness. Beneath the uppermost layer lies an 8 m thick layer of resistivity values ranging from 38 to 110 Ω m. This layer extends from 5 to 13 m within the subsurface. Within this layer are a series of isolated lentiform features, with very conductive zones concentrated toward the eastern end of the profile. Underlying the 8 m thick layer is a deeper layer that extends to the bottom of the cross-

section. This layer, approximately 26 m thick, is made up of materials with resistivity values ranging from 110 to 550 Ω m. At the eastern end within this deeper layer, high-resistivity materials are observed, with values ranging between 220 and 550 Ω m.

<u>Lithology and Structural Interpretation</u>

The high resistivity of the uppermost layer indicates the presence of dry sands and gravels. The moderate to low resistivity values within the intermediate layer suggest a mix of materials such as sands, clay-rich zones, or weathered limestone. The isolated lentiform features and very conductive zones toward the eastern end may represent localized accumulations of saturated clays (clay-filled cavities) or water-filled voids. The high-resistivity materials at the eastern end of the deeper layer indicate more competent limestone, less weathered than the surrounding limestone.

4.4. Discussion of Results

The ERT profiles (resistivity models) were analyzed to delineate subsurface conditions within Dougherty County, with a focus on understanding subsurface characteristics such as depth-to-bedrock, spatial heterogeneity of the Ocala limestone and characterizing the presence and extent of fractures within the subsurface.

Depth-to-bedrock

In determining the depth-to-bedrock from the resistivity model sections, two assumptions were made to guide the interpretation. First, it was assumed that the contact between the uppermost layer, interpreted as the overburden, and the underlying Ocala limestone was laterally continuous across the survey area. For the resistivity model sections in which the overburden did not span the entire extent of the profile, an average thickness was calculated and used to estimate the depth-to-

bedrock. The second assumption was that the contact between the overburden and Ocala limestone was sharp rather than gradational.

The resistivity models from the surveys showed varying overburden thicknesses (depth-to-bedrock). Table 4.2 shows the bedrock depths and associated resistivity ranges interpreted from the seven model sections. It should be noted that the depths to bedrock seen on the resistivity model sections will differ from borehole depths observed on well logs or from borings. This is because the resistivity values of the materials that make up the overburden represent lateral and vertical averages associated with the sampling of current flow lines. The depth-to-bedrock observed on well logs or from borings gives the exact depth to the bedrock at a particular drill location.

Spatial Heterogeneity of Ocala Limestone

The Ocala limestone revealed significant spatial heterogeneity in the resistivity model sections. The Ocala limestone was divided into two sections/units: an upper and lower section. This observation is consistent with the findings of previous studies in the area that focused on the Ocala limestone (Hicks et al., 1987). The upper section was predominantly characterized by lentiform features of low resistivity values and generally had resistivity values ranging between 9 and 110 Ω m. This is a characteristic of a chalky, friable limestone. The lower section of the Ocala limestone was characterized by sequences of horizontally layered materials with higher resistivity values than the upper section. This indicates that the upper section of the Ocala limestone is more weathered and/or saturated than the lower section of the limestone unit. The high-resistivity lower section can be interpreted as more compact, intact limestones than the upper section. The ERT profiles also revealed alternating high and low resistivity zones beneath the overburden, indicating that the Ocala limestone is heterogeneous. These heterogeneities were delineated in all the profile

lines except in profile line C, which shows a homogeneous limestone body with embedded highresistivity blobs. The identified heterogeneities within the Ocala limestone show how complex groundwater movement is in Dougherty County.

Fractures

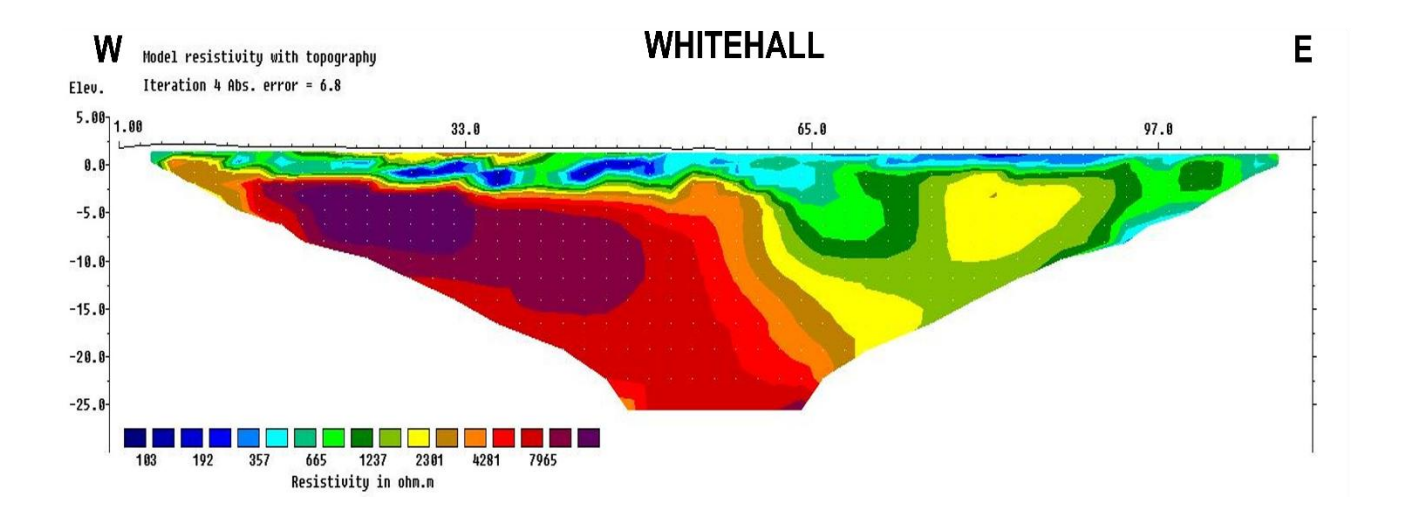
The resistivity profiles were examined for the presence of fractures within the subsurface to validate the correlation between hydrogeomorphological features mapped as fractures and the fractures at depth. Two potential resistivity anomalies have been identified within the Ocala limestone in profile Lines F and E. These anomalies are characterized by distinct vertical low resistivity contrasts with their surrounding media. This indicates potential fractures within the Ocala limestone. The fracture within the Ocala limestone in profile Line E is potentially induced by the drilled borehole in the middle of the survey line. The vertically oriented resistivity anomaly in the lower section of Line F suggests a possible fracture within the limestone unit. The smaller contrast in resistivity with the surrounding media could correspond to a fracture zone with low water content or smaller fracture density. However, the alignment of this fracture with the surface-mapped lineaments supports the hypothesis that these features are indicative of structural discontinuities within the Ocala limestone.

Another important observation is that all the surveys conducted across lineaments or in lineament-dense areas consistently showed lower resistivity readings for the Ocala limestone compared to the survey conducted near well CA 11, which did not intersect any mapped lineament. The higher resistivity readings of the limestone unit in Line E suggest a compact, less weathered limestone. Though only one potential fracture was identified from the profile lines correlating to the mapped lineaments, the lower resistivity readings of the Ocala limestone in the surveys

conducted across lineaments or in lineament-dense areas suggest highly weathered, fractured, and saturated limestone units. Most of the available boreholes were concentrated outside the study area (Figure 4.1), limiting the ability to conduct surveys near them. Additionally, the Upper Floridan Aquifer does not outcrop within the study site, making it impossible to validate the identified fracture with ground-truth data directly. However, the ERT results align with the expected geological formations within the study region. Also, the forward model analyses confirm that the depth of the identified fracture zone in the Ocala limestone is within the resolved portions of the model section. Therefore, we are confident that these anomalies correspond to a fracture zone and/or area of preferential dissolution within the limestone unit.

Table 4.2: Bedrock depths and associated resistivity ranges interpreted from the seven model sections.

Line	Overburden Thickness	Resistivity Range of Overburden
	(m)	(Ωm)
A	6	220 -1000
В	7	38 -1000
C	5	9 - 75
D	5	420 - 1200
E	10.5	9 - 1000
F	9	74 - 1000
G	5	19 - 550



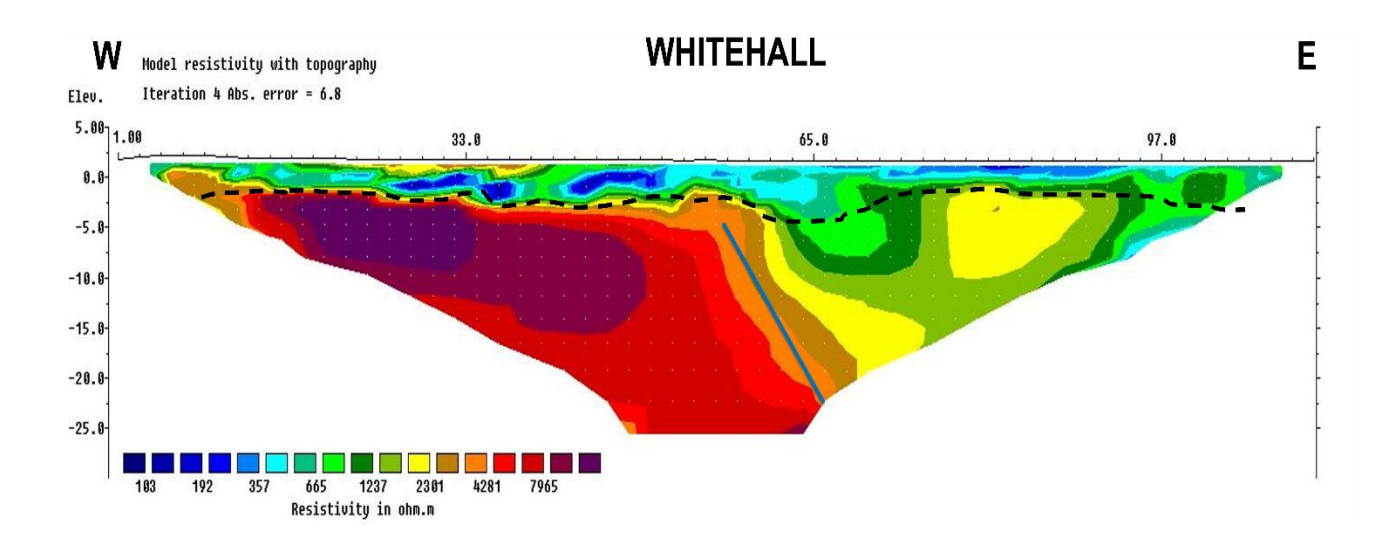
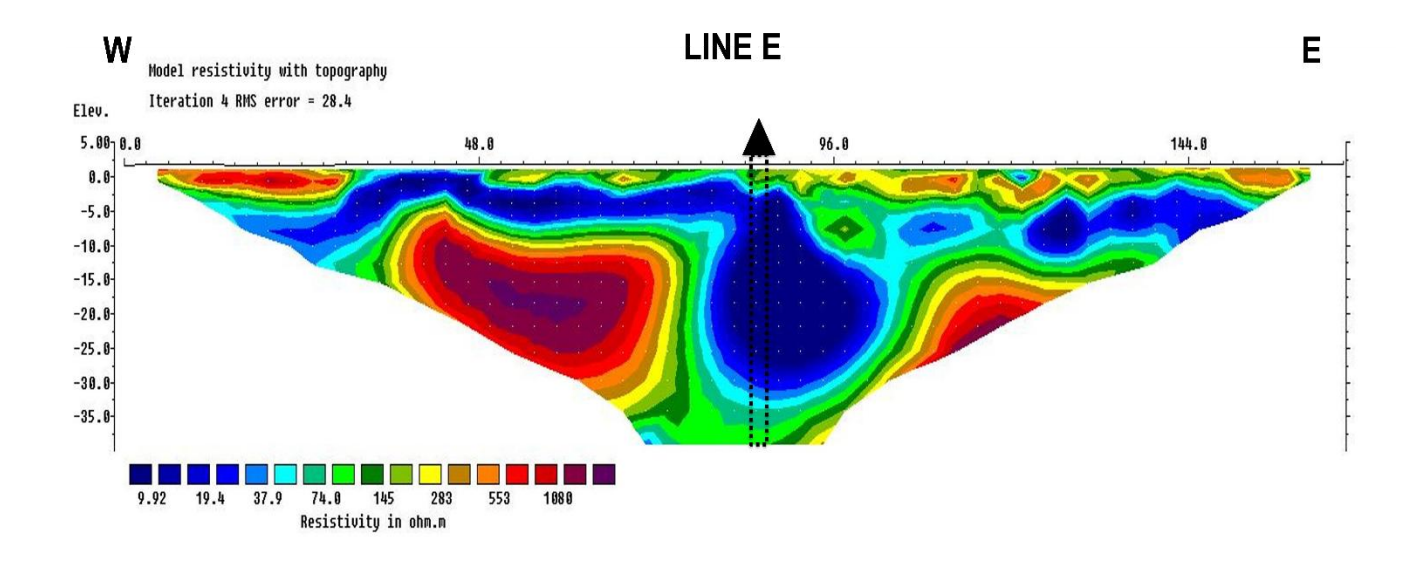


Figure 4.5: Uninterpreted (top) and interpreted (bottom) resistivity model sections of the survey conducted at Whitehall, University of Georgia, Athens campus. The black curvy dashed lines indicate the inferred soil-bedrock contact and the blue solid line indicates a potential fault.



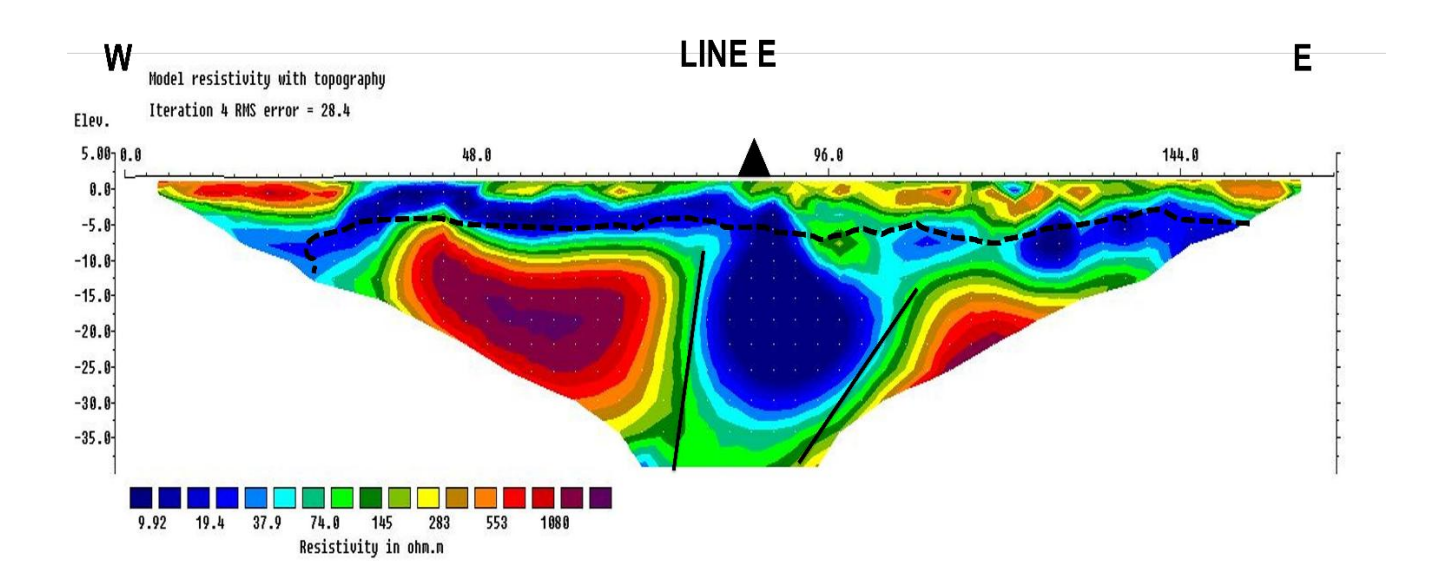
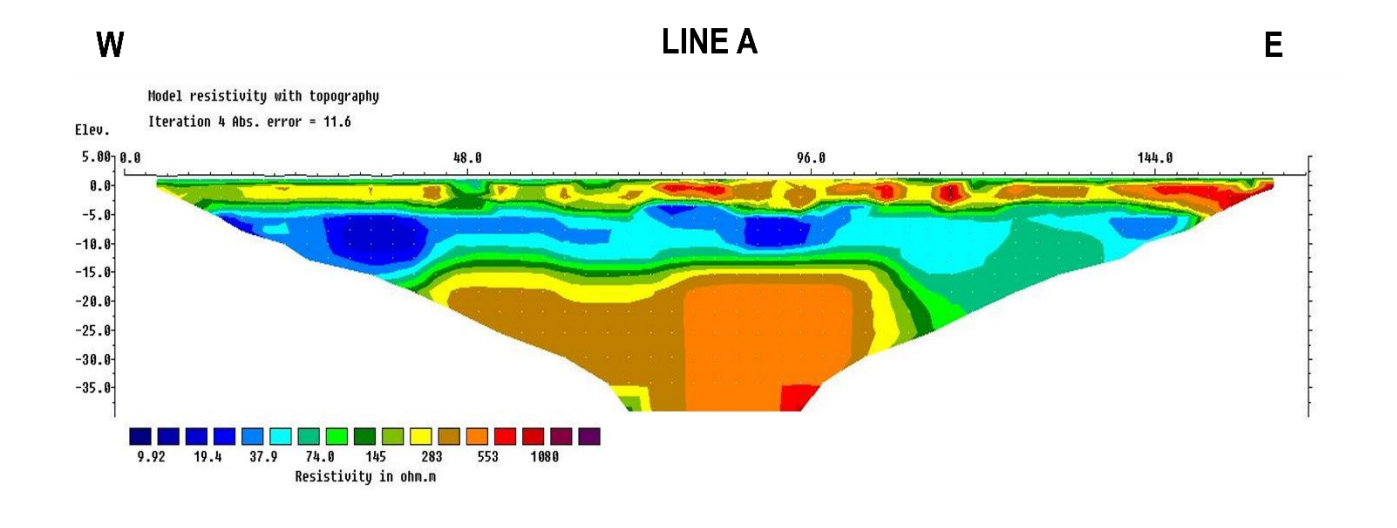


Figure 4.6: Uninterpreted (top) and interpreted (bottom) resistivity model sections of profile line E. The black curvy dashed lines indicate the inferred soil-bedrock contact and the black solid line indicates a potential fracture. The black triangle indicates the location of a well.



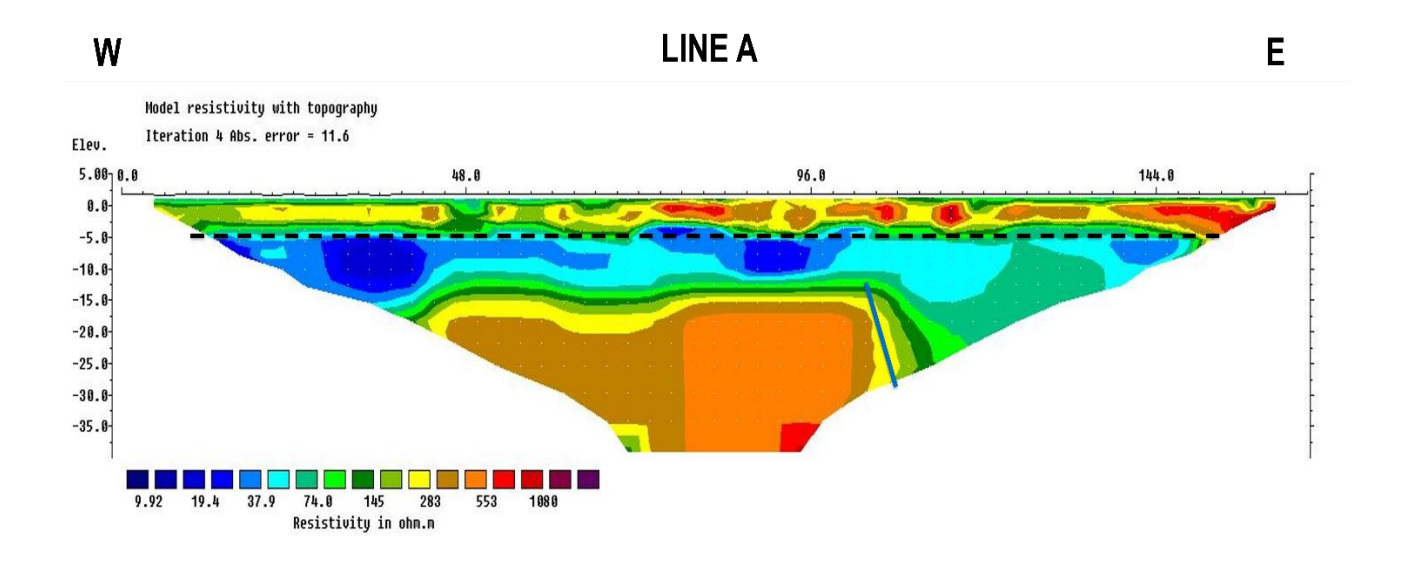
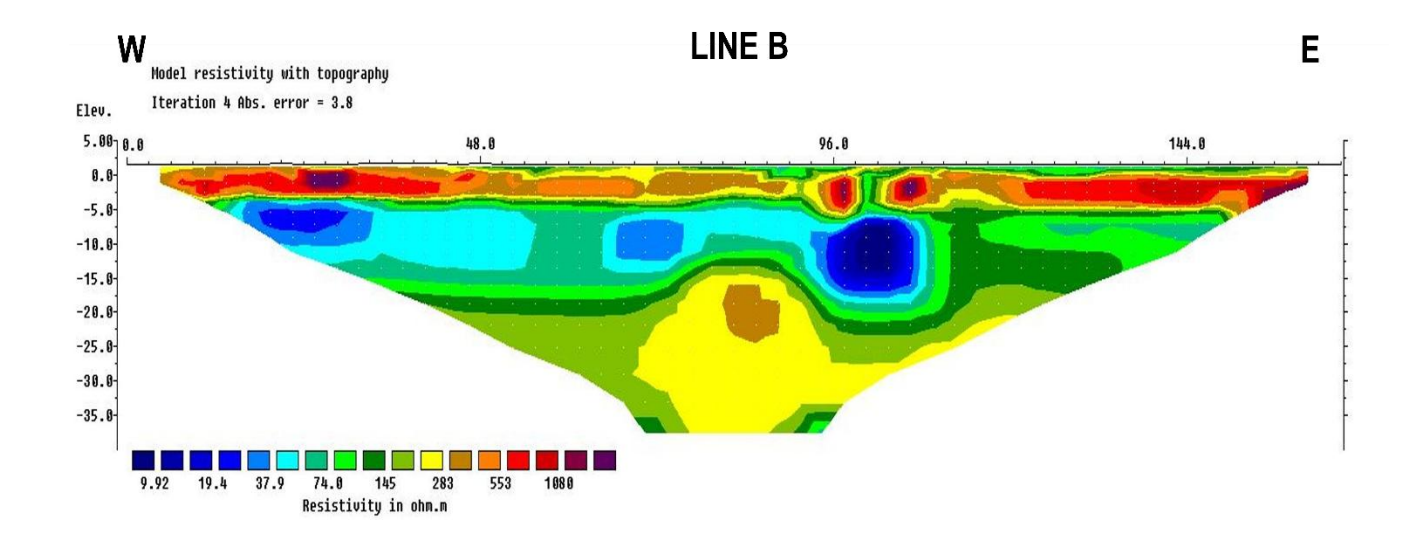


Figure 4.8: Uninterpreted (top) and interpreted (bottom) resistivity model sections of profile line A. The black horizontal dashed lines indicate the inferred soil-bedrock contact and the blue subvertical line indicate a potential fault.



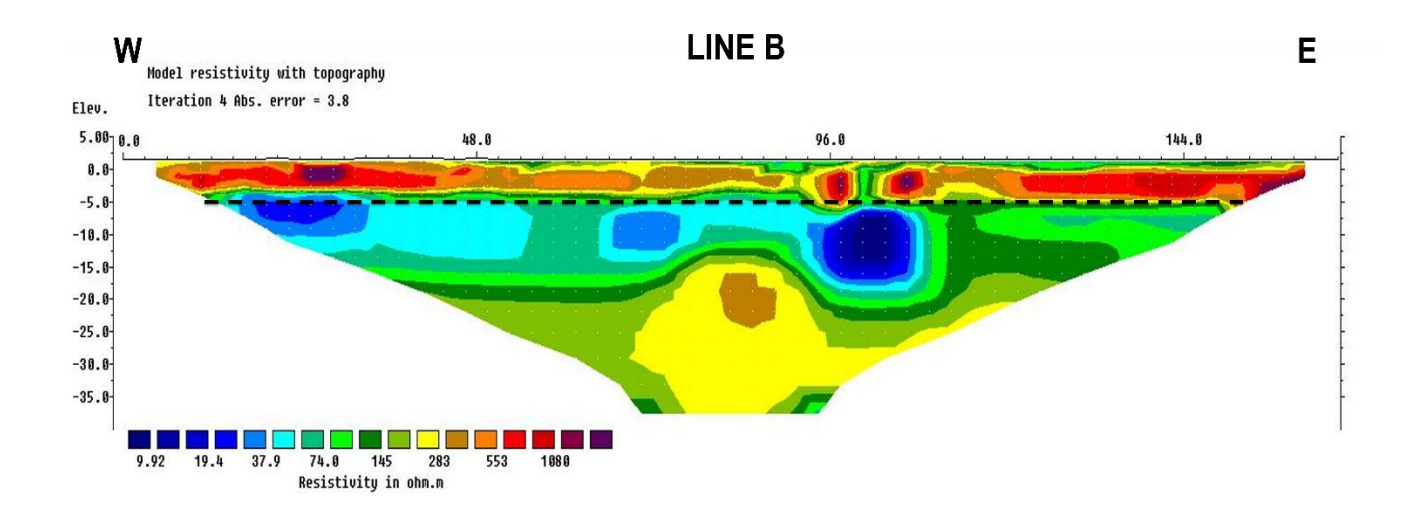
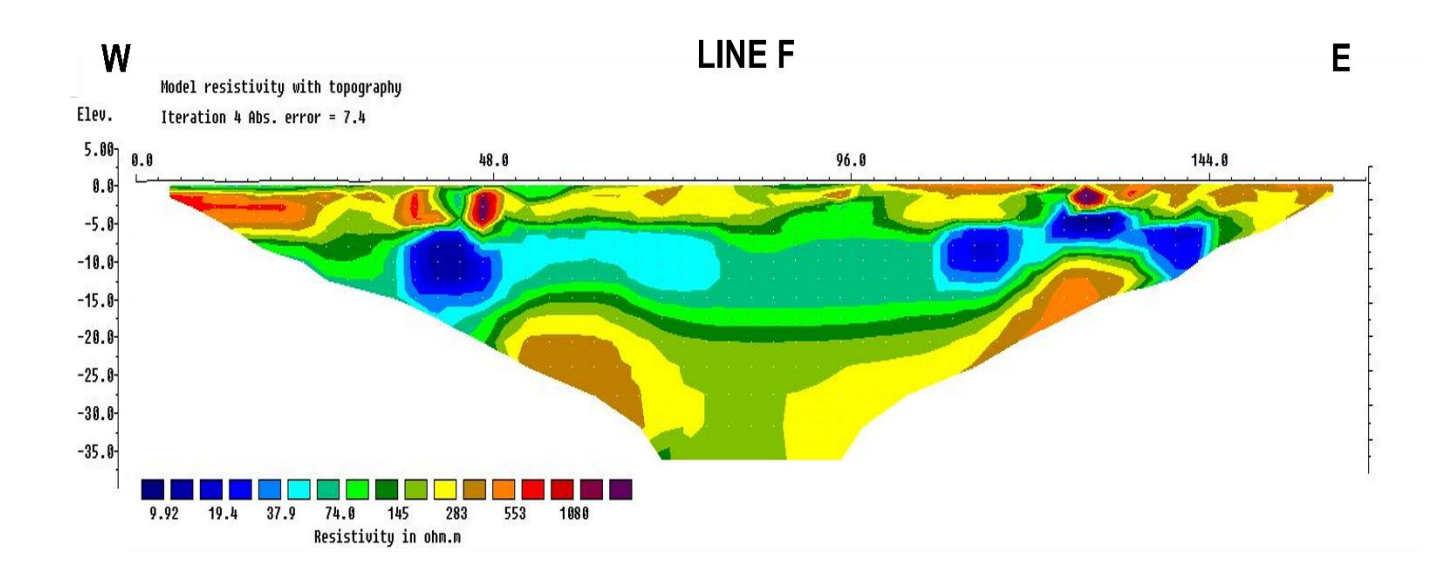


Figure 4.9: Uninterpreted (top) and interpreted (bottom) resistivity model sections of profile line B. The black horizontal dashed lines indicate the inferred soil-bedrock.



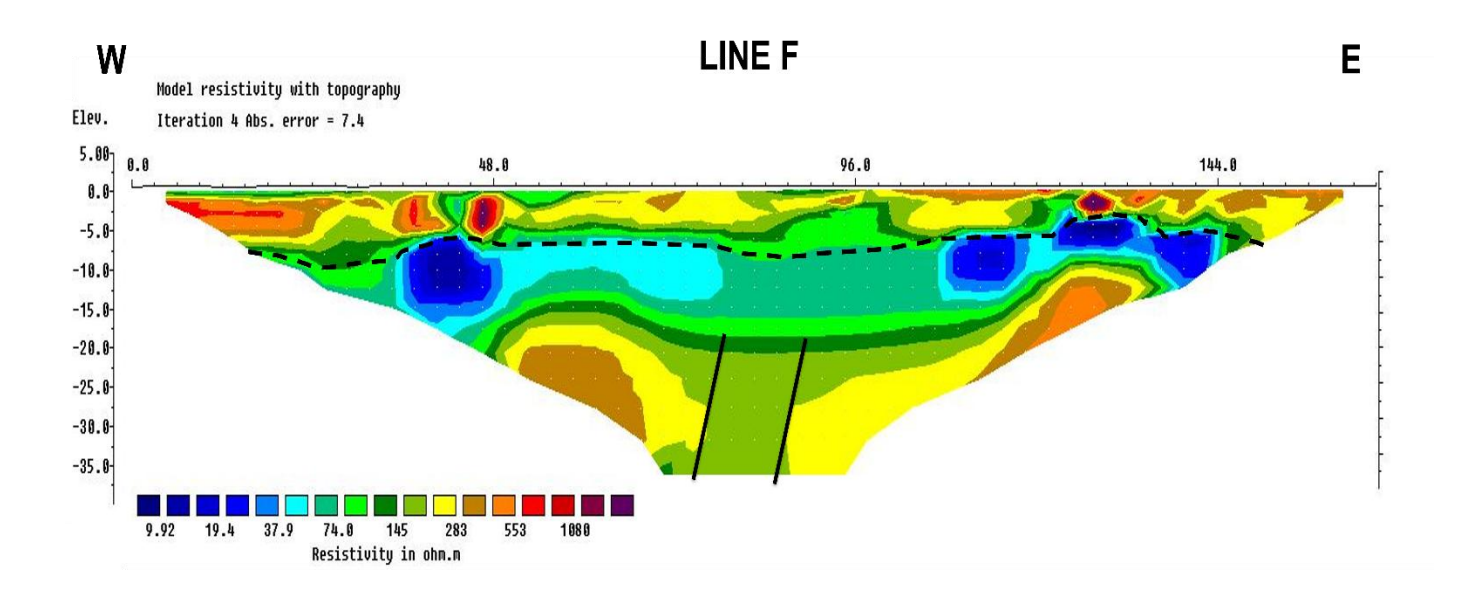
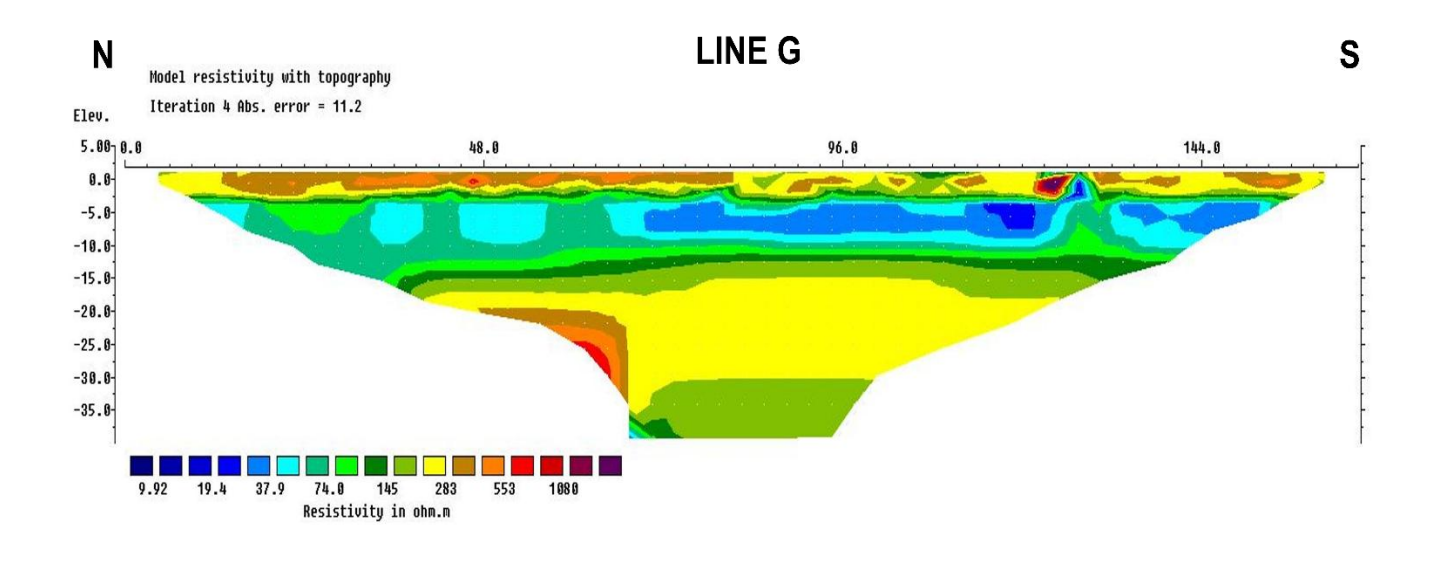


Figure 4.10: Uninterpreted (top) and interpreted (bottom) resistivity model sections of profile line F. The black curvy dashed lines indicate the inferred soil-bedrock contact and the black full line indicates a potential fracture zone.



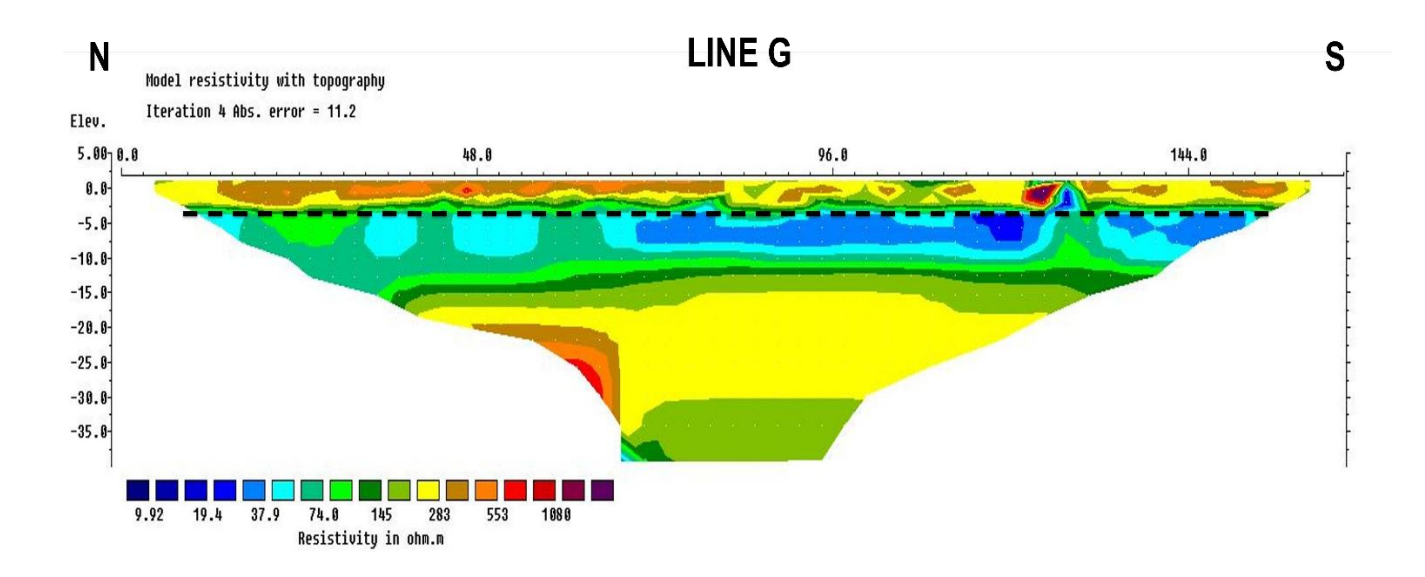
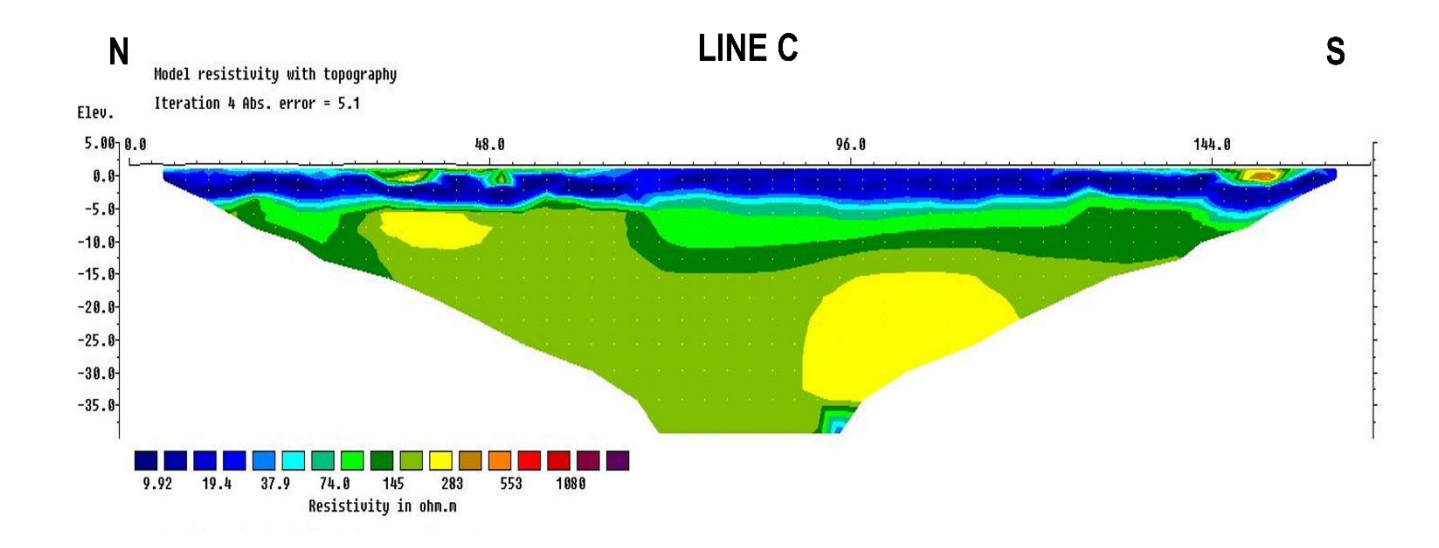


Figure 4.11: Uninterpreted (top) and interpreted (bottom) resistivity model sections of profile line G. The black horizontal dashed lines indicate the inferred soil-bedrock contact.



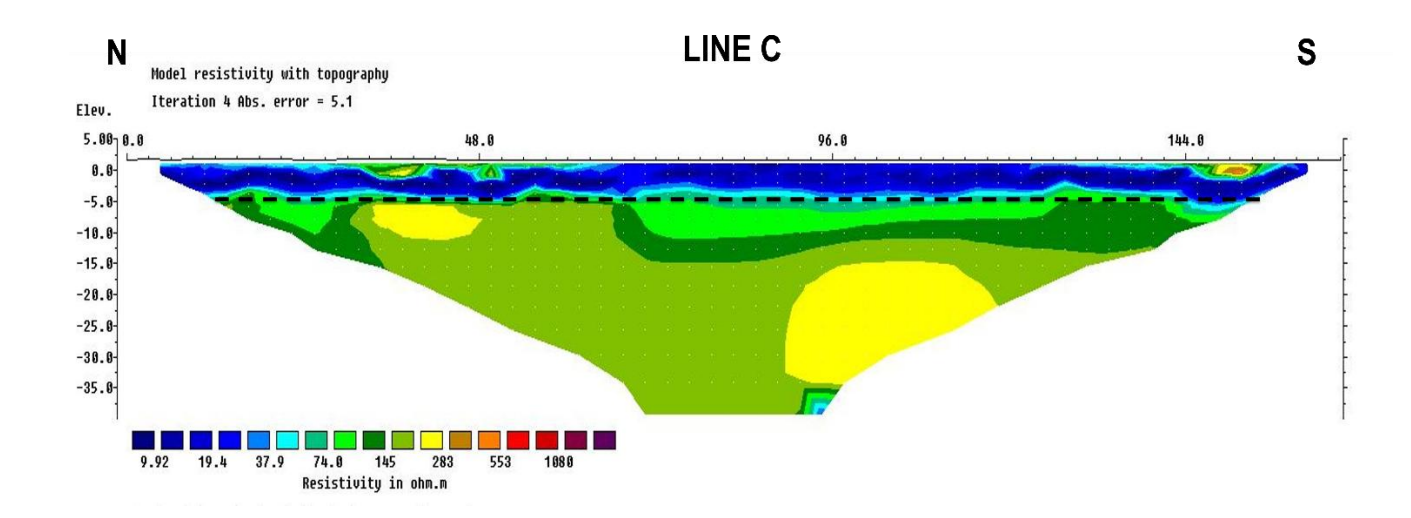
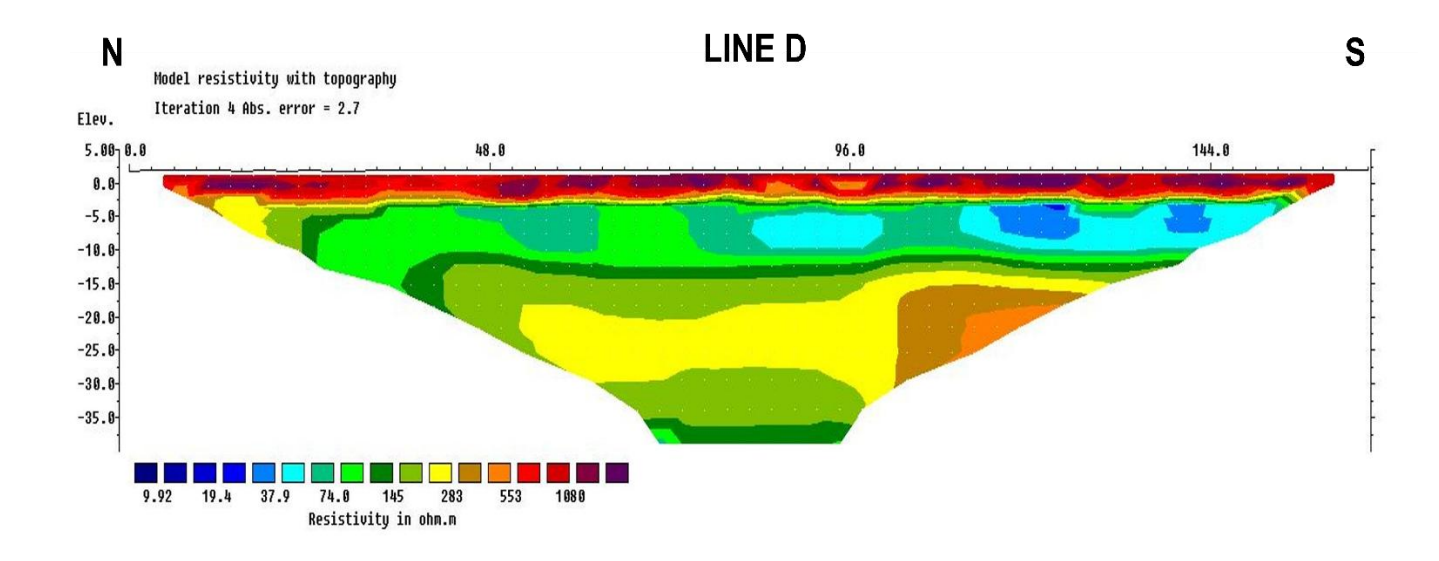


Figure 4.14: Uninterpreted (top) and interpreted (bottom) resistivity model sections of profile line C. The black horizontal dashed lines indicate the inferred soil-bedrock contact.



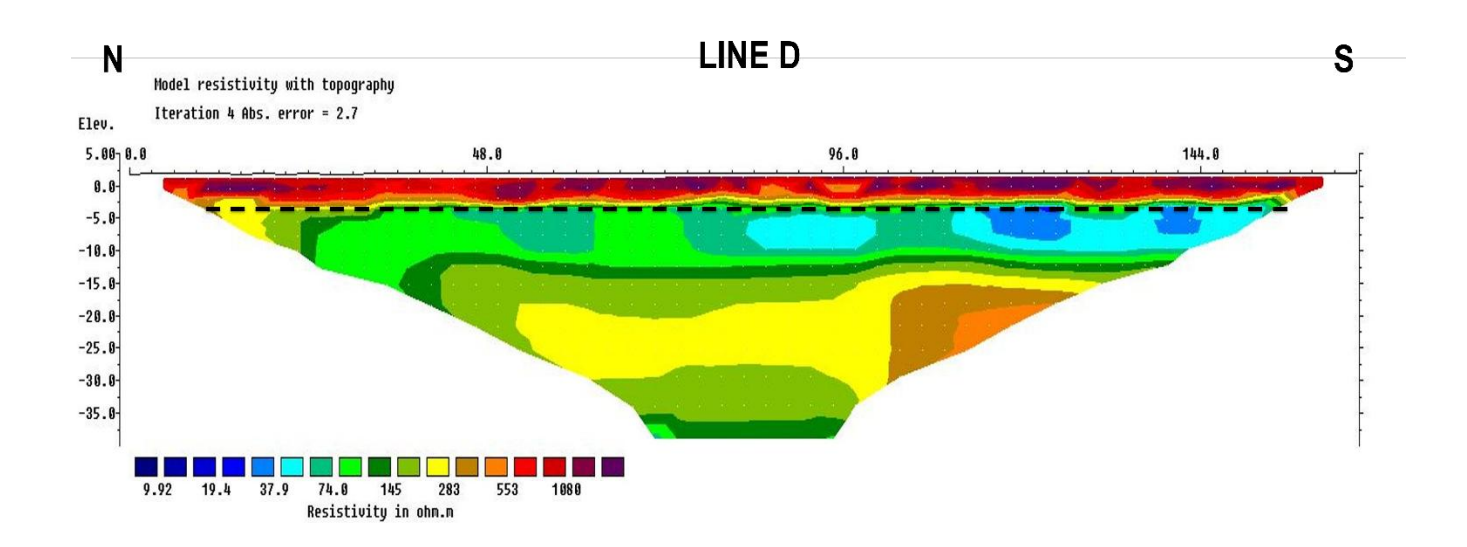


Figure 4.15: Uninterpreted (top) and interpreted (bottom) resistivity model sections of profile line D. The black horizontal dashed lines indicate the inferred soil-bedrock contact.

CHAPTER 5

CONCLUSIONS

5.1. Conclusions

Electrical Resistivity Tomography surveys were carried out in Dougherty County, southwest Georgia, to delineate the spatial heterogeneity of the Ocala limestone and validate the correlation between surface lineaments and underground bedrock fractures. Borehole geophysical logs were used to identify suitable locations for the ERT survey and as reference data for generating forward models to simulate ERT field responses.

The synthetic and field results reveal how the Electrical Resistivity Tomography technique can effectively delineate shallow subsurface architecture in karstic environments. The distinct signatures, expressed in terms of resistivity, helped delineate geological horizons and potential geological structures such as fractures and faults within the subsurface. The ERT technique was valuable in characterizing the complex relationships between geophysical resistivity signatures and geological architecture within the subsurface in the study area. Traditional point-based observations, such as local sampling data, are limited to spatial interpolation and may fail to detect the lateral variations in the heterogeneity of underlying geological units. ERT was able to detect the location of the Overburden-Ocala limestone and delineate the spatial heterogeneity within the Ocala limestone.

Results from the field data interpretation indicate that the overburden thickness in the study area varies significantly, ranging from approximately 5 to about 10.5 m. It was characterized by materials such as clay, sand, gravel and underlain by a highly weathered Ocala limestone, except

in the control survey conducted at a known well location. The upper unit of the Ocala limestone was characterized by lentiform features with low-to-intermediate resistivity values, interpreted as water-filled and or clay-filled cavities.

The resistivity model sections also indicated a potential interconnection between surface water and groundwater within the Ocala limestone, characterized by the potential infiltration (recharge) paths within the overburden. At most of the study sites, contaminants introduced at the land surface are likely to gradually seep through the overburden and eventually reach the Upper Floridan Aquifer. This percolation is expected to be slower where the overburden consists mainly of clay and faster in the other survey lines where sand and gravel dominate. Additionally, percolation will be slower in areas with a thick overburden and a greater depth to bedrock, such as Line E, whereas it will occur more rapidly in locations with a thinner overburden, including Lines C, D, and G. With an average overburden thickness of 9 m in western Dougherty County, this makes the Upper Floridan Aquifer susceptible to contamination in the region.

Out of the six ERT surveys conducted across mapped lineaments, only one (Line F) showed a potential fracture within the Ocala limestone. While remote sensing techniques such as aerial photographs and satellite images are useful for identifying potential fractures through lineament mapping, they provide limited field evidence regarding the nature and precise location of these fractures.

ERT was also able to detect the contact between the Overburden-Ocala limestone, though the resistivity contrast between the two interfaces was less distinct compared to interpretations from the borehole gamma ray logs. This discrepancy is likely due to the inherent diffusive nature of the ERT method, coupled with the smoothing applied to regularize the inversion. Lastly, although the study concentrated on relatively fewer study sites, detailed information gathered from this research is regarded as essential, if our collective understanding of fracturing, its role in groundwater movement, and the response of ERT in Dougherty County are to be significantly advanced.

5.2. Future Works

Building on the findings of this present study, in the future, additional ERT surveys with different electrode spacing and longer spreads could be used to further image the extent of the identified fractures. ERT surveys could also be extended to cover other areas within Dougherty County to validate the findings across a broader region. This would help refine the estimates of the number of surface lineaments that represent subsurface fractures in the region. Tracer tests can also be conducted to validate ERT-detected fractures as actual flow paths, providing a direct link between geophysical data and groundwater flow (Robert et al., 2012).

Additional geophysical methods, such as seismic refraction and gravity methods, could also be used to complement the ERT results. While vertically low resistivity anomalies may indicate fractures in ERT resistivity model sections, a high shear wave velocity or lower P-wave velocity may also represent a fractured bedrock in seismic refraction surveys (Carpenter et al., 1991; Parker Jr & Hawman, 2012). Also, fractures, especially when water-filled, create localized zones of lower bulk density compared to the surrounding intact rock. Gravity surveys can, therefore be used to detect these density variations as subtle negative anomalies in the Earth's gravitational field indicate potential fractures (Greenfield, 1979; Neumann, 1967).

REFERENCES

- Acharya, T., & Mallik, S. B. (2012). Analysis of lineament swarms in Precambrian metamorphic rocks in India. Journal of Earth System Science, 121, 453–462.
- Acharya, T., Nag, S. K., & Basumallik, S. (2012). Hydraulic significance of fracture correlated lineaments in Precambrian rocks in Purulia district, West Bengal. Journal of the Geological Society of India, 80, 723–730.
- Ahmadi, H., & Pekkan, E. (2021). Fault-based geological lineaments extraction using remote sensing and GIS—a review. Geosciences, 11(5), 183.
- Aizebeokhai, A. P. (2010). 2D and 3D geoelectrical resistivity imaging: Theory and field design. Scientific Research and Essays, 5(23), 3592–3605.
- Al Hagrey, S. A. (2012). 2D optimized electrode arrays for borehole resistivity tomography and CO 2 sequestration modelling. *Pure and Applied Geophysics*, *169*, 1283–1292.
- Alhassan, D. U., Obiora, D. N., Okeke, F. N., & Ibuot, J. U. (2018). Investigation of groundwater potential of southern Paiko, northcentral Nigeria, using seismic refraction method. Modeling Earth Systems and Environment, 4, 555–564.
- Alonso-Contes, C. A. (2011). Lineament mapping for groundwater exploration using remotely sensed imagery in a karst terrain: Rio Tanama and Rio de Arecibo basins in the northern karst of Puerto Rico. Michigan Technological University.
- Anderson, N. L., Apel, D. B., & Ismail, A. (2006). Assessment of karst activity at highway construction sites using the electrical resistivity method (Greene and Jefferson Counties, Missouri). University of Missouri--Rolla. Center for Infrastructure Engineering Studies.
- Aspinall, A., & Gaffney, C. F. (2001). The Schlumberger array—potential and pitfalls in archaeological prospection. *Archaeological Prospection*, 8(3), 199–209.

- Asquith, G. B., Krygowski, D., & Gibson, C. R. (2004). Basic well log analysis (Vol. 16).

 American Association of Petroleum Geologists Tulsa.
- Balasco, M., Lapenna, V., Rizzo, E., & Telesca, L. (2022). Deep electrical resistivity tomography for geophysical investigations: the state of the art and future directions. Geosciences, 12(12), 438.
- Bakar, N. A. A., Talib, M. K. A., Arifin, S. N. H., Madun, A., Tajudin, S. A. A., Dan, M. F. M.,
 Pakir, F., & Abd Malik, A. K. (2024). Relationship of Resistivity Value with the Ground
 Material Information Obtained from Borehole Data: Case study.
- Barker, R. D. (1981). The offset system of electrical resistivity sounding and its use with a multicore cable. Geophysical Prospecting, 29(1), 128–143.
- Barrett, B., Heinson, G., Hatch, M., & Telfer, A. (2002). Geophysical methods in saline groundwater studies: locating perched water tables and fresh-water lenses. Exploration Geophysics, 33(2), 115–121.
- Bechtel, T. D., Bosch, F. P., & Gurk, M. (2014). Geophysical methods. In Methods in karst hydrogeology (pp. 171–199). CRC Press.
- Benson, R. C., Glaccum, R. A., & Noel, M. R. (1982). Geophysical techniques for sensing buried wastes and waste migration. Environmental Monitoring Systems Laboratory, Office of Research and
- Bernard, J., Leite, O., Vermeersch, F., Instruments, I., & Orleans, F. (2006). Multi-electrode resistivity imaging for environmental and mining applications. IRIS Instruments, Orleans.
- Binley, A., & Slater, L. (2020). Resistivity and induced polarization: Theory and applications to the near-surface earth. Cambridge University Press.
- Botha, W. J. (1975). Horizontal electrical profiling in groundwater exploration.

- Boyer, R., & McQueen, J. (1964). Comparison of mapped rock fractures and airphoto linear features. Photogrammetric Engineering and Remote Sensing, 30(4), 630–635.
- Brantly, J. E. (1916). A report on the limestones and marls of the Coastal Plain of Georgia (Issue 21). Blosser.
- Brook, G. A., & Allison, T. L. (1983). Fracture mapping and ground subsidence susceptibility modeling in covered karst terrain: Dougherty County, Georgia. PH Dougherty (Réd.). Environmental Karst. Editions GeoSpeleo, Cincinnati, 91–108.
- Brown, N. N. (1994). Integrating structural geology with remote sensing in hydrogeological resource evaluation and exploration. Proceedings of the Thematic Conference on Geologic Remote Sensing, 1, I–144.
- Buselli, G., & Lu, K. (2001). Groundwater contamination monitoring with multichannel electrical and electromagnetic methods. Journal of Applied Geophysics, 48(1), 11–23.
- Butler, J. J. (2005). Hydrogeological methods for estimation of spatial variations in hydraulic conductivity. Hydrogeophysics, 23–58.
- Cahalan, M. D., & Milewski, A. M. (2018). Sinkhole formation mechanisms and geostatistical-based prediction analysis in a mantled karst terrain. Catena, 165, 333–344.
- Caran, S. C. (1982). Lineament analysis and inference of geologic structure: examples from the Balcones Ouachita trend of Texas. Virtual Landscapes of Texas.
- Cardarelli, E., & De Donno, G. (2019). Advances in electric resistivity tomography: Theory and case studies. In Innovation in near-surface geophysics (pp. 23–57). Elsevier.
- Cardarelli, E., & Fischanger, F. (2006). 2D data modeling by electrical resistivity tomography for complex subsurface geology. Geophysical Prospecting, 54(2), 121–133.

- Carpenter, P. J., Calkin, S. F., & Kaufmann, R. S. (1991). Assessing a fractured landfill cover using electrical resistivity and seismic refraction techniques. Geophysics, 56(11), 1896–1904.
- Carrière, S. D., Chalikakis, K., Sénéchal, G., Danquigny, C., & Emblanch, C. (2013). Combining electrical resistivity tomography and ground penetrating radar to study geological structuring of karst unsaturated zone. Journal of Applied Geophysics, 94, 31–41.
- Carruthers, R. M., Greenbaum, D., Peart, R. J., & Herbert, R. (1991). Geophysical investigations of photolineaments in southeast Zimbabwe. Quarterly Journal of Engineering Geology and Hydrogeology, 24(4), 437–451.
- Casper, J., Ruth, B., & Degner, J. (1981). A remote sensing evaluation of potential for sinkhole occurrence.
- Chalikakis, K., Plagnes, V., Guerin, R., Valois, R., & Bosch, F. P. (2011). Contribution of geophysical methods to karst-system exploration: an overview. Hydrogeology Journal, 19(6), 1169.
- Chambers, J., Meldrum, P., Gunn, D., Wilkinson, P., Uhlemann, S., Kuras, O., & Swift, R. (2015).

 Proactive infrastructure monitoring and evaluation (PRIME): a new electrical resistivity tomography system for remotely monitoring the internal condition of geotechnical infrastructure assets. 3rd International Workshop on Geoelectrical Monitoring (GELMON).
- Chandra, S., Rao, V. A., Krishnamurthy, N. S., Dutta, S., & Ahmed, S. (2006). Integrated studies for characterization of lineaments used to locate groundwater potential zones in a hard rock region of Karnataka, India. Hydrogeology Journal, 14, 767–776.

- Cheng, Q., Tao, M., Chen, X., & Binley, A. (2019). Evaluation of electrical resistivity tomography (ERT) for mapping the soil–rock interface in karstic environments. Environmental Earth Sciences, 78, 1–14.
- Chik, Z., & Islam, S. M. T. (2012). Finding soil particle size through electrical resistivity in soil site investigations. Electronic Journal of Geotechnical Engineering, 17, 1867–1876.
- Christensen, N. B. (2000). Difficulties in determining electrical anisotropy in subsurface investigations [Link]. Geophysical Prospecting, 48(1), 1–19.
- Clarke, J. S., Faye, R. E., & Brooks, R. (1984). Hydrogeology of the Clayton aquifer of southwest Georgia. Available from OFSS, USGS Box 25425, Lakewood, CO 80225. Georgia State Hydrologic Atlas 13, 1984. 89 p, 30 Fig, 5 Tab, 37 Ref.
- Coker, J. O. (2012). Vertical electrical sounding (VES) methods to delineate potential groundwater aquifers in Akobo area, Ibadan, South-western, Nigeria. Journal of Geology and Mining Research, 4(2), 35–42.
- Cook, P. G. (2003). A guide to regional groundwater flow in fractured rock aguifers. Citeseer.
- Cosgrove, W. J., & Loucks, D. P. (2015). Water management: Current and future challenges and research directions. Water Resources Research, 51(6), 4823–4839.
- Dahlin, T., & Zhou, B. (2004). A numerical comparison of 2D resistivity imaging with 10 electrode arrays. Geophysical Prospecting, 52(5), 379–398.
- Daily, W., Ramirez, A., Binley, A., & LeBrecque, D. (2004). Electrical resistance tomography. The Leading Edge, 23(5), 438–442.
- Dey, A., & Morrison, H. F. (1979). Resistivity modeling for arbitrarily shaped two-dimensional structures. Geophysical Prospecting, 27(1), 106–136.

- Dhakate, R., Singh, V. S., Negi, B. C., Chandra, S., & Rao, V. A. (2008). Geomorphological and geophysical approach for locating favorable groundwater zones in granitic terrain, Andhra Pradesh, India. Journal of Environmental Management, 88(4), 1373–1383.
- Dobecki, T. L., & Upchurch, S. B. (2006). Geophysical applications to detect sinkholes and ground subsidence. The Leading Edge, 25(3), 336–341.
- Edwards, J. T., & Hillel, A. J. (1977). The electrical resistivity of GP zones. The Philosophical Magazine: A Journal of Theoretical Experimental and Applied Physics, 35(5), 1221–1229.
- Endres, A. L., Clement, W. P., & Rudolph, D. L. (2000). Ground penetrating radar imaging of an aquifer during a pumping test. Groundwater, 38(4), 566–576.
- Erkan, K. (2008). A comparative overview of geophysical methods. Geodetic Science and Surveying, 3(488), 29–45.
- Eze, I. E. (2024). Groundwater Exploration and Management using Geophysical and Remote Sensing Techniques: a Review. International Journal of Science and Management Studies (IJSMS), 7(4). https://doi.org/10.51386/25815946/ijsms-v7i4p128
- Fazzito, S. Y., Rapalini, A. E., Cortés, J. M., & Terrizzano, C. M. (2009). Characterization of Quaternary faults by electric resistivity tomography in the Andean Precordillera of Western Argentina. Journal of South American Earth Sciences, 28(3), 217–228.
- Fields Jr, J., Tandy, T., Halihan, T., Ross, R., Beak, D., Neill, R., & Groves, J. (2022). Electrical resistivity imaging of an enhanced aquifer recharge site. Journal of Geophysics and Engineering, 19(5), 1095–1110.
- Florinsky, I. V. (1996). Quantitative topographic method of fault morphology recognition. Geomorphology, 16(2), 103–119.

- Foster, S., Chilton, J., Nijsten, G.-J., & Richts, A. (2013). Groundwater—a global focus on the 'local resource.' Current Opinion in Environmental Sustainability, 5(6), 685–695.
- Foulger, G. R., & Pierce, C. (2007). Geophysical methods in geology. Teaching Handbook, University of Durham, UK.
- Fountain, J. C., Jacobi, R. D., & Fountain, M. J. (1999). Detection of fracture intensification domains using hyperspectral remote sensing data: a case study in Allegany County, New York. Ontario Petroleum Institute Thirty-Eighth Annual Conference, Gilbert, DW (Chairperson), Ontario Petroleum Institute, London, ON, Canada, 38(13), 1–10.
- Frost, J. D., & Burns, S. E. (2003). In Situ Subsurface Characterization. The Civil Engineering Handbook.
- Gabrielsen, R. H., & Braathen, A. (2014). Models of fracture lineaments—Joint swarms, fracture corridors and faults in crystalline rocks, and their genetic relations. Tectonophysics, 628, 26–44.
- Gaffney, C. (2008). Detecting trends in the prediction of the buried past: a review of geophysical techniques in archaeology. Archaeometry, 50(2), 313–336.
- Gallardo, L. A., & Meju, M. A. (2011). Structure-coupled multiphysics imaging in geophysical sciences. Reviews of Geophysics, 49(1).
- Galli, P. A. C., Giocoli, A., Peronace, E., Piscitelli, S., Quadrio, B., & Bellanova, J. (2014).

 Integrated near-surface geophysics across the active Mount Marzano Fault System (southern Italy): seismogenic hints. International Journal of Earth Sciences, 103, 315–325.
- Garambois, S., Sénéchal, P., & Perroud, H. (2002). On the use of combined geophysical methods to assess water content and water conductivity of near-surface formations. Journal of Hydrology, 259(1–4), 32–48.

- Gay Jr, S. P. (2012). Joints, Linears, and Lineaments—The Basement Connection. Adapted from Oral Presentation given at AAPG Rocky Mountain Section Meeting, Grand Junction, Colorado, 9–12.
- Gelis, C., Noble, M., Cabrera, J., Penz, S., Chauris, H., & Cushing, E. M. (2016). Ability of high-resolution resistivity tomography to detect fault and fracture zones: application to the Tournemire experimental platform, France. Pure and Applied Geophysics, 173, 573–589.
- Gleick, P. H. (1998). Water in crisis: paths to sustainable water use. Ecological Applications, 8(3), 571–579.
- Greenfield, R. J. (1979). Review of geophysical approaches to the detection of karst. Bulletin of the Association of Engineering Geologists, 16(3), 393–408.
- Godfray, G., & Tembo, M. M. (2024). Assessment of groundwater potentiality in semi-arid area of central Tanzania. implication from geology and geomorphology of the dodoman supergroup. Geology, Ecology, and Landscapes, 8(2), 165–184.
- Goldman, M., & Neubauer, F. M. (1994). Groundwater exploration using integrated geophysical techniques. Surveys in Geophysics, 15, 331–361.
- Gordon, D. W. (2020). Groundwater quality and groundwater levels in Dougherty County, Georgia, April 2019 through March 2020. US Geological Survey.
- Gordon, D. W., & Gonthier, G. (2017). Hydrology of the Claiborne aquifer and interconnection with the Upper Floridan aquifer in southwest Georgia. US Geological Survey.
- Griffiths, D. H., & Barker, R. D. (1993). Two-dimensional resistivity imaging and modelling in areas of complex geology. Journal of Applied Geophysics, 29(3–4), 211–226.
- Griffiths, D. H., & King, R. F. (2013). Applied geophysics for geologists and engineers: the elements of geophysical prospecting. Elsevier.

- Gunawan, T. (1997). The contribution of aerial photographs in evaluation of Bribin Catchment area, Gunung Kidul, Yogyakarta, Indonesia. The Indonesian Journal of Geography, 29(73), 49–65.
- Hagrey, S. A. al. (2012). Geophysical imaging techniques. Measuring Roots: An Updated Approach, 151–188.
- Haryono, E., & Day, M. (2004). Landform differentiation within the Gunung Kidul Kegelkarst, Java, Indonesia. Journal of Cave and Karst Studies, 66(2), 62–69.
- Hasan, M., Shang, Y., Jin, W., & Akhter, G. (2020). An engineering site investigation using non-invasive geophysical approach. Environmental Earth Sciences, 79(11), 265.
- Hashim, M., Ahmad, S., Johari, M. A. M., & Pour, A. B. (2013). Automatic lineament extraction in a heavily vegetated region using Landsat Enhanced Thematic Mapper (ETM+) imagery. Advances in Space Research, 51(5), 874–890.
- Hayes, L. R., Maslia, M. L., & Meeks, W. C. (1983). Hydrology and model evaluation of the principal artesian aquifer, Dougherty Plain, southwest Georgia (Vol. 97). Georgia Geologic Survey.
- Henriksen, H., & Braathen, A. (2006). Effects of fracture lineaments and in-situ rock stresses on groundwater flow in hard rocks: a case study from Sunnfjord, western Norway. Hydrogeology Journal, 14, 444–461.
- Herman, R. (2001). An introduction to electrical resistivity in geophysics. American Journal of Physics, 69(9), 943–952.
- Hess, D. P. (2009). Using geospatial analyses to understand Laurentide Ice Sheet dynamics in New York\State from landform morphometry and till fabric. Unpublished Doctoral Thesis, University of Buffalo, Buffalo, NY, USA.

- Hicks, D. W., Gill, H. E., & Longsworth, S. A. (1987). Hydrogeology, chemical quality, and availability of ground water in the Upper Floridan Aquifer, Albany area, Georgia (Issues 87–4145). Department of the Interior, US Geological Survey.
- Hicks, D. W., Krause, R. E., & Clarke, J. S. (1981). Geohydrology of the Albany area, Georgia.
- Hine, G. T. (1970). Relation of fracture traces, joints, and ground-water occurrence in the area of the Bryantsville quadrangle, central Kentucky (Issue 3). Kentucky Geological Survey, University of Kentucky.
- Hobbs, W. H. (1904). Lineaments of the Atlantic border region. Bulletin of the Geological Society of America, 15(1), 483–506.
- Hoffmann, J., & Sander, P. (2007). Remote sensing and GIS in hydrogeology. Hydrogeology Journal, 15(1), 1–3.
- Hoover, D. B., Klein, D. P., Campbell, D. C., & du Bray, E. (1995). Geophysical methods in exploration and mineral environmental investigations. Preliminary Compilation of Descriptive Geoenvironmental Mineral Deposit Models: USGS Open-File Report, 95(831), 19–27.
- Jacobi, R. D. (2002). Basement faults and seismicity in the Appalachian Basin of New York State.

 Tectonophysics, 353(1–4), 75–113.
- Jennifer Hafer. (2022). Southwest Georgia: Working Together. GeorgiaTrend.
- John E. Moore. (2005). Geological Occurrence of Groundwater. Ground Water Hydrology.
- Jordan, G., Meijninger, B. M. L., Van Hinsbergen, D. J. J., Meulenkamp, J. E., & Van Dijk, P. M. (2005). Extraction of morphotectonic features from DEMs: Development and applications for study areas in Hungary and NW Greece. International Journal of Applied Earth Observation and Geoinformation, 7(3), 163–182.

- Kana, J. D., Djongyang, N., Raïdandi, D., Nouck, P. N., & Dadjé, A. (2015). A review of geophysical methods for geothermal exploration. Renewable and Sustainable Energy Reviews, 44, 87–95.
- Karki, R., Srivastava, P., Kalin, L., Mitra, S., & Singh, S. (2021). Assessment of impact in groundwater levels and stream-aquifer interaction due to increased groundwater withdrawal in the lower Apalachicola-Chattahoochee-Flint (ACF) River Basin using MODFLOW. *Journal of Hydrology: Regional Studies*, 34, 100802.
- Kearey, P., Brooks, M., & Hill, I. (2002). An introduction to geophysical exploration (Vol. 4). John Wiley & Sons.
- Keys, W. S. (2017). A practical guide to borehole geophysics in environmental investigations. Routledge.
- Keys, W. S., & MacCary, L. M. (1971). Application of borehole geophysics to water-resources investigations. US Government Printing Office Washington, DC.
- Knödel, K., Lange, G., Voigt, H.-J., Seidel, K., & Lange, G. (2007). Direct current resistivity methods. Environmental Geology: Handbook of Field Methods and Case Studies, 205–237.
- Lattman, L. H. (1958). Technique of mapping geologic fracture traces and lineaments on aerial photographs. Photogrammetric Engineering, 24(4), 568–576.
- Lattman, L. H., & Matzke, R. H. (1961). Geological significance of fracture traces. Photogrammetric Engineering, 27(3), 435–438.
- Lattman, L. H., & Parizek, R. R. (1964). Relationship between fracture traces and the occurrence of ground water in carbonate rocks. Journal of Hydrology, 2(2), 73–91.

- Linde, N., Chen, J., Kowalsky, M. B., & Hubbard, S. (2006). Hydrogeophysical parameter estimation approaches for field scale characterization. In Applied hydrogeophysics (pp. 9–44). Springer.
- Loke, M. H. (2004). Tutorial: 2-D and 3-D electrical imaging surveys.
- Loke, M. H. (2011). Tutorial: 2-D and 3-D electrical imaging surveys, Geotomo Software Sdn. Bhd., Penang, Malaysia.
- Loke, M. H., Acworth, I., & Dahlin, T. (2003). A comparison of smooth and blocky inversion methods in 2D electrical imaging surveys. Exploration Geophysics, 34(3), 182–187.
- Loke, M. H., & Barker, R. D. (1996). Practical techniques for 3D resistivity surveys and data inversion1. Geophysical Prospecting, 44(3), 499–523.
- Loke, M. H., Chambers, J. E., Rucker, D. F., Kuras, O., & Wilkinson, P. B. (2013). Recent developments in the direct-current geoelectrical imaging method. Journal of Applied Geophysics, 95, 135–156.
- Lutenegger, A. J. (2021). In Situ Testing Methods in Geotechnical Engineering. CRC Press.
- Mabee, S. B., Curry, P. J., & Hardcastle, K. C. (2002). Correlation of lineaments to ground water inflows in a bedrock tunnel. Groundwater, 40(1), 37–43.
- Mabee, S. B., Hardcastle, K. C., & Wise, D. U. (1994). A method of collecting and analyzing lineaments for regional-scale fractured-bedrock aquifer studies. Groundwater, 32(6), 884–894.
- Magowe, M., & Carr, J. R. (1999). Relationship between lineaments and ground water occurrence in western Botswana. Groundwater, 37(2), 282–286.

- Maina, M. M., & Tudunwada, I. Y. (2017). Lineament mapping for groundwater exploration in Kano state, Nigeria. International Journal of Advances in Agricultural & Environmental Engineering, 4, 226–229.
- Markos, M., Saka, A., Jule, L. T., Nagaprasad, N., & Ramaswamy, K. (2021). Groundwater potential assessment using vertical electrical sounding and magnetic methods: A case of Adilo Catchment, South Nations, Nationalities and Peoples Regional Government, Ethiopia. Concepts in Magnetic Resonance Part A, 2021(1), 5424865.
- Martin, G. I. (2010). Evaluating the location, extent, and condition of isolated wetlands in the Dougherty Plain, Georgia, USA.
- Martin, G. I., Hepinstall-Cymerman, J., & Kirkman, L. K. (2013). Six decades (1948–2007) of landscape change in the Dougherty Plain of southwest Georgia, USA. Southeastern Geographer, 53(1), 28–49.
- Martínez-Moreno, F. J., Galindo-Zaldívar, J., Pedrera, A., Teixido, T., Ruano, P., Peña, J. A., González-Castillo, L., Ruiz-Constán, A., López-Chicano, M., & Martín-Rosales, W. (2014). Integrated geophysical methods for studying the karst system of Gruta de las Maravillas (Aracena, Southwest Spain). Journal of Applied Geophysics, 107, 149–162.
- Mashala, M. J., Dube, T., Mudereri, B. T., Ayisi, K. K., & Ramudzuli, M. R. (2023). A systematic review on advancements in remote sensing for assessing and monitoring land use and land cover changes impacts on surface water resources in semi-arid tropical environments. Remote Sensing, 15(16), 3926.
- Masoud, A., & Koike, K. (2006). Tectonic architecture through Landsat-7 ETM+/SRTM DEM-derived lineaments and relationship to the hydrogeologic setting in Siwa region, NW Egypt. Journal of African Earth Sciences, 45(4–5), 467–477.

- Mazzullo, S. J. (2004). Overview of porosity evolution in carbonate reservoirs. Kansas Geological Society Bulletin, 79(1–2), 1–19.
- McGuire, K. (2007). Fracture, lineament, and seismic data: Indication of fault patterns in the Appalachian Basin in east-central New York State. State University of New York at Buffalo.
- Mickus, K. (2021). Geophysical methods. In Pollution Assessment for Sustainable Practices in Applied Sciences and Engineering (pp. 199–287). Elsevier.
- Middleton, M., Schnur, T., Sorjonen-Ward, P., & Hyvönen, E. (2015). Geological lineament interpretation using the object-based image analysis approach: results of semi-automated analyses versus visual interpretation. Geological Survey of Finland, Special Paper, 57, 135–154.
- Militzer, H., Rösler, R., & Lösch, W. (1979). Theoretical and experimental investigations for cavity research with geoelectrical resistivity methods. Geophysical Prospecting, 27(3), 640–652.
- Milsom, J., & Eriksen, A. (2013a). Field geophysics. EEGS 1720 South Bellaire, Suite 110, Denver, CO 80222-4303, USA.
- Milsom, J., & Eriksen, A. (2013b). Field geophysics. EEGS 1720 South Bellaire, Suite 110, Denver, CO 80222-4303, USA.
- Minor, T. (1995). Application of geographic information system technology to water well siting in Ghana, West Africa: a feasibility study. Desert Research Institute, Water Resources Institute.
- Mirzaei, L., Hafizi, M. K., & Riahi, M. A. (2021). Application of Dipole–Dipole, Schlumberger, and Wenner–Schlumberger Arrays in Groundwater Exploration in Karst Areas Using

- Electrical Resistivity and IP Methods in a Semi-arid Area, Southwest Iran. Water Resources in Arid Lands: Management and Sustainability, 81–89.
- Mishra, O. P., & Naskar, D. C. (2024). *Geophysical Methods: Fundamentals, Applications, and Case Studies*. CRC Press.
- Mleta, P. (2010). An Analysis of Groundwater in Mchinji District of Central Malawi. University of Fort Hare, Republic of South Africa, 1–39.
- Molina, E., Cultrone, G., Sebastián, E., Alonso, F. J., Carrizo, L., Gisbert, J., & Buj, O. (2011). The pore system of sedimentary rocks as a key factor in the durability of building materials. Engineering Geology, 118(3–4), 110–121.
- Mollard, J. D. (1988). First RM Hardy Memorial Lecture: Fracture lineament research and applications on the western Canadian plains. Canadian Geotechnical Journal, 25(4), 749–767.
- Mondal, N. C., Rao, V. A., Singh, V. S., & Sarwade, D. V. (2008). Delineation of concealed lineaments using electrical resistivity imaging in granitic terrain. Current Science, 1023–1030.
- Montane, J. M. (2001). Geophysical Analysis of a Central Florida Karst Terrain using Light Detection and Ranging (LIDAR) and Ground Penetrating Radar (GPR) Derived Surfaces.
- Moore, D. L., & Stewart, M. T. (1983). Geophysical signatures of fracture traces in a karst aquifer (Florida, USA). Journal of Hydrology, 61(1–3), 325–340.
- Moore, G. K., & Waltz, F. A. (1983). Objective procedures for lineament enhancement and extraction. Photogrammetric Engineering and Remote Sensing, 49(5), 641–647.
- Muchaidze, I. (2008). Imaging in karst terrain using electrical resistivity tomography.

- Naif, S., Selway, K., Murphy, B. S., Egbert, G., & Pommier, A. (2021). Electrical conductivity of the lithosphere-asthenosphere system. Physics of the Earth and Planetary Interiors, 313, 106661.
- Neumann, R. (1967). High-precision gravimetry application to cavity research. Geophysical Prospecting, 15(1), 116–134.
- Neyamadpour, A., Wan Abdullah, W. A. T., & Taib, S. (2010). Use of four-electrode arrays in three-dimensional electrical resistivity imaging survey. Studia Geophysica et Geodaetica, 54, 299–311.
- Nur, A. (1982). The origin of tensile fracture lineaments. Journal of Structural Geology, 4(1), 31–40.
- Nyquist, J. E., Peake, J. S., & Roth, M. J. S. (2007). Comparison of an optimized resistivity array with dipole-dipole soundings in karst terrain. Geophysics, 72(4), F139–F144.
- Obiadi, I. I., Onwuemesi, A. G., Anike, O. L., Obiadi, C. M., Ajaegwu, N. E., Anakwuba, E. K., Akpunonu, E. O., & Ezim, E. O. (2012). Imaging subsurface fracture characteristics using 2D electrical resistivity tomography. Int Res J Eng Sci Technol Innov, 1, 103–110.
- Ogata, K., Senger, K., Braathen, A., & Tveranger, J. (2014). Fracture corridors as seal-bypass systems in siliciclastic reservoir-cap rock successions: Field-based insights from the Jurassic Entrada Formation (SE Utah, USA). Journal of Structural Geology, 66, 162–187.
- Ohaegbuchu, H. E., Anyadiegwu, F. C., Odoh, P. O., & Orji, F. C. (2019). Review of top notch electrode arrays for geoelectrical resistivity surveys. *Journal of the Nigerian Society of Physical Sciences*, 147–155.
- Okpoli, C. C. (2013). Sensitivity and resolution capacity of electrode configurations. International Journal of Geophysics, 2013(1), 608037.

- Olayinka, A. I., & Yaramanci, U. (2000). Assessment of the reliability of 2D inversion of apparent resistivity data [Link]. *Geophysical Prospecting*, 48(2), 293–316.
- Oldenburg, D. W., & Li, Y. (1999). Estimating depth of investigation in dc resistivity and IP surveys. Geophysics, 64(2), 403–416.
- O'leary, D. W., Friedman, J. D., & Pohn, H. A. (1976). Lineament, linear, linear, linearies some proposed new standards for old terms. Geological Society of America Bulletin, 87(10), 1463–1469.
- Parker Jr, E. H., & Hawman, R. B. (2012). Multi-channel analysis of surface waves (MASW) in karst terrain, Southwest Georgia: Implications for detecting anomalous features and fracture zones. Journal of Environmental and Engineering Geophysics, 17(3), 129–150.
- Parizek, R. R. (1976). On the nature and significance of fracture traces and lineaments in carbonate and other terranes.
- Petersen, G. W., & Chesters, G. (1966). Quantitative determination of calcite and dolomite in pure carbonates and limestones. Journal of Soil Science, 17(2), 317–327.
- Piroddi, L., Calcina, S. V., Erriu, S., Trogu, A., & Ranieri, G. (2021). Integrated active and passive geophysical methods to explore underground soils in urban scenarios: the case of "Stampace alto" in Cagliari (Italy). 2021 21st International Conference on Computational Science and Its Applications (ICCSA), 234–241.
- Polk, J. S., Persoiu, A., & Pace-Graczyk, K. J. (2007). Underground Florida: A field trip guidebook of the West Central Florida karst.
- Prabu, P., & Rajagopalan, B. (2013). Mapping of lineaments for groundwater targeting and sustainable water resource management in hard rock hydrogeological environment using RS-GIS. Climate Change and Regional/Local Responses, 235–247.

- Pradipta, A., Kirmizakis, P., Papadopoulos, N., & Soupios, P. (2025). A non-invasive experiment for root zone monitoring using electrical resistivity imaging. Environmental Earth Sciences, 84(1), 1–17.
- Press, W. H., Teukolsky, S. A., Vetterling, W. T., & BP, F. (1986). 1992. Numerical Recipes in Fortran 77: the art of scientific computing. Cambridge University Press, New York.
- Robert, T., Caterina, D., Deceuster, J., Kaufmann, O., & Nguyen, F. (2012). A salt tracer test monitored with surface ERT to detect preferential flow and transport paths in fractured/karstified limestones. Geophysics, 77(2), B55–B67.
- Robinson, D. A., Binley, A., Crook, N., Day-Lewis, F. D., Ferré, T. P. A., Grauch, V. J. S., Knight, R., Knoll, M., Lakshmi, V., & Miller, R. (2008). Advancing process-based watershed hydrological research using near-surface geophysics: A vision for, and review of, electrical and magnetic geophysical methods. Hydrological Processes: An International Journal, 22(18), 3604–3635.
- Robinson, E. S. (1988). Basic exploration geophysics.
- Rodriguez, V., Gutiérrez, F., Green, A. G., Carbonel, D., Horstmeyer, H., & Schmelzbach, C. (2014). Characterizing sagging and collapsing sinkholes in a mantled karst by means of ground penetrating radar (GPR). Environmental & Engineering Geoscience, 20(2), 109–132.
- Rucker, D. F., & Glaser, D. R. (2015). Standard, random, and optimum array conversions from two-pole resistance data. Journal of Environmental and Engineering Geophysics, 20(3), 207–217.
- Rugel, K. (2020). Stakeholders reach consensus in troubled waters: Apalachicola-Chattahoochee-Flint River Basin, southeastern USA. *Case Studies in the Environment*, 4(1), 1112837.

- Sander, P. (2007). Lineaments in groundwater exploration: a review of applications and limitations. Hydrogeology Journal, 15(1), 71–74.
- Scheiber, T., Fredin, O., Viola, G., Jarna, A., Gasser, D., & Łapińska-Viola, R. (2015). Manual extraction of bedrock lineaments from high-resolution LiDAR data: methodological bias and human perception. Gff, 137(4), 362–372.
- Schmelzbach, C., Jordi, C., Sollberger, D., Doetsch, J., Kaufmann, M., Meijer, W. Y., Manukyan, E., Robertsson, J., Maurer, H., & Greenhalgh, S. (2015). Understanding the impact of karst on seismic wave propagation-a multi-method geophysical study. 77th EAGE Conference and Exhibition-Workshops, 2015(1), 1–5.
- Setzer, J. (1966). Hydrologic significance of tectonic fractures detectable on airphotos. Groundwater, 4(4), 23–27.
- Sharma, P. V. (1997). Environmental and engineering geophysics. Cambridge University Press.
- Singhal, B. B. S., & Gupta, R. P. (2010). Applied hydrogeology of fractured rocks. Springer Science & Business Media.
- Smith, M. J., & Wise, S. M. (2007). Problems of bias in mapping linear landforms from satellite imagery. International Journal of Applied Earth Observation and Geoinformation, 9(1), 65–78.
- Soge, A. O., Popoola, O. I., & Adetoyinbo, A. A. (2019). A four-point electrical resistivity method for detecting wood decay and hollows in living trees. European Journal of Wood and Wood Products, 77, 465–474.
- Solomon, S., & Ghebreab, W. (2006). Lineament characterization and their tectonic significance using Landsat TM data and field studies in the central highlands of Eritrea. Journal of African Earth Sciences, 46(4), 371–378.

- Solomon, S., & Quiel, F. (2006). Groundwater study using remote sensing and geographic information systems (GIS) in the central highlands of Eritrea. Hydrogeology Journal, 14, 1029–1041.
- Souque, C., Knipe, R. J., Davies, R. K., Jones, P., Welch, M. J., & Lorenz, J. (2019). Fracture corridors and fault reactivation: Example from the Chalk, Isle of Thanet, Kent, England. Journal of Structural Geology, 122, 11–26.
- Stewart, L. M., Warner, D., & Dawson, B. J. (1999). Hydrogeology and water quality of the Upper Floridan Aquifer, western Albany area, Georgia (Vol. 99, Issue 4140). US Department of the Interior, US Geological Survey.
- Storz, Storz, & Jacobs. (2001). Electrical resistivity tomography to investigate geological structures of the earth's upper crust. Geophysical Prospecting, 48(3), 455–471.
- Šumanovac, F., & Weisser, M. (2001). Evaluation of resistivity and seismic methods for hydrogeological mapping in karst terrains. Journal of Applied Geophysics, 47(1), 13–28.
- Swarzenski, P. W., Johnson, C. D., Lorenson, T. D., Conaway, C. H., Gibbs, A. E., Erikson, L. H., Richmond, B. M., & Waldrop, M. P. (2016). Seasonal electrical resistivity surveys of a coastal bluff, Barter Island, North Slope Alaska. Journal of Environmental and Engineering Geophysics, 21(1), 37–42.
- Szalai, S., Kovács, A., Kuslits, L., Facskó, G., Gribovszki, K., Kalmár, J., & Szarka, L. (2018). Characterisation of fractures and fracture zones in a carbonate aquifer using electrical resistivity tomography and pricking probe methods. Journal of Geoscience and Environment Protection, 6(4), 1–21.
- Telford, W. M., Geldart, L. P., & Sheriff, R. E. (1990). Applied geophysics. Cambridge University Press.

- Terech, N. (2006). Fracture patterns, lineaments and seismic reflection data: Integration for fault mapping in the Appalachian Basin of east-central New York State. State University of New York at Buffalo.
- Tiab, D., & Donaldson, E. C. (2024). Petrophysics: theory and practice of measuring reservoir rock and fluid transport properties. Elsevier.
- Tiren, S. (2010). Lineament interpretation. Short review and methodology.
- Van Riet, B., Six, S., Walraevens, K., Vandenbohede, A., & Hermans, T. (2022). Assessing the impact of fractured zones imaged by ERT on groundwater model prediction: a case study in a chalk aquifer in Voort (Belgium). Frontiers in Water, 3, 783983.
- Van Schoor, M. (2002). Detection of sinkholes using 2D electrical resistivity imaging. Journal of Applied Geophysics, 50(4), 393–399.
- Verdet, C., Sirieix, C., Marache, A., Riss, J., & Portais, J.-C. (2020). Detection of undercover karst features by geophysics (ERT) Lascaux cave hill. Geomorphology, 360, 107177.
- Wait, R. L. (1963). Geology and ground-water resources of Dougherty County, Georgia. USGPO.
- White, W. B. (1988). Geomorphology and hydrology of karst terrains.
- White, W. B. (1990). Surface and near-surface karst landforms. Groundwater Geomorphology: Geol. Soc. Am. Special Paper, 252, 157–175.
- Wise, D. U., Funiciello, R., Parotto, M., & Salvini, F. (1985). Topographic lineament swarms: clues to their origin from domain analysis of Italy. Geological Society of America Bulletin, 96(7), 952–967.
- Woodruff Jr, C. M., & Caran, S. C. (1984). Lineaments of Texas---Possible Surface Expressions of Deep-Seated Phenomena.

- Wylie, B.; Jubran, R.; Carnes, C.; Hundley, B.; Gallagher, E.; Nguyen, T.; Khalifa, M.; Schroeder,
 P.; Dowd, J.; Hawman, R. Shallow Geophysical Studies of Natural Hazards and Groundwater
 Systems in the Southeastern US: Geological Society of America Southeastern Section
 Meeting Conference, Blacksburg, Virginia, April 9-10, 2014, poster forum
- Xu, W., Bernardes, S., Bacchus, S. T., & Madden, M. (2016). Mapped fractures and sinkholes in the Coastal Plain of Florida and Georgia to infer environmental impacts from Aquifer Storage and Recovery (ASR) and supply wells in the regional Karst Floridan Aquifer System. Journal of Geography and Geology, 8(2), 76–110.
- Zarroca, M., Bach, J., Linares, R., & Pellicer, X. M. (2011). Electrical methods (VES and ERT) for identifying, mapping, and monitoring different saline domains in a coastal plain region (Alt Empordà, Northern Spain). Journal of Hydrology, 409(1–2), 407–422.
- Zhou, W., Beck, B. F., & Adams, A. L. (2002). Effective electrode array in mapping karst hazards in electrical resistivity tomography. Environmental Geology, 42, 922–928.
- Zhou, W., Beck, B. F., & Stephenson, J. B. (2000). Reliability of dipole-dipole electrical resistivity tomography for defining depth to bedrock in covered karst terranes. Environmental Geology, 39, 760–766.
- Zhu, J., Currens, J. C., & Dinger, J. S. (2011). Challenges of using electrical resistivity method to locate karst conduits—a field case in the Inner Bluegrass Region, Kentucky. Journal of Applied Geophysics, 75(3), 523–530.

APPENDIX A

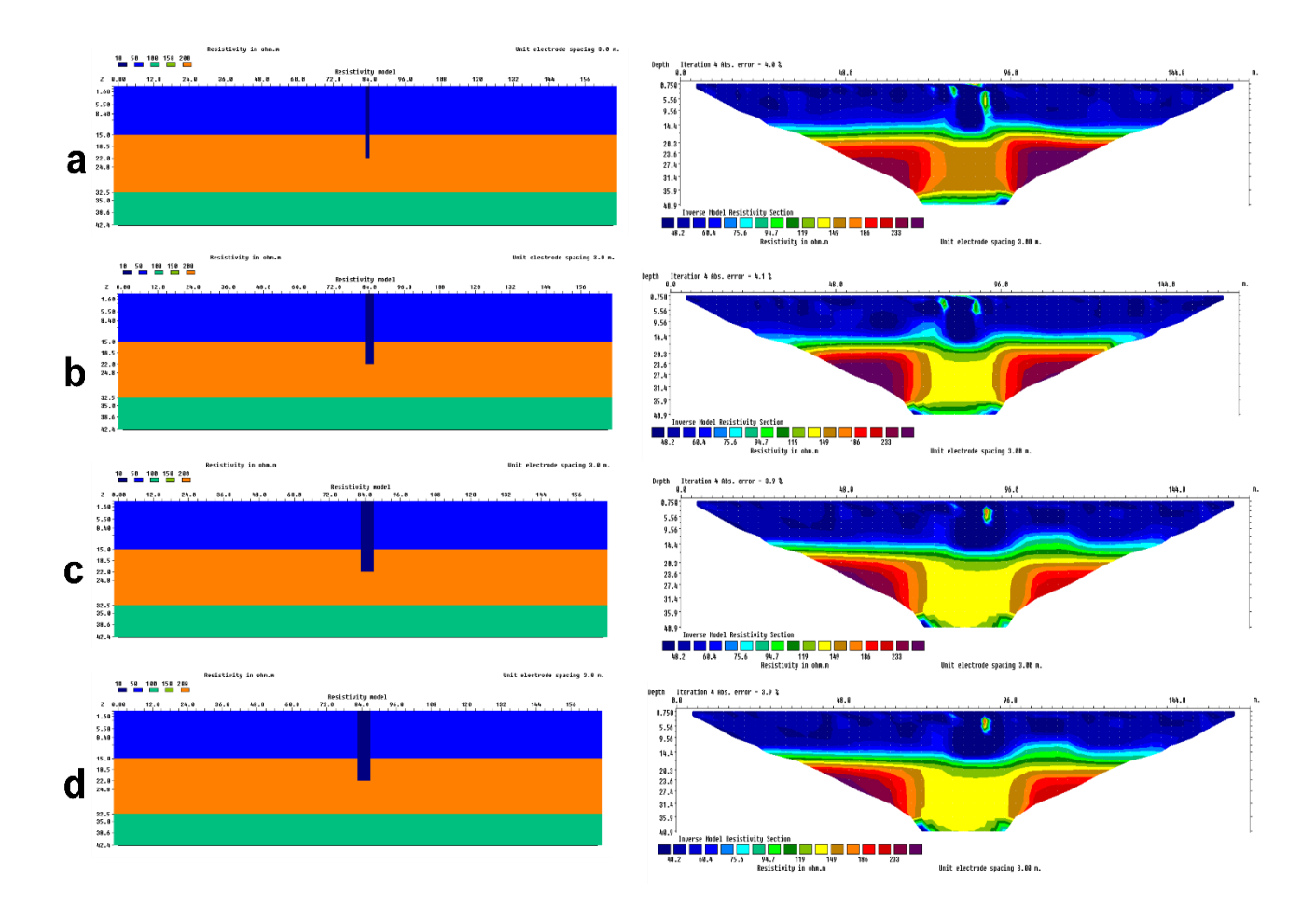
The figure below is the excel file used in generating the forward models in the Res2DMod software. A complete version of this spreadsheet is available upon request.

Name of model	Thesis																			
Number of electrodes	56																			
Number of pseudosection data levels	32																			
Flag for underwater survey	0																			
Electrode spacing	3																			
Type of grid model	2																			
Offset of first block	0																			
Total length on survey	165																			
Number of resistiivty values in model	5																			
Number of nodes per units spacing	2																			
Model resistivity values	10	50	100	150	200															
Number of rows of rectangular blocks	20																			
Depth to horizontal grid mesh line	0.8	1.6	3	5.5	8.4	10.5	15	18.5	22	24.8	32.5	35	38.6	42.4	46.8	52.4	56.6	58.4	61.8	6
	1	1	1	1	1	1	1	1	1	1	1	1	1	1	1	1	1	1	1	
	1	1	1	1	1	1	1	1	1	1	1	1	1	1	1	1	1	1	1	
	1	1	1	1	1	1	1	1	1	1	1	1	1	1	1	1	1	1	1	
	1	1	1	1	1	1	1	1	1	1	1	1	1	1	1	1	1	1	1	
	1	1	1	1	1	1	1	1	1	1	1	1	1	1	1	1	1	1	1	
	1	1	1	1	1	1	1	1	1	1	1	1	1	1	1	1	1	1	1	
	1	1	1	1	1	1	1	1	1	1	1	1	1	1	1	1	1	1	1	
	1	1	1	1	1	1	1	1	1	1	1	1	1	1	1	1	1	1	1	
	1	1	1	1	1	1	1	1	1	1	1	1	1	1	1	1	1	1	1	
	1	1	1	1	1	1	1	1	1	1	1	1	1	1	1	1	1	1	1	
	1	1	1	1	1	1	1	1	1	1	1	1	1	1	1	1	1	1	1	
	1	1	1	1	1	1	1	1	1	1	1	1	1	1	1	1	1	1	1	
	1	1	1	1	1	1	1	1	1	1	1	1	1	1	1	1	1	1	1	
	1	1	1	1	1	1	1	1	1	1	1	1	1	1	1	1	1	1	1	
	1	1	1	1	1	1	1	1	1	1	1	1	1	1	1	1	1	- 1	1	
	1	1	1	1	1	1	1	1	1	1	1	1	1	1	1	1	1	1	1	
	1	1	1	1	1	1	1	1	1	1	1	1	1	1	1	1	1	1	1	
	1	1	1	1	1	1	1	1	1	1	1	1	1	1	1	1	1	1	1	
	1	1	1	1	1	1	1	1	1	1	1	1	1	1	1	1	1	1	1	
	1	1	1	1	1	1	1	1	1	1	1	1	1	1	1	1	1	1	1	
Type of array	3																			
Flag for calcualted apparent resistivity																				
Flag for potential values	0																			

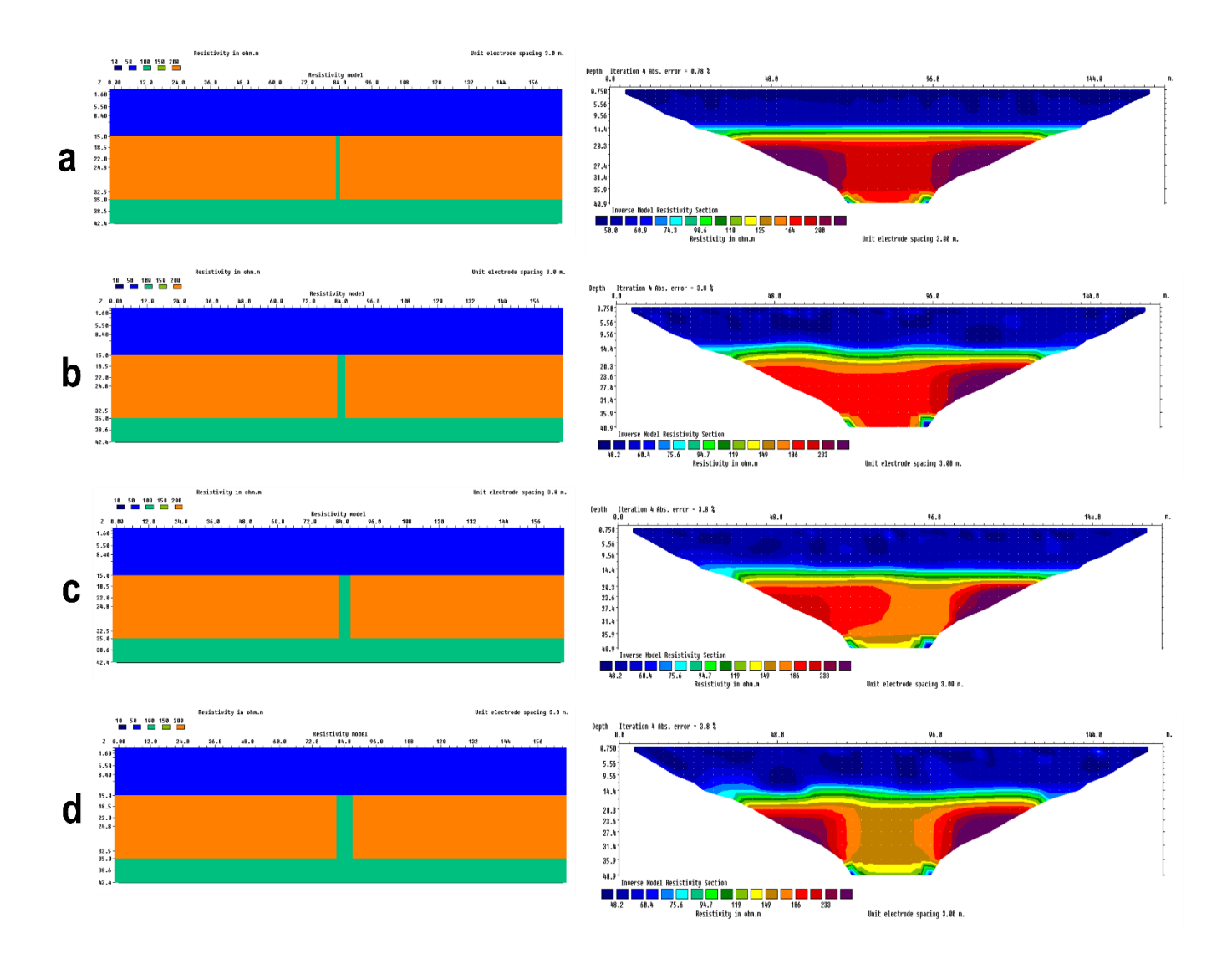
APPENDIX B

In this appendix, synthetic data for different fracture simulations using the dipole-dipole array are displayed. The files for creating these simulations are available upon request. The model sections show;

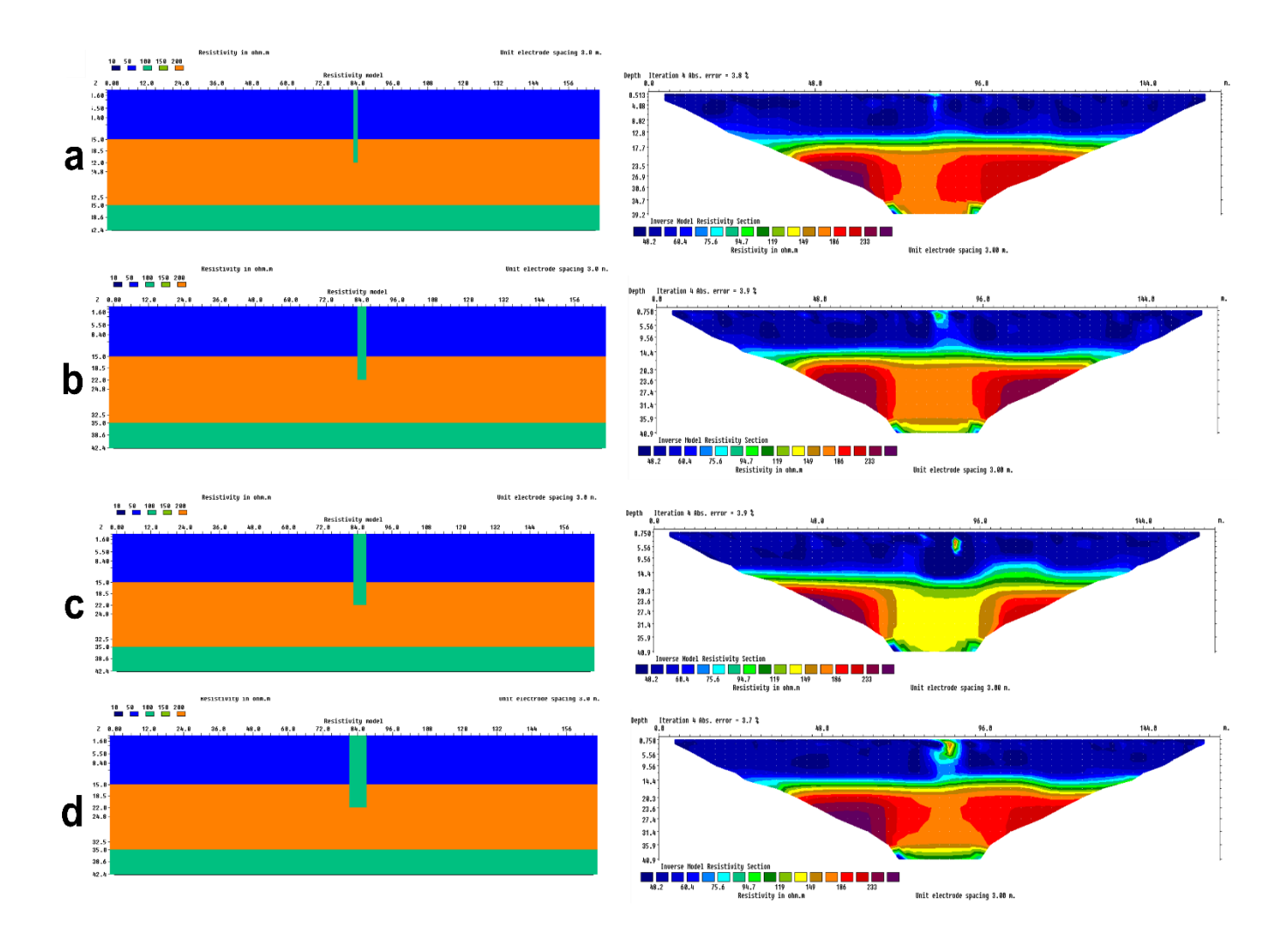
a) Fractures of different widths extending into the Ocala limestone (a, b, c and d represent 1m, 2m, 3m and 4m fracture widths respectively)



b) 100 ohm-m fractures of different widths confined in the Ocala limestone (a, b, c and d represent 1m, 2m, 3m and 4m fracture widths respectively)



c) 100 ohm-m fractures of different widths extending into the Ocala limestone (a, b, c and d represent 1m, 2m, 3m and 4m fracture widths respectively)



d) Inversion for the three distinct layers without a fracture constructed. Visual inspections of this section show that the dipole-dipole has a greater depth of penetration of about 41 m compared to the Wenner array of about 30 m. This indicates that the dipole-dipole is more suitable in delineating the deeper extent of fractures within Dougherty County compared to the Wenner array.

